UNIVERSIDADE DE LISBOA
INSTITUTO SUPERIOR TÉCNICO

Measurement of the polarizations of prompt and non-prompt J/ψ and $\psi(2\mathrm{S})$ mesons produced in pp collisions at $\sqrt{s} = 13$ TeV

Mariana Henriques de Araújo

Supervisor: Doctor Pietro Faccioli
Co-Supervisors: Doctor Carlos Manuel Lourenço
Doctor João Carlos Carvalho de Sá Seixas

Thesis approved in public session to obtain the PhD Degree in

Physics

Jury final classification: **Pass with Distinction and Honour**

2025

UNIVERSIDADE DE LISBOA
INSTITUTO SUPERIOR TÉCNICO

Measurement of the polarizations of prompt and non-prompt J/ψ and $\psi(2\mathrm{S})$ mesons produced in pp collisions at $\sqrt{s} = 13$ TeV

Mariana Henriques de Araújo

Supervisor: Doctor Pietro Faccioli
Co-Supervisors: Doctor Carlos Manuel Lourenço
Doctor João Carlos Carvalho de Sá Seixas

Thesis approved in public session to obtain the PhD Degree in

Physics

Jury final classification: **Pass with Distinction and Honour**

Jury

Chairperson: Doctor João Paulo Ferreira da Silva, Instituto Superior Técnico, Universidade de Lisboa

Members of the Committee:

Doctor António Joaquim Onofre Abreu Ribeiro Gonçalves, Escola de Ciências, Universidade do Minho

Doctor João Carlos Carvalho de Sá Seixas, Instituto Superior Técnico, Universidade de Lisboa

Doctor Michele Gallinaro, Instituto Superior Técnico, Universidade de Lisboa

Doctor Pedro Manuel Vieira de Castro Ferreira da Silva, CERN - European Organization for Nuclear Research

Funding Institution

FCT: Fundação para a Ciência e a Tecnologia

2025

Resumo

A Cromodinâmica Quântica (QCD) é o sector do Modelo Padrão responsável por descrever interações entre quarks e gluões. Devido à natureza única, dentro do Modelo Padrão, da sua constante de acoplamento, cálculos em QCD permanecem um desafio. Quarkónia, estados ligado de um quark pesado e o seu respetivo antiquark, são o caso de estudo mais simples para processos de formação de hadrões, sendo portanto as sondas ideais para uma melhor compreensão de QCD.

Nesta tese, estudamos uma das propriedades fundamentais de estados de quarkónio, a sua polarização, caraterizada experimentalmente pela distribuição angular dos seus produtos de decaimento. Usando amostras de dados recolhidas pela experiência CMS em 2017 e 2018, correspondendo a uma luminosidade integrada total de 103.3 fb^{-1}, medimos as polarizações de mesões J/ψ e $\psi(2\mathrm{S})$ *prompt* e *non-prompt* produzidos em colisões protão-protão a $\sqrt{s} = 13$ TeV, usando o canal de decaimento em dimuão. O parâmetro de anisotropia polar no referencial de helicidade, $\lambda_\vartheta^{\mathrm{HX}}$, é medido em função do momento transverso, p_{T}, dos dois estados de charmónio, no intervalo 25–120 GeV para J/ψ e no intervalo 20–100 GeV para $\psi(2\mathrm{S})$. As medições são comparadas com previsões.

As polarizações *non-prompt* estão de acordo com previsões baseadas na hipótese de que, acima de um p_{T} em volta de 25 GeV, estes estados são predominantemente produzidos em decaimentos de dois corpos de mesões B. Os resultados *prompt* excluem definitivamente a expectativa da teoria de polarizações transversas fortes (λ_ϑ =+1) para o intervalo de p_{T} em estudo, que excede 30 vezes a massa de J/ψ, dado the λ_ϑ tende para um valor assintótico de 0.3 neste intervalo. Tomado em conjunto com medições prévias do LHC para $\sqrt{s} = 7$ TeV, compatíveis na região de p_{T} de sobreposição, λ_ϑ *prompt* mostra uma variação significativa com p_{T}, a baixo p_{T}.

Palavras-chave: CMS, física, física de partículas, produção de quarkónio, polarização de quarkónio

Abstract

Quantum Chromodynamics (QCD) is the sector of the Standard Model responsible for describing interactions between quarks and gluons. Because of the unique nature, within the Standard Model, of its coupling constant, calculations in QCD remain a challenge. Quarkonia, bound states of a heavy quark and its respective antiquark, are the simplest case study for hadron formation processes, and so are the ideal probes for a better understanding of QCD.

In this thesis, we study one of the fundamental properties of quarkonium states, their polarization, characterized experimentally by the angular distribution of their decay products. Using data samples collected by the CMS experiment in 2017 and 2018, corresponding to a total integrated luminosity of 103.3 fb^{-1}, we measure the polarizations of prompt and non-prompt J/ψ and $\psi(2\mathrm{S})$ mesons produced in proton-proton collisions at $\sqrt{s} = 13$ TeV, using the dimuon decay channel. The polar anisotropy parameter in the helicity frame, $\lambda_\vartheta^{\mathrm{HX}}$, is measured as a function of the transverse momentum, p_T, of the two charmonium states, in the 25–120 GeV range for the J/ψ and in the 20–100 GeV range for the $\psi(2\mathrm{S})$. The measurements are compared with predictions.

The non-prompt polarizations agree with predictions based on the hypothesis that, above a p_T of around 25 GeV, these states are predominantly produced in two-body B meson decays. The prompt results definitively exclude the theory expectation of strong transverse polarizations (λ_ϑ =+1) for the p_T range under study, which exceeds 30 times the J/ψ mass, as λ_ϑ tends to an asymptotic value around 0.3 over this range. Taken together with previous LHC measurements for $\sqrt{s} = 7$ TeV, compatible in the overlap p_T region, the prompt λ_ϑ shows a significant variation with p_T, at low p_T.

Keywords: CMS, physics, particle physics, quarkonium production, quarkonium polarization

Acknowledgments

This thesis was the product of years of hard work. It was written by me, but its creation depended on the contributions of a very large group of people, either their work, their support, or just their company.

First, I must extend a thanks to the Foundation for Science and Technology (FCT) which provided the funding for my PhD studies. I also want to thank the Laboratory of Instrumentation and Experimental Particle Physics (LIP) for hosting me for the duration of the work, as well as Instituto Superior Técnico (IST) for providing my doctoral degree.

Moving to less impersonal dedications, I would like to thank all the members of the LIP teams in which I was included, LIP-CMS and LIP-Pheno, for their advice and contributions to the ongoing work. I also extend thanks to other CMS collaborators that contributed to my work, namely Alberto Sanchez Hernandez, who provided the simulated samples used in the analysis, as well as a wealth of information on the experimental details of the detector and the triggers.

I particularly thank my colleagues at LIP, the MSc and PhD students with whom I shared a work space, lunch and coffee breaks, the occasional complaint, and true companionship. The life of a student getting started in academia isn't always easy, but it becomes a little easier when we don't do it alone.

My team of thesis supervisors were all essential to my work, complementing and matching each other's contributions. João Seixas, Carlos Lourenço, and my supervisor, Pietro Faccioli, were always present to help me solve problems, to work out our next steps, to adapt and improvise to the circumstances, and to push me to keep going. They helped me with every detail of the thesis: the understanding of the theory, the details of the coding, the presentations, the paperwork, and anything else that came up.

In addition to their help, I also benefited greatly from the contributions of past students in the CMS quarkonium polarization studies group: Ilse Krätschmer, Valentin Knünz and Thomas Madlener were always ready and willing to contribute whatever was necessary, taking time from their busy schedules and lives to extend a helping hand.

At the risk of seeming partial, I must thank Carlos Lourenço again, this time for choosing me, among all the applicants, to be his student for the CERN Summer Student Programme in 2016. His choice led to an unforgettable summer and to my very first introduction to quarkonium. It was in this programme that I met my supervisory team and that I began my first steps in the field of quarkonium polarization. It wouldn't be an exaggeration to say that it changed my life.

Finally, I want to thank all my friends, and particularly my family. To my mother, Fátima, and my father, Pedro, thank you for always supporting me in whatever choices I make, and for believing in me. I can't claim to be the first doctor in the family, but I'll still be glad to open that bottle of Barca Velha to celebrate it. To my brother, Manuel, who beat me to the honour, thank you for encouraging me to be my most curious self, and for having so many questions for me that I am reminded why I like to find answers so much. To my grandmother, Lucília, thank you for being proud of me.

To my family, not by blood but by choice, to Catarina and Luís, Miúcha and Vítor, to a whole brood of inherited aunts and cousins, thank you for taking me in, for being my friends, for being there for me in whatever I need. Thank you as well to all my furry friends, but particularly to my special girls Zelda and Tsuki and to my special boy Hong.

Finally, a special thank you to Madalena: friend, family and everything in between. I genuinely couldn't have done it without you. Thank you for putting up with me, at my best and at my worst.

The work of this thesis was supported by Fundação para a Ciência e a Tecnologia (FCT), Portugal, through the FCT PhD grant SFRH/BD/140671/2018.

Contents

List of Tables

List of Figures

List of Abbreviations

ALICE	A Large Ion Collider Experiment
ATLAS	A Toroidal LHC Apparatus
BPH	B Physics
BPix	Barrel Pixel Detector
BS	Beam Spot
CB	Crystal Ball
CDF	Collider Detector at Fermilab
CEM	Colour-Evaporation Model
CERN	Organisation Européenne pour la Recherche Nucléaire
CMS	Compact Muon Solenoid
CM	Centre of Mass
CSC	Cathode Strip Chamber
CSM	Colour-Singlet Model
CS	Collins–Soper
DT	Drift Tube
ECAL	Electromagnetic Calorimeter
FPix	Forward Pixel Detector
HCAL	Hadronic Calorimeter
HLT	High Level Trigger
HX	Helicity
IP	Interaction Point
L1	Level 1

LDME	Long-Distance Matrix Element
LEP	Large Electron-Positron Collider
LHCb	Large Hadron Collider beauty
LHC	Large Hadron Collider
LO	Leading Order
LSB	Left Sideband
LS	Long Shutdown
MB	Muon Barrel
MC	Monte Carlo
ME	Muon Endcap
NLO	Next-to-Leading Order
NNLO	Next-to-Next-to-Leading Order
NPLSB	Non-Prompt Left Sideband
NPRSB	Non-Prompt Right Sideband
NPS	Non-Prompt Signal Region
NP	Non-Prompt
NRQCD	Non-Relativistic Quantum Chromodynamics
PAG	Physics Analysis Group
PD	Primary Data Set
PRLSB	Prompt Left Sideband
PRRSB	Prompt Right Sideband
PRS	Prompt Signal Region
PR	Prompt
PU	Pile-Up
PV	Primary Vertex
QCD	Quantum Chromodynamics
RPC	Resistive Plate Chamber
RSB	Right Sideband

SDC Short-Distance Coefficient

SM Standard Model

SV Secondary Vertex

TEC Tracker EndCap

TIB Tracker Inner Barrel

TID Tracker Inner Disk

TOB Tracker Outer Barrel

Chapter 1

Introduction

The Standard Model of Particle Physics (SM) was first formulated in the 1960s and provides a remarkably good description of particle physics. It is a quantum field theory based on an SU(3)$\times$SU(2)$\times$U(1) gauge symmetry, relating elementary matter particles (quarks and leptons) with three fundamental forces (the strong, the weak and the electromagnetic forces) [1, 2, 3, 4]. The SM was defined in its modern form with a final addition in the form of the Higgs mechanism, introducing a new field, the Higgs field, that gives mass to all elementary particles through spontaneous symmetry breaking [5, 6, 7]. Decades of experimental observations support this theory, culminating with the discovery of the Higgs boson, in 2012, considered up to that point the last "missing piece" of the SM [8, 9]. Despite some shortcomings of the theory, irrelevant for the topics addressed in this thesis, the SM is considered an incredible success in the description of the interactions of elementary particles.

Quantum Chromodynamics (QCD) [10] is ruled by the SU(3) symmetry of the SM and describes the strong interaction between quarks and gluons, its mediating bosons. Colour, the charge associated with the strong force, is only present in these two types of particles, and this force binds the quarks into nucleons, and the nucleons into atomic nuclei, forming the basis of most visible matter. Calculations in QCD can only be performed in specific conditions, as the "running" strong coupling constant α_s [11, 12] limits the possibility to perform perturbative calculations as an expansion in orders of the coupling constant, an approach that allows the majority of calculations in the electroweak sector. In QCD, perturbative calculations are only possible for "hard scattering" processes, involving high momentum transfers at short distances for which α_s is small. In the opposite conditions, the realm of "soft QCD", the expansion in powers of α_s breaks down and the perturbative approach is no longer viable.

Processes leading to the formation of QCD bound states are characterized by low momentum transfers [13, 14], so that they are difficult to access with perturbative QCD calculations. This issue can be mitigated in cases where only heavy quarks are involved, particularly charm and beauty quarks, as is the case for quarkonia: QCD bound states of a heavy quark and its respective antiquark. In this case, the heavy masses of the b and c quarks are conjectured to lead to a separation of the quarkonium production into two separate steps, occurring at two distinct time scales. The first step, the creation of a quark-antiquark pair $Q\overline{Q}$, is governed by short-distance parton-level strong interaction processes, calculable within perturbative QCD. It is followed by the subsequent hadronization: the formation of the bound quarkonium state from the $Q\overline{Q}$ pair, under long-distance strong interactions that are ruled by non-perturbative QCD.

Despite the remaining presence of non-perturbative processes in quarkonium production, this factorization hypothesis allows for the calculation of measurable observables, and is the basis for the non-relativistic QCD (NRQCD) factorization approach [15]. NRQCD is an effective field theory, under which the initial perturbative step consists of the production of a $Q\overline{Q}$ pair, or "pre-resonance", which can have several different values of spin, angular momentum and colour (singlet or octet) eigenstates. In a second step, this $Q\overline{Q}$ state undergoes a transition to the final hadron (such as, for example, a J/ψ meson). The probability that the $Q\overline{Q}$ pre-resonance is in a certain quantum state is given by the Long-Distance Matrix Elements (LDMEs), which are considered to be constants, independent of kinematics. LDMEs cannot be calculated perturbatively, and direct calculations using, for example, lattice QCD, remain out of reach. Thus, in the current approach of NRQCD, they are determined from fits to experimental data: several experimentally accessible physics observables are sensitive to the value of the LDMEs, so that their theoretical calculations, compared with data, can be used to determine the value of these constants.

The most important of these observables are the quarkonium production cross sections and the quarkonium polarizations. Cross section measurements at the Tevatron experiments [16, 17, 18, 19] and their incompatibility with models considering only colour-singlet contributions to quarkonium production lent support to the NRQCD approach, which included colour-octet terms [20]. However, the polarization measurements performed at these experiments [21, 22, 23] showed results that were in stark contrast with NRQCD predictions [24] and, more concerningly, mutually inconsistent. This came to be known as the "quarkonium polarization puzzle". An updated methodology for polarization measurements, avoiding ambiguity in the measurements, has since been developed [25, 26, 27, 28, 29, 30].

The Large Hadron Collider (LHC) physics program has allowed for several quarkonium cross section and polarization measurements, taking advantage of its high statistics and collision energy $\sqrt{s}$. Polarization measurements in particular, using the updated, robust methodology, show no more signs of inconsistencies or mutual incompatibility, though they continue to be at odds with NRQCD predictions. A series of phenomenological studies have been done, using the available measurements [31, 32, 33, 34], finding that it is indeed possible to reconcile the measured polarization values with the NRQCD framework, although the experimental results for quarkonium production draw a picture of striking simplicity and apparent universality, contrasting with the complexity and necessary precise cancellations of NRQCD terms to reproduce it. These and other studies present the polarization dimension as uniquely positioned to test the validity of NRQCD or precisely constrain its parameters.

Currently available quarkonium polarization measurements are mainly of S-wave states, showing weak polarization with no apparent p_{T} dependence [35, 36, 37, 38, 39]. However, the large uncertainties associated with such a complex measurement, requiring the evaluation of unbiased angular distributions, make it impossible to determine conclusively whether the polarization is zero or merely small, and whether it is truly p_{T}-independent. Because of these uncertainties, the potential of polarization measurements to challenge the theory or provide unique constraints is severely limited. It is necessary to obtain new polarization measurements, using the much higher statistics of the subsequent data-taking periods of the LHC experiments, which can both extend the p_{T} range of the measurements and reduce their uncertainties so that any p_{T} dependence and deviation from zero can be probed.

This thesis aims to provide such a measurement, particularly of the charmonium S-wave states J/ψ and $\psi(2\mathrm{S})$, produced both promptly and non-promptly. The polarization measurement is performed for data collected by the Compact Muon Solenoid (CMS) in 2017 and 2018, in pp collisions at $\sqrt{s} = 13$ TeV. This is a much larger sample than the one collected in 2011, at 7 TeV, which was used for the previous CMS measurement of the prompt J/ψ and $\psi(2\mathrm{S})$ polarizations [37], and achieves unparalleled precision in a measurement of this type. The measurement reported in this thesis has been published in Ref. [40].

A brief description of quarkonium properties and production is provided in Chapter 2. Quarkonium polarization is approached in particular detail, presenting the physical quantities relevant to its measurement. The main recent experimental results of quarkonium production and polarization are presented, as well as the status of NRQCD calculations and selected phenomenological studies devoted to these topics.

Chapter 3 is dedicated to the experimental setup, with descriptions of the LHC accelerator and of the CMS detector, focusing on the components that are most relevant for the study of quarkonium production and polarization.

In Chapter 4, the event selection criteria are presented. The measured and simulated event samples are characterized, before and after applying the selection criteria, and the final event yields and variable distributions are shown, including extensive comparisons between the measured and simulated distributions, for the validation of the Monte-Carlo simulation.

The quarkonium polarization measurement procedure, as well as the corresponding results, are given in Chapter 5. Here are described the steps required to correct for detection acceptance using the simulated events, subtract the background contamination in the measured samples, and obtain the final polarization parameters from the corrected angular distributions.

Chapter 6 is devoted to the description and evaluation of possible sources of systematic uncertainties, some of them seen to be negligible and others contributing to the final result.

Chapter 7 reports the final results, including all relevant uncertainties, and shows comparisons with past measurements and theory predictions.

In this thesis, natural units are used, with $\hbar = c = 1$. Thus, energy, mass and momentum are all given in units of eV, or rather the multiples MeV, GeV and TeV.

Chapter 2

Quarkonium physics

Quarkonia are bound states of a heavy quark and its antiquark, bound by the strong force. These mesons can be formed for two flavors of heavy quark, giving rise to the charmonium (charm and anticharm pair) and bottomonium (bottom and antibottom pair) families. Such a bound state cannot be formed in the case of the top quark and its antiquark, as the high mass of these particles means that they decay through the electroweak interaction before a bound state can form.

The first charmonium meson was discovered in 1974 [41, 42]. The discovery was made independently by two research groups, one at the Stanford Linear Accelerator Center and one at the Brookhaven National Laboratory, the former naming the particle J and the latter ψ. Ultimately, the particle became known as J/ψ. The first bottomonium meson, Υ, was discovered soon after, in 1977 [43]. Due to their unique position as probes for Quantum Chromodynamics (QCD) and hadron formation, they have been the focus of continuous study since then, with the discovery of an extensive spectrum of states and the measurement of their respective properties.

2.1 Quarkonium spectrum

The members of each of the two quarkonium families occur in many different quantum states, characterized by the quantum numbers describing the angular momentum L, the spin S, the total angular momentum $J = S + L$ and the principal quantum number N. The resulting configurations are described with the notation J^{PC}, with parity $P = (-1)^{L+1}$ and charge conjugation $C = (-1)^{L+S}$, or using the spectroscopic notation $N^{2S+1}L_J$ [44].

Figures 2.1 and 2.2 illustrate the structure of the charmonium and bottomonium systems, respectively, showing a subset of the quarkonium states relevant for this thesis and of the decays that occur within each family. Decays between families, of the form $b\bar{b} \to c\bar{c}$, are negligible [44]. The figures are restricted to CP-even states, J^{++} and J^{--}, with masses below the open charm and open bottom thresholds. The CP-odd 0^{-+} (η_c and η_b) and 1^{+-} (h_c and h_b) states are not discussed in this thesis, and thus not included.

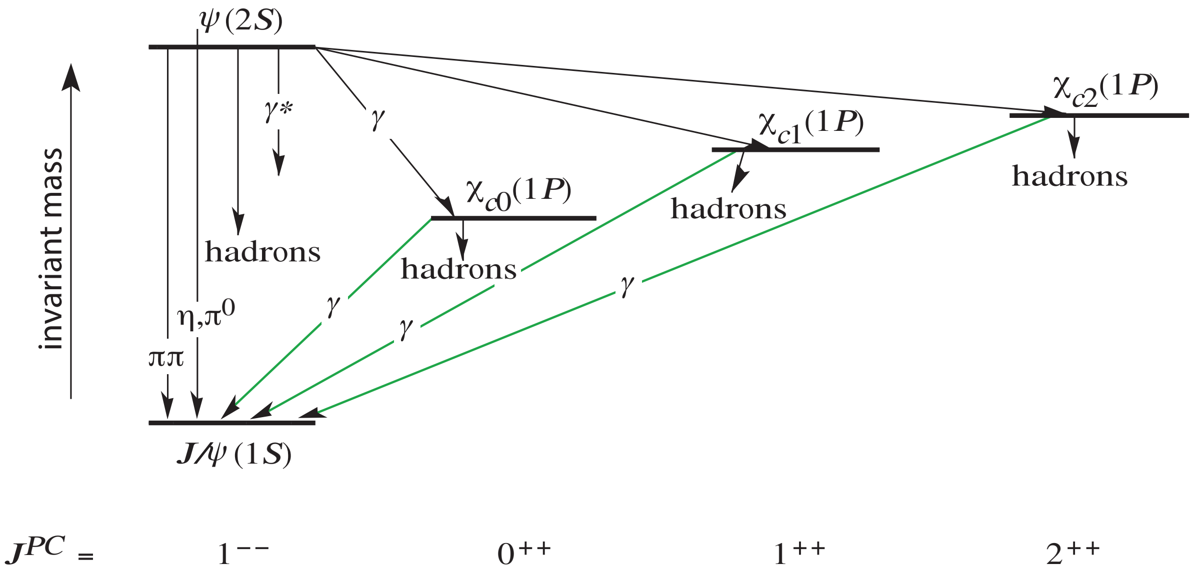

Figure 2.1: Charmonium spectrum of CP-even states below the open charm threshold and decays, adapted from Ref. [44].

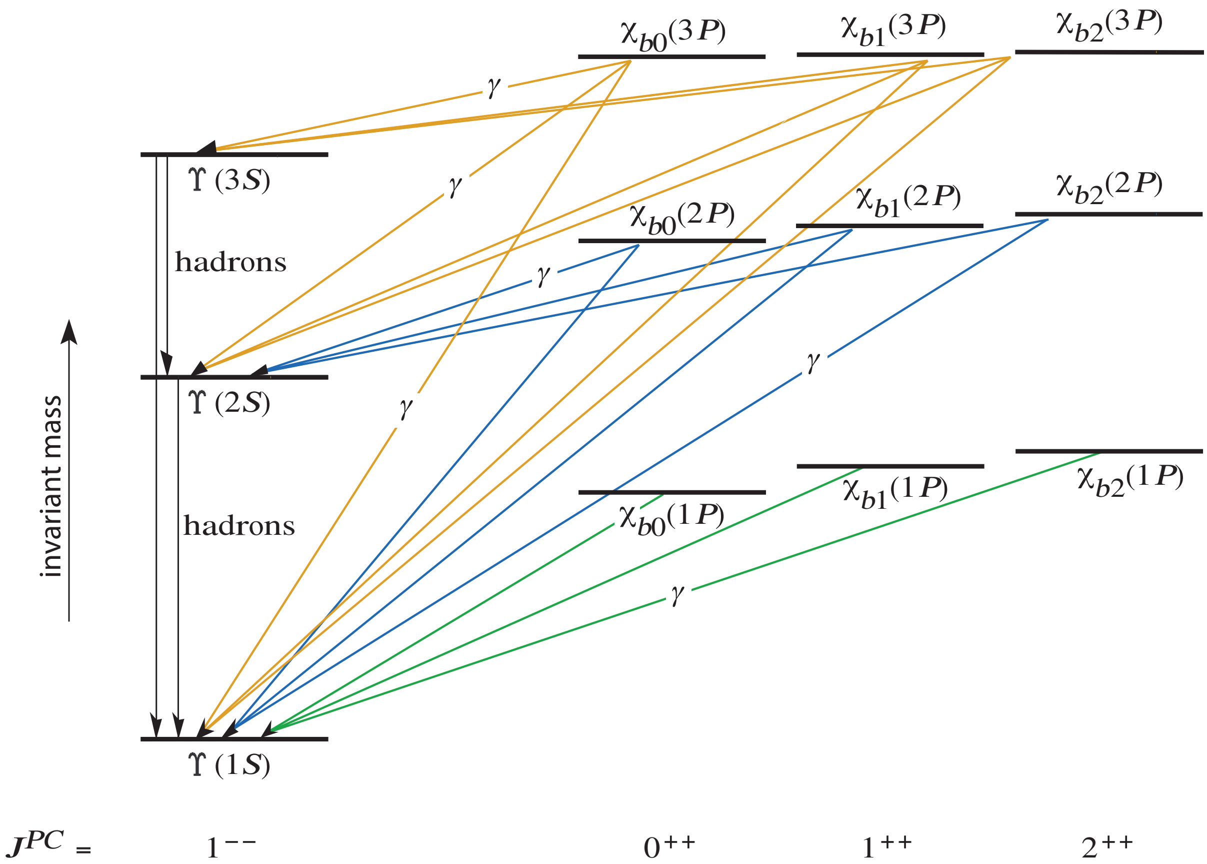

Figure 2.2: Bottomonium spectrum of CP-even states below the open bottom threshold, and a subset of decays, adapted from Ref. [44]. Decays of the type $\Upsilon(nS) \to \chi_{bJ}(mP) + \gamma$ are omitted for clarity.

The spectra can be divided into two main categories, known as the "S-wave" states ($L = 0$) and the "P-wave" states ($L = 1$). In the subset of states considered, the S-wave states are the $J^{PC} = 1^{--}$ vector mesons, which for the charmonium consists of J/ψ and its radial excitation $\psi(2\mathrm{S})$. These two states are referred to collectively as $\psi(nS)$ states ($n = 1$ or 2). For the bottomonium, the S-wave states are the $\Upsilon(1S)$ and its radial excitations $\Upsilon(2S)$ and $\Upsilon(3S)$, collectively known as $\Upsilon(nS)$. The P-wave states are the $J^{PC} = J^{++}$ pseudo vector mesons $\chi_{cJ}(1P)$ (often χ_{cJ}, for simplicity) and $\chi_{bJ}(1P)$, which occur in triplets corresponding to $J = 0, 1, 2$. For the bottomonium, there are also the radial excitations $\chi_{bJ}(2P)$ and $\chi_{bJ}(3P)$.

Experimentally, the most important decay modes for the S-wave states are the dimuon decays $\psi(nS) \to \mu\mu$ and $\Upsilon(nS) \to \mu\mu$. For the P-wave states, the radiative decays, $\chi_{cJ} \to \mathrm{J}/\psi + \gamma$ and $\chi_{bJ}(nP) \to \Upsilon(mS) + \gamma$ ($n \geq m$), are the most used. Existing measurements of particle masses, full widths, decay modes and corresponding branching fractions are listed in detail in Ref. [44].

Charmonium masses range from 3097 MeV, for the J/ψ, to 3686 MeV, for the $\psi(2\mathrm{S})$, and bottomonium masses from 9460 MeV, for the $\Upsilon(1S)$, to 10524 MeV, for the $\chi_{b2}(3P)$. As to the full widths, for the S-wave states they are small compared to the experimental measurement resolutions. For the χ_{cJ} states, this is not the case, with widths of 10.8, 0.84 and 1.97 MeV for $J = 0, 1, 2$, respectively, while the widths of the $\chi_{bJ}(nP)$ states are yet to be measured.

The decay times of the S-wave states are of the order of 10^{-21}–10^{-20} s. In the case of the P-wave states, for which we only have measurements for the charmonium, the decay times are of the order of 10^{-23}–10^{-22} s. This means that the quarkonium states only travel average distances of the order of femto- or pico-meters before they decay, and thus all quarkonium decays are classified as quasi-instantaneous or "prompt" (PR) decays.

Quarkonium states measured experimentally are a mixture of directly produced quarkonia and products of the decays of heavier states, as illustrated in Figs. 2.1 and 2.2, which are called "feed-down decays". Due to the short decay times of quarkonia, it is not possible to experimentally separate the two contributions. In principle, this would be possible by reconstructing all decay products of the heavier states, but such an approach is not typically feasible in the experimental conditions of hadronic collisions.

The experimental measurements of S- and P-wave states are therefore limited to the measurement of properties of the prompt components, including both direct and feed-down contributions. However, with measurements of the properties of the contributing feed-down states and with knowledge of the "feed-down fractions", which define the relative contribution of each production channel of the prompt samples, it is possible, *a posteriori*, to disentangle the properties of the directly produced quarkonium states and obtain constraints or predictions for unmeasured properties. The highest mass states of each family, $\psi(2\mathrm{S})$ for the charmonium and $\chi_{bJ}(3P)$ for the bottomonium, are considered to be free of feed-down decays, so that their respective prompt samples are composed entirely of directly produced quarkonium states. The corresponding measurements are thus especially important, providing essential information for the study of the feed-down chain of each family and allowing for a direct comparison with model calculations.

In the case of the charmonium family of states, in addition to the prompt component there will be a "non-prompt" (NP) contribution, consisting of feed-down decays of b-hadrons, which must be taken into account. These hadrons have average decay times of the order of 10^{-12} s [44], allowing them to travel distances of a few 100 μm between production and decay. Experimentally, non-prompt charmonia can be distinguished from prompt using this displacement, as will be detailed in Chapter 3.

2.2 Quarkonium production

Heavy quarkonium states are the ideal probes to study QCD and hadron formation due to their simplicity and symmetry as a bound state of a quark and its antiquark, as well as the heavy masses of their component quarks m_Q that cause them to fall under the study of both perturbative and non-perturbative QCD [13].

The basic concept that drives all theoretical studies to understand quarkonium production is the assumption that the production of any quarkonium state can be factorized in two parts: the production of an initial $Q\overline{Q}$ pair and its subsequent hadronization, forming the final bound state. The first part meets the conditions for perturbative calculations, involving momentum transfers of the order of m_Q, and can thus be studied theoretically. This is not the case for the second part, which falls in the non-perturbative realm of QCD.

In quarkonium production, the states can be treated as approximately non-relativistic systems. This is due to the large masses of the charm and bottom quarks, and the resulting relative quark velocity v in the bound state: $v^2 \approx 0.3$ for the charmonium and $v^2 \approx 0.1$ for the bottomonium. Due to the relatively small values of v, the scales for the two factorized steps of quarkonium production are distinct: the production of the $Q\overline{Q}$ pair is associated with a scale of m_Q, while the formation of the bound state involves the smaller dynamical scales $m_Q v$, the momentum of the pair, and $m_Q v^2$, its binding energy. The time scale of each step is proportional to the inverse of these values, so that they will be well separated if $1/\left(m_Q v^2\right) \gg 1/\left(m_Q v\right) \gg 1/m_Q$ [15]. The intuitive expectation is that, in these conditions, which are well fulfilled for bottomonium states and reasonably well for charmonium, the short-distance and long-distance effects can indeed be separated. This is not the case for all hadrons, where the time scales could have a negligible separation. Therefore, quarkonium production stands out, providing a unique opportunity to study hadron formation and dynamics involving the long-distance strong force.

Full QCD calculations of quarkonium production observables can only be performed for the perturbative part of the production, in increasing powers in α_s according to computational capabilities. For the non-perturbative step, the formation of the quarkonium bound state, perturbative approaches are invalid. Numerical lattice calculations could in principle be performed, but this extremely complex and computation-intensive approach is not, currently, the main avenue of study.

Given these limitations, calculations for quarkonium production have to rely on certain assumptions and approximations, and this is where most models discussed nowadays differ. Of the models available, the Non-Relativistic QCD (NRQCD) factorization approach is widely considered the most sound theoretically and most successful in reconciling data and model calculations. Other theoretical models under discussion are, for example, the Colour-Singlet Model (CSM) [45, 46], which can be considered a special case of the NRQCD approach, and the Colour-Evaporation Model (CEM) [47, 48]. In the following, the NRQCD factorization approach will be the focus of discussion, while other models, including some not mentioned here, can be studied in reviews such as Refs. [13, 49] and references therein.

2.2.1 Non-Relativistic QCD Factorization

NRQCD is an effective field theory first introduced in 1995 [15]. It relies on the assumption that quarkonium production can be factorized into two steps: the production of the initial $Q\overline{Q}$ pair and the formation of the bound state. In the framework of NRQCD, the production cross section of a quarkonium state thus becomes a linear combination of the form

$$\sigma(\mathcal{Q}) = \sum_n \mathcal{S}\left[Q\overline{Q}(n)\right] \cdot \mathcal{O}^{\mathcal{Q}}(n). \tag{2.1}$$

This formula is composed of two elements: the short-distance coefficients (SDCs) $\mathcal{S}\left[Q\overline{Q}(n)\right]$, describing the perturbative production of the $Q\overline{Q}$ pre-resonance in a quantum state $n = {}^{2S+1}L_J^{[\mathcal{C}]}$, where $\mathcal{C}$ is the colour multiplicity; and the long-distance matrix elements (LDMEs) $\mathcal{O}^{\mathcal{Q}}(n)$, describing the non-perturbative evolution of the $Q\overline{Q}$ in state n into the bound quarkonium $\mathcal{Q}$ in its characteristic state. Each term in this sum, referred to as a "partial cross section", gives the contribution of a particular $Q\overline{Q}$ state n to the production of the final quarkonium state, with the sum of these terms running over all possible intermediate configurations of n, including colour-singlet ($\mathcal{C} = 1$) and colour-octet ($\mathcal{C} = 8$) configurations. In this formalism, it is thus possible to have intermediate unphysical colour-octet $Q\overline{Q}$ states, which transition to a final physical colour-neutral quarkonium bound state via the non-perturbative emission or absorption of soft gluons. This process is illustrated in Fig. 2.3.

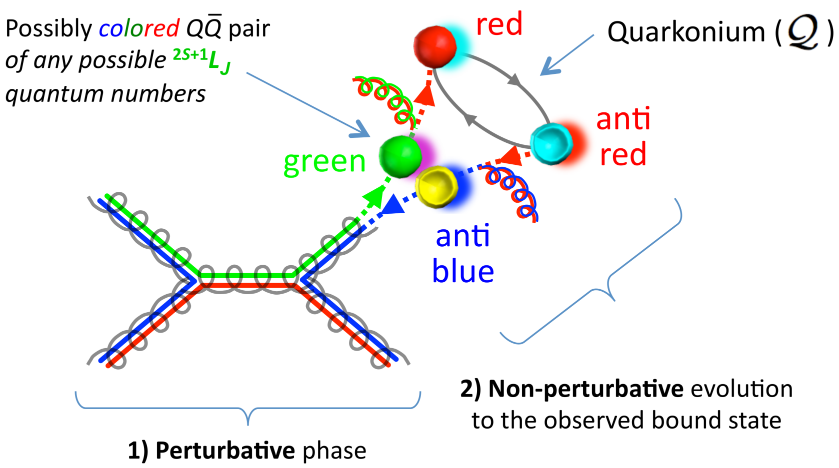

Figure 2.3: Illustration of quarkonium production according to the NRQCD factorization hypothesis: the perturbative production of an initial $Q\overline{Q}$ pair, possibly coloured, and the subsequent evolution into a colour-neutral bound quarkonium state via the non-perturbative emission of soft gluons [50].

Despite this approach being widely used, there is not yet a complete proof of factorization. A discussion of the difficulties in establishing NRQCD factorization can be found in Ref. [13], with the issue hinging on establishing that the LDMEs are universal. A first step was achieved in 2005, when it was shown that this was the case through two-loop order [51, 52].

The SDCs and LDMEs

The SDCs can be calculated perturbatively, as an expansion in powers of α_s. They represent the sum of the partonic cross sections that contribute to produce a $Q\overline{Q}$ pair in the state n, convoluted with the parton distribution functions. The SDCs account for the full kinematic dependence of the process, and are the only process-dependent contribution to the cross section $\sigma(\mathcal{Q})$. Each individual SDC must not necessarily take physical values or be observable on its own. In fact, both the SDCs and LDMEs are unphysical constructs and take on meaning only as contributions to a final physical quantity. Additionally, only the product of SDC and LDME is relevant in comparisons with experimental measurements: if one changes the computation of a given SDC, in perturbative QCD, one needs to change the corresponding LDME.

The LDMEs behave as the relative weights of the SDCs in Eq. 2.1: they can be interpreted as the probability of each intermediate $Q\overline{Q}$ in state n to form a given quarkonium state $\mathcal{Q}$. They are constants, kinematics- and process-independent, and vary only according to the initial state n of the pre-resonance and the final quarkonium state $\mathcal{Q}$. The LDMEs are not calculable with currently available techniques, and are instead estimated by fits to experimental data, as will be explored in more detail in Section 2.4.

Velocity scaling rules

In principle, one would have to sum over all configurations of n, an infinity of terms, in order to obtain the final value of $\sigma(\mathcal{Q})$. However, the LDMEs follow certain hierarchies, or "velocity scaling rules", which estimate the relative size of each LDME in powers of the heavy-quark velocity v, so that the NRQCD factorization formula is in fact a double expansion in powers of v and powers of α_s. Several slightly differing velocity scaling rules exist in the literature. Table 2.1 summarizes the most important states n for the S-wave 1^{--} and P-wave J^{++} states, showing their expected suppression in powers of v, according to a common definition [53].

S-wave (1^{--})	${}^1S_0^{[\mathcal{C}]}$	${}^3S_1^{[\mathcal{C}]}$	${}^1P_1^{[\mathcal{C}]}$	${}^3P_J^{[\mathcal{C}]}$	${}^3D_J^{[\mathcal{C}]}$	${}^1D_2^{[\mathcal{C}]}$
Colour-singlet ($\mathcal{C}=1$)	v^8	**1**	v^8	v^8	v^8	v^{12}
Colour-octet ($\mathcal{C}=8$)	$\boldsymbol{v^4}$	$\boldsymbol{v^4}$	v^8	$\boldsymbol{v^4}$	v^8	v^{12}
P-wave (J^{++})	${}^1S_0^{[\mathcal{C}]}$	${}^3S_1^{[\mathcal{C}]}$	${}^1P_1^{[\mathcal{C}]}$	${}^3P_J^{[\mathcal{C}]}$	${}^3D_J^{[\mathcal{C}]}$	${}^1D_2^{[\mathcal{C}]}$
Colour-singlet ($\mathcal{C}=1$)	v^6	v^6	v^{10}	$\boldsymbol{v^2}$	v^{10}	v^{10}
Colour-octet ($\mathcal{C}=8$)	v^6	$\boldsymbol{v^2}$	v^6	v^6	v^6	v^{10}

Table 2.1: Expected scaling of the LDMEs of each pre-resonance state n, in powers of v, for S- and P-wave final quarkonium states [53]. The LDMEs considered for calculations are outlined in bold.

In the observed non-relativistic regime of large m_Q and small v, higher powers of v will be increasingly suppressed, and the sum can be truncated at a fixed order in v, resulting in only a small number of dominating terms contributing to the linear combination for each $\mathcal{Q}$ state. There is a possibility that

LDMEs that are suppressed by higher powers in v could still lead to significant contributions to the final state when their corresponding SDCs take large values. The standard approach, taking all factors into account, is to include in the sum of Eq. 2.1 all states with velocity scaling up to v^4. This approach is well justified for bottomonium states, due to their small v, but the hierarchy might be more difficult to constrain for charmonium, with its larger v.

Under these considerations, the main contributions for S-wave states will be the intermediate states ${}^3S_1^{[1]}$, ${}^1S_0^{[8]}$, ${}^3S_1^{[8]}$ and ${}^3P_J^{[8]}$. For P-wave states, the main contributions will be ${}^3P_J^{[1]}$ and ${}^3S_1^{[8]}$.

Colour-Singlet Model

From a purely theoretical perspective, the contribution to S-wave quarkonium states that is scaled by the lowest power of v is the colour-singlet $Q\overline{Q}$ pair with state n identical to that of the final quarkonium: the ${}^3S_1^{[1]}$ intermediate state. In the limit of small velocity, only this term is considered, and the framework that has been described reduces to the simpler Colour-Singlet Model (CSM). In this model, the quantum state of the pair does not evolve between its production and its hadronization, neither in spin nor in colour. In this way, it can be considered a special case of the NRQCD factorization framework, obtained when Eq. 2.1 contains only a single colour-singlet intermediate state, the ${}^3S_1^{[1]}$ for S-wave states and the ${}^3P_J^{[1]}$ for the P-wave.

Due to the simplicity of the transition of the intermediate $Q\overline{Q}$ state into the quarkonium state in this case, with no alteration in quantum numbers or non-perturbative emission of soft gluons, the LDMEs for these colour-singlet states can be calculated with high precision, and determined experimentally through the measurement of the decay widths of quarkonium states, leading to a model with no free parameters [13]. While this framework works well, from a theoretical perspective, for the S-wave states, in the case of the P-wave states, considering only the colour-singlet states leads to infrared divergences. Adding the colour-octet terms to the sum resolves this issue.

The ability of NRQCD and the CSM to describe experimental results will be discussed further in Section 2.4. Before this can be done, another important observable must be introduced: the quarkonium polarization, which is the subject of Section 2.3.

2.3 Quarkonium polarization

The discussion in this section focuses on S-wave quarkonia, which are vector states of the form 1^{--}, and particularly on the two-body lepton decay $\mathcal{Q} \to \ell^+\ell^-$ of these states. Both experimentally and theoretically, this decay channel provides the cleanest way of measuring quarkonium production yields and polarizations. The polarization of χ states is mentioned briefly, for completeness.

An S-wave quarkonium state can be observed in three eigenstates of J_z, the angular momentum component with respect to a quantization axis z: $J_z = 0, \pm 1$. The state will be considered polarized, with respect to the axis z, if it is dominantly observed in one of these states, and unpolarized if it is found in each eigenstate with equal probability. These particles are said to be “transversely” polarized when $J_z = \pm 1$ and “longitudinally” polarized when $J_z = 0$ [29].

In two-body decays, the shape of the angular distribution of the two decay products (emitted back-to-back in the quarkonium rest frame, so that only one needs to be studied) reflects the polarization of the quarkonium state. An isotropic (spherically symmetric) distribution corresponds to unpolarized quarkonium production, while the decay of a polarized state will lead to anisotropies shaping the angular distribution.

In order to measure this distribution, it is necessary to define a coordinate system, and then to define the momentum of one of the two decay products with respect to it, in spherical coordinates. In inclusive quarkonium measurements, the directions of the two colliding beams provide the physical reference for the coordinate system, by making the plane containing the momenta of the colliding beams (called the "production plane") define the xz plane, so that the y direction is perpendicular to it. The polar angle ϑ is determined by the direction of one of the two decay products with respect to the chosen polar axis z, and the azimuthal angle φ is measured with respect to the production plane. These definitions are illustrated in Fig. 2.4.

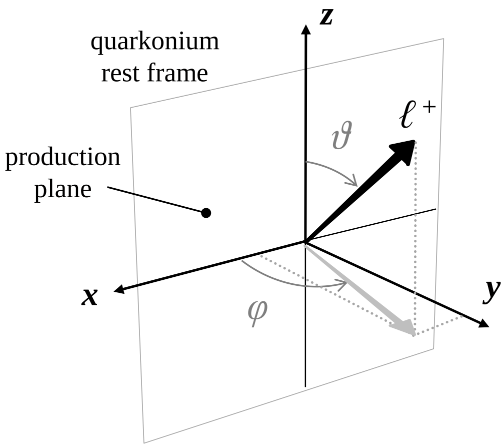

Figure 2.4: The coordinate system used to define ϑ and φ of the decay product (in this case the ℓ^+) in the quarkonium rest frame. The y axis is perpendicular to the production plane and the z axis can be defined in different ways, depending on the selected convention [29].

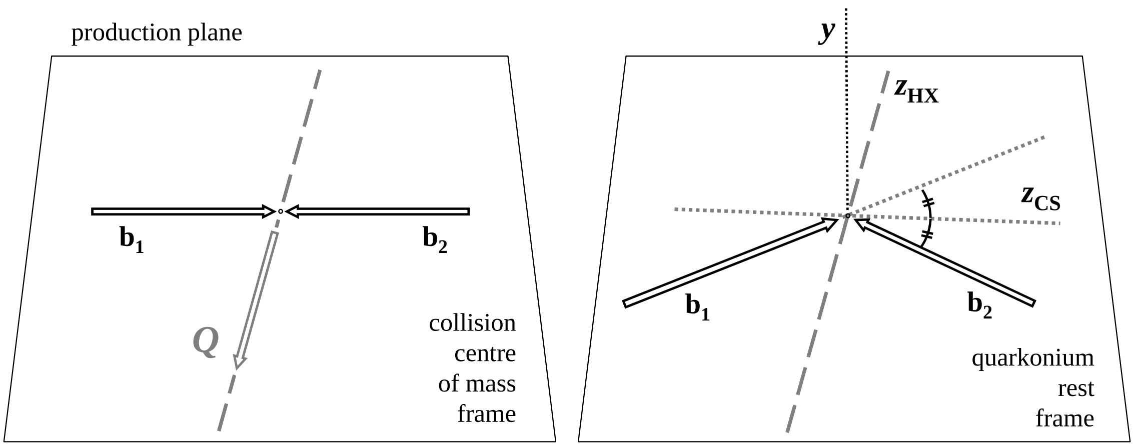

Figure 2.5: Illustration of the two definitions of the polar axis z given in the text, Collins–Soper (CS) and helicity frame (HX), with respect to the directions of motion of the two colliding beams ($b_{1,2}$) and of the quarkonium (Q). Adapted from Ref. [29].

The definition of reference frame is not unique, with more than one convention for the orientation of the polar axis being used in measurements, each with its own physical motivation. Two of these are illustrated in Fig. 2.5. The helicity frame (HX) uses the flight direction of the quarkonium in the centre of mass (CM) of the colliding beams, which translates to the opposite of the direction of motion of the interaction point in the quarkonium rest frame. The Collins–Soper (CS) frame [54] uses the bisector of the angle between one beam and the opposite of the other. When the quarkonium is produced at high transverse momentum p_{T} and negligible longitudinal momentum p_{L} (both defined relative to the beam axis), these two frames differ by a rotation of 90° around the y axis.

The angular decay distribution of a vector state can be calculated from basic quantum mechanical considerations, imposing helicity conservation for massless fermions at the photon-dilepton vertex of the dilepton decay. Using the appropriate rotation matrices to perform a change of quantization axis that introduces the angles ϑ, φ, one obtains [29]

$$W(\cos\vartheta, \varphi|\vec{\lambda}) = \frac{3}{4\pi\,(3+\lambda_\vartheta)} \left(1 + \lambda_\vartheta \cos^2\vartheta + \lambda_\varphi \sin^2\vartheta \cos 2\varphi + \lambda_{\vartheta\varphi} \sin 2\vartheta \cos\varphi\right), \tag{2.2}$$

where $\vec{\lambda} = (\lambda_\vartheta, \lambda_\varphi, \lambda_{\vartheta\varphi})$ are the three "anisotropy parameters" or "polarization parameters" that characterize the distribution. The parameter λ_ϑ describes the polar anisotropy of the decay, λ_φ the azimuthal anisotropy, and $\lambda_{\vartheta\varphi}$ the change of the azimuthal anisotropy as a function of the polar angle.

The polar anisotropy parameter λ_ϑ is positive for transverse polarization, and negative for longitudinal, taking the value +1 (-1) for a fully transverse (longitudinal) polarization. The unpolarized case is characterized by the set of polarization parameter values $\vec{\lambda} = (0, 0, 0)$. It should be noted that the obtained definitions of the λ parameters as functions of the decay amplitudes of $\mathcal{Q}$ is such that no configuration results in the unpolarized case: the angular distribution of a $J = 1$ state is never intrinsically isotropic, although a specific superposition of different production processes could still lead to a precise cancellation of all decay parameters [29].

In the case of n contributing production processes, each with a relative weight $f^{(i)}$, the most general observable distribution takes the form

$$\begin{aligned} W(\cos\vartheta, \varphi) &= \sum_{i=1}^{n} f^{(i)} W^{(i)}(\cos\vartheta, \varphi) \\ &\propto \frac{1}{3+\lambda_\vartheta} \left(1 + \lambda_\vartheta \cos^2\vartheta + \lambda_\varphi \sin^2\vartheta \cos 2\varphi + \lambda_{\vartheta\varphi} \sin 2\vartheta \cos\varphi\right), \end{aligned} \tag{2.3}$$

where $W^{(i)}(\cos\vartheta, \varphi)$ is the decay distribution corresponding to a single subprocess, as defined in Eq. 2.2. Each of the three observable parameters $X = \lambda_\vartheta$, λ_φ and $\lambda_{\vartheta\varphi}$ is a weighted average of the corresponding parameters $X^{(i)}$ of each subprocess,

$$X = \frac{\sum_{i=1}^{n} \frac{f^{(i)}}{3+\lambda_\vartheta^{(i)}} X^{(i)}}{\sum_{i=1}^{n} \frac{f^{(i)}}{3+\lambda_\vartheta^{(i)}}}. \tag{2.4}$$

This sum rule is useful for calculations considering feed-down decays, used when combining the angular distributions of the different contributions. It is also useful in the addition of the polarizations of the individual colour channels in NRQCD calculations.

Just as it was observed that the definitions of the λ parameters as functions of the decay amplitudes of $\mathcal{Q}$ mean that the case $\vec{\lambda} = (0, 0, 0)$ is impossible, other conclusions can be derived from these definitions. In particular, a set of inequalities called the "positivity constraints" [28], obtained in this way, define the allowed regions for the decay angular parameters, as shown in Fig. 2.6, in grey.

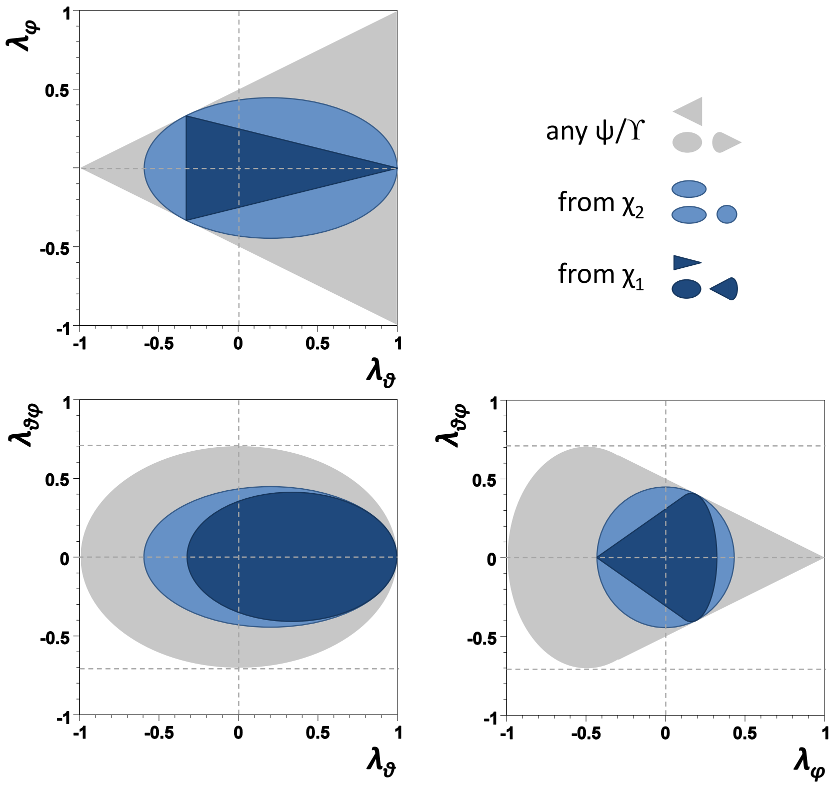

Figure 2.6: Allowed regions for the λ parameters of vector states of any origin (grey) and of χ_1 (dark blue) and χ_2 (light blue) daughters in radiative decays [30].

2.3.1 Polarization of χ states

The measurement of the P-wave quarkonia is experimentally more challenging. The radiative decay $\mathcal{Q}^{^3P_J} \to \mathcal{Q}^{^3S_1} + \gamma$ requires, in principle, both the information on the lepton pair from the $\mathcal{Q}^{^3S_1} \to \ell^+\ell^-$ decay and on the photon, which can be difficult to reconstruct and measure reliably. Despite these difficulties, the polarization of the χ states is an important ingredient in the understanding of S-wave polarization patterns, due to the feed-down chains in each of the quarkonium families and the fact that, as mentioned previously, S-wave state measurements don't typically distinguish between directly-produced states and those resulting from the decay of higher-mass states.

In the most straightforward approach, this measurement would consist of determining the angular distribution of the $\mathcal{Q}^{^3S_1} + \gamma$ system in the $\mathcal{Q}^{^3P_J}$ rest frame. This would require reconstructing the photon very precisely, in terms of kinematics and detection efficiencies, in order to have reliable results. In current detectors, the associated experimental uncertainties would most likely be dominant. However, it has been shown in Ref. [30], through a rigorous calculation of the angular distributions of the two-step decay, that, at high enough total dilepton momentum, the angular distribution of the $\mathcal{Q}^{^3S_1} \to \ell^+\ell^-$ decay in the $\mathcal{Q}^{^3S_1}$ rest frame is identical to that of the $\mathcal{Q}^{^3P_J} \to \mathcal{Q}^{^3S_1} + \gamma$ decay in the $\mathcal{Q}^{^3P_J}$ rest frame. This approximation introduces a negligible bias for the momentum ranges accessible at the LHC experiments, so that a χ polarization measurement using LHC events can be done (as for the S-wave states) by measuring the angular decay distribution of the dilepton decay, requiring only the identification of an additional photon originating from the dilepton vertex such that the $\mathcal{Q}^{^3S_1} + \gamma$ system has an invariant mass compatible with coming from a $\mathcal{Q}^{^3P_J}$ decay.

As for the S-wave states, the positivity constraints for the P-wave states can be derived from the definitions of the λ parameters, determining their allowed regions. These are also shown in Fig. 2.6, in dark and light blue for the $J = 1$ and $J = 2$ states, respectively.

2.3.2 Frame dependence of the polarization measurement

One concept relevant for the discussion ahead is the "natural" polarization axis or frame. When a quarkonium state is produced, it acquires its polarization with respect to this natural frame. In an experimental context, this frame varies event-by-event, depending on the momentum of the produced $\mathcal{Q}$, and only the resulting superposition of many distributions can be measured, but the frame closest to the natural frame will be the one providing the smallest value of λ_φ and $\lambda_{\vartheta\varphi}$[1] and the largest $|\lambda_\vartheta|$ [25].

Assuming that a measurement is performed in the natural frame, one might be tempted to limit it to the most significant parameter, λ_ϑ. However, if this assumption is incorrect, the resulting measurement is imbued with ambiguity. This is illustrated in Fig. 2.7, showing two reference frames for each of two polarization scenarios $J_z = \pm 1$ and $J_z = 0$. The distributions a) and c) correspond to the case where $J_z = \pm 1$. In the natural frame, given in a), a polarization measurement will obtain $\lambda_\vartheta = +1$ and $\lambda_\varphi = \lambda_{\vartheta\varphi} = 0$. However, in a frame corresponding to a rotation of 90°, given in c), the new λ parameters will be $\lambda'_\vartheta = -1/3$ and $\lambda'_\varphi = +1/3$. In a similar way, for $J_z = 0$, in the natural frame shown in b), $\lambda_\vartheta = -1$ and $\lambda_\varphi = \lambda_{\vartheta\varphi} = 0$, but in a frame rotated by 90°, shown in d), $\lambda'_\vartheta = +1$ and $\lambda'_\varphi = -1$ [29].

This means that, in the first case, an improper choice of frame of reference could "transform" a fully transverse polarization into a mixture of processes resulting in 50% transverse and 50% longitudinal natural polarization (for which $\lambda_\vartheta = -1/3$, according to Eq. 2.4), if one only considers the λ_ϑ parameter and assumes $\lambda_\varphi = \lambda_{\vartheta\varphi} = 0$. In the second case, a fully longitudinal polarization would be measured as fully transverse. Recalling that the HX and Collins–Soper frames differ by 90° when $p_\mathrm{T} \gg p_L$, this example reproduces the hypothesis that the quarkonium is naturally polarized along one frame and measured along the other, illustrating perfectly that a measurement consisting only in the determination of λ_ϑ is inherently incomplete.

This is only the "simplest" way in which the choice of reference frame impacts measurements. In reality, rather than determine a single polarization value, measurements are performed over a range of

[1] Physically, $\lambda_{\vartheta\varphi} = 0$ corresponds to aligning the axes of the frame along the principal symmetry axes of the polarized angular distribution.

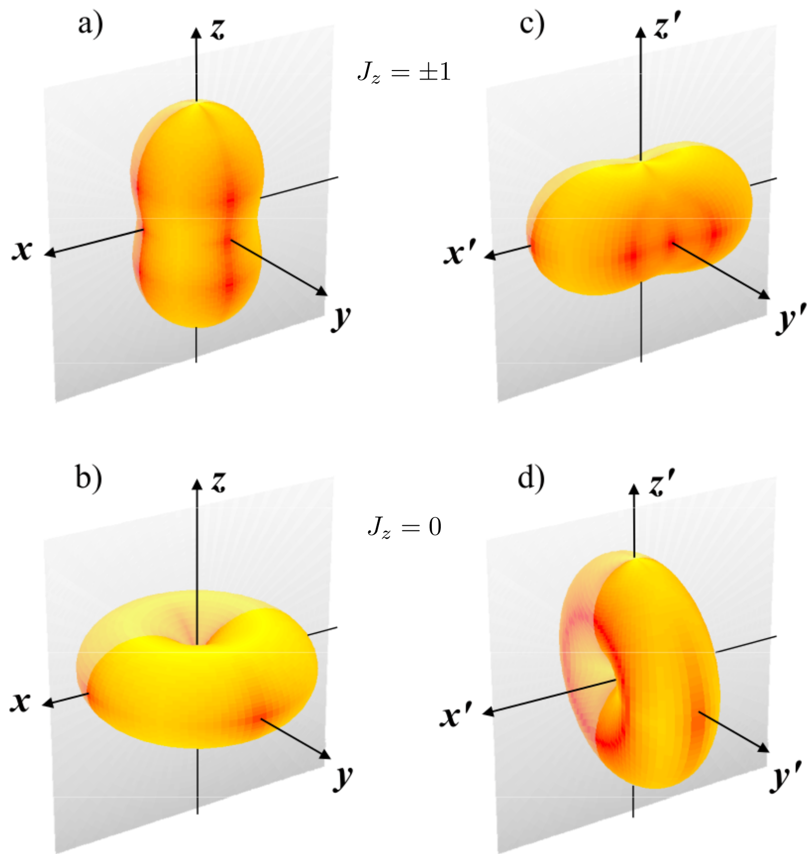

Figure 2.7: Graphical representation of the dilepton decay distribution of fully transverse (top) and fully longitudinal (bottom) quarkonium, in the natural frame (left) and in frames rotated by 90°. The probability of the lepton emission in one direction is represented by the distance of the corresponding surface point from the origin [29].

kinematic variables such as quarkonium momentum p and rapidity y, the latter defined as

$$y = \frac{1}{2}\ln\left(\frac{E+p_L}{E-p_L}\right), \tag{2.5}$$

with E the particle energy. The rapidity expresses the direction of the particle with relation to the beam, and the particle is considered to have "central" rapidity when $|y| \lesssim 1$, as opposed to "forward" or "backward" rapidity when $|y|$ takes larger values and y is positive or negative, respectively.

In this range, kinematic dependences will emerge naturally as a result of the varying relative weights of the individual processes contributing to the quarkonium production. These can be considered "intrinsic" kinematic dependences and are physically meaningful. However, considering once again the case of the HX and Collins–Soper frames being the experimental and natural frames, or vice-versa, the angle between the two polarization axes will vary as a function of the quarkonium momentum, so that a natural polarization with no intrinsic kinematic dependence will appear to be p_{T}-dependent when measured, introducing an "extrinsic" kinematic dependence, one that is fully induced by experimental limitations [29]. Many other systematic effects can also affect the measurement and cause an extrinsic kinematic dependence, such as detector geometry or data selection constraints, as well as the incorrect subtraction of background processes.

These considerations motivate the use of a frame-invariant approach. Since the polarization axis z is defined within the production plane in all experimentally definable configurations, any two polarization frames differ only by a rotation around the y axis. While the angular distribution will remain physically unchanged, the measured polarization parameters λ will vary as a function of the rotation angle δ. Based on these frame-transformation relations, one can find frame-invariant quantities, definable in terms of the λ_ϑ, λ_φ and $\lambda_{\vartheta\varphi}$ parameters [29]. These quantities are, by definition, immune to the extrinsic kinematic dependences that affect the measurement, and will therefore be less sensitive than the standard anisotropy parameters to differences in kinematic conditions between measurements. One frame-invariant parameter commonly used is

$$\tilde{\lambda} = \frac{\lambda_\vartheta + 3\lambda_\varphi}{1 - \lambda_\varphi}, \tag{2.6}$$

which is +1 for any fully transverse shape and -1 for any fully longitudinal shape. In the case of multiple contributing processes, each polarized along its respective polarization axis, the resulting $\tilde{\lambda}$ will represent a weighted average of the polarizations, unaffected by the orientations of the corresponding axes.

Aside from providing physics information, the $\tilde{\lambda}$ parameter can also be an experimental cross-check. By comparing the parameter in several frames, one can evaluate the level of systematic errors not accounted for in the analysis.

2.3.3 Polarization of non-prompt charmonia

A non-prompt (NP) sample, identified using the displacement between production and decay of the parent b-hadron as mentioned in Section 2.1, can be analyzed in the same way as the prompt case, resulting in a measurement of non-prompt quarkonium polarization. However, the interpretation of this measurement is not as straightforward. Reference [55] explores the necessary considerations, focusing on the case of the NP J/ψ, which contributes significantly to the inclusive J/ψ sample in the LHC kinematic conditions and is mostly due to B meson decays.

A J/ψ produced from a decay of a B meson, $B \to \mathrm{J}/\psi + X$, where X can be a particle or a multi-body system, is polarized intrinsically along the direction of its emission in the B rest frame. Given that the X product is usually undetected, however, the B kinematics cannot be reconstructed, and the B rest frame is unavailable. A measurement performed in the J/ψ rest frame, instead, will result in a smeared polarization: the polarization axes vary with respect to each other for each event and the resulting measurement is of unpolarized J/ψ.

In practice, the measurement using J/ψ kinematics impacts the decay distribution further, as cuts in the dilepton kinematic variables will sculpt the (unmeasured) B distributions, so that the smearing will no longer be spherically symmetrical. This results in a visibly anisotropic decay angular distribution of the J/ψ state. Further, the nature of the X product will impact the polarization as well. In the "two-body" case, where X is a kaon or similar light particle of $J(X) = 0$, the J/ψ is fully longitudinally polarized along its direction of production. The complementary "multi-body" case congregates all other decays, where X is a system of particles, or $J(X) \neq 0$, or the J/ψ is produced in a feed-down decay from a heavier quarkonium state. In the former case the smearing is less severe than in the latter, where the natural polarization is smaller and the smearing has a stronger impact, resulting in a measured polarization of much smaller magnitude.

The two complementary decay topologies considered are further distinct in terms of the J/ψ production process. While the two-body case is dominated by singlet production, through the intermediate colour-singlet state ${}^3S_1^{[1]}$, the multi-body case should include contributions from colour-octet $Q\overline{Q}$ states [56, 57, 58]. Understanding the relative weight of each decay topology can thus provide information on the charmonium production mechanism.

2.4 Agreement between theory and data

Quarkonium physics, due to its complex nature, has had a troubled history both on the theoretical and the experimental side. While enormous progress has been made in resolving disagreements and inconsistencies, some of these issues affect the field to this day. As such, it is useful to offer a short overview of the chronological developments in the field of quarkonium production, from the pre-LHC era to the current LHC results, and the accompanying developments in the theory.

The CSM, briefly mentioned in Section 2.2, was the first model to gain prominence in the aftermath of the first quarkonium measurements in the 70s [41, 42, 43]. With the ability to calculate quarkonium production cross sections with no free parameters, the CSM was successful in predicting quarkonium production rates at relatively low energy [59], although experimentally measured cross sections at increasing energies were found to be significantly higher than the predictions [60, 61]. As the measurements covered higher values of p_{T} [17] with no improvement in agreement with theory, the possibility of unaccounted-for non-perturbative effects causing this difference had to be discarded and the discrepancy acknowledged. It was particularly alarming for the $\psi(2\mathrm{S})$, which was unaffected by feed-down decays, so that its (direct) measurement should coincide with the theory predictions, with no unknown contributions affecting the experimental result. Instead, the CSM predictions underestimated the observed yields by a factor of 40–50, a problem known as the "$\psi(2\mathrm{S})$ anomaly".

The NRQCD approach was introduced at this time, expanding the simpler CSM by including also colour-octet contributions. Comparing this theory to the data required a fit where the colour-octet LDMEs were left as free fit parameters, and it was found that this approach agreed nicely with the same data that had caused such trouble for the CSM [20]. This success, however, was not satisfactory, given the freedom of the fit: it was not too challenging to obtain a good-quality description of the measured p_{T}-differential cross section with a superposition of four terms with totally free normalizations. It was important to verify the validity of NRQCD, by fixing the fitted LDMEs and predicting another observable that could be compared to experimental measurements: the polarization.

Each $Q\overline{Q}$ intermediate state has its characteristic polarization in the NRQCD factorization approach, with a set of λ parameters, with respect to the chosen polarization axis z, as functions of p_{T}. The polarization parameters can be calculated by defining the SDCs corresponding to the individual projections

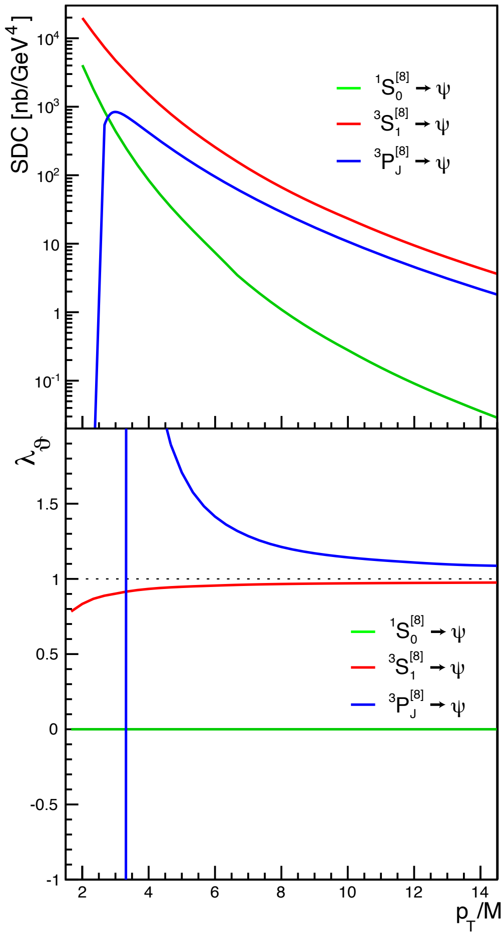

Figure 2.8: SDCs (top) and corresponding λ_ϑ in the HX frame (bottom), for the main components of directly-produced $\psi(nS)$ mesons, calculated at NLO [63, 64] for pp collisions at $\sqrt{s} = 7$ TeV and a charmonium mass of 3 GeV. The $^3P_J^{[8]}$ SDC function is multiplied by m_c^2 and plotted with flipped sign as it becomes negative at high $p_{\rm T}$ $/M$, where M is the mass of the quarkonium state [32].

of the $Q\overline{Q}$ spin S on the polarization axis z, S_{ij}, with the notation $i, j = 0, \pm 1$ [62],

$$\lambda_\vartheta = \frac{S_{11} - S_{00}}{S_{11} + S_{00}}, \quad \lambda_\varphi = \frac{S_{1,-1}}{S_{11} + S_{00}}, \quad \lambda_{\vartheta\varphi} = \frac{\sqrt{2}\,\mathrm{Re}\,S_{10}}{S_{11} + S_{00}}. \tag{2.7}$$

The LDMEs fitted from the production cross section measurements can then be used to predict the polarization of the measured sample, weighing the $\vec{\lambda}$ distributions of each contributing intermediate state.

As an example of the kinematic diversity observed in these distributions, the Next-to-Leading Order (NLO) SDCs and corresponding HX-frame λ_ϑ polarization parameters are shown in Figure 2.8, for the main contributions to the $\psi(nS)$ states, $^1S_0^{[8]}$, $^3S_1^{[8]}$ and $^3P_J^{[8]}$. The $^3S_1^{[1]}$ colour-singlet contribution is not shown since, as was discussed regarding the $\psi(2\mathrm{S})$ anomaly, it has been determined that its SDC leads to negligible yields in comparison to the observed prompt cross sections.

The three colour-octet states have very different polarizations, from the unpolarized $^1S_0^{[8]}$ to the $^3S_1^{[8]}$ that tends towards fully transverse polarization at high $p_{\rm T}$, and the $^3P_J^{[8]}$ showing unphysical values of $|\lambda_\vartheta| > 1$. Recalling that only the linear combination of LDMEs and SDCs given in Eq. 2.1 is a physical quantity, and not necessarily each of the component terms, this is not an issue in and of itself, but it does mean that the relative contribution of each $Q\overline{Q}$ state must be such that any unphysical behaviour is cancelled in the sum.

This diversity of λ_ϑ makes the polarization dimension a great probe of the validity of NRQCD and the LDMEs determined from cross section data fits. In this view, several groups conducting Leading Order (LO) NRQCD calculations made their polarization predictions for the Tevatron J/ψ and $\psi(2\mathrm{S})$ production, finding strongly transverse polarization in the HX frame, especially at high p_T (see Ref. [13] and references therein). However, the CDF Collaboration measured no large polarizations [21, 22]. The CDF measurements for Run 2 and the corresponding NRQCD predictions are compared in Fig. 2.9, illustrating this clear disagreement.

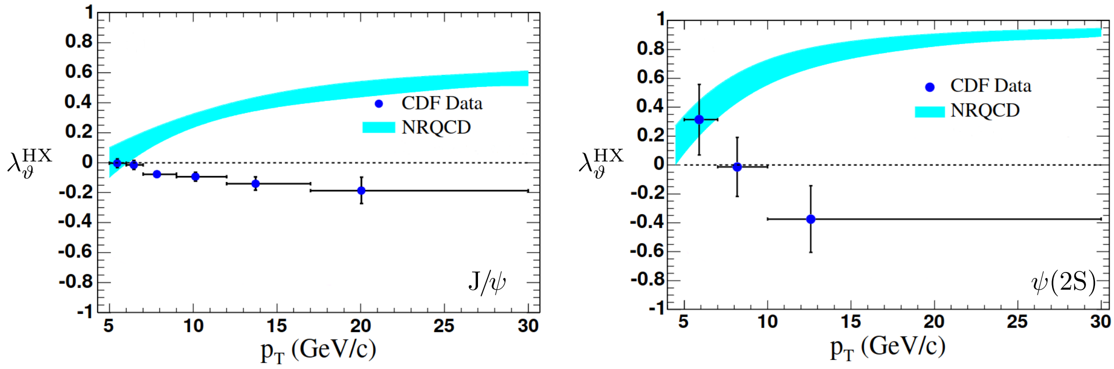

Figure 2.9: Prompt J/ψ (left) and $\psi(2\mathrm{S})$ (right) polar anisotropy parameter in the HX frame $\lambda_\vartheta^{\mathrm{HX}}$, measured by the CDF Collaboration at a CM energy of $\sqrt{s} = 1.96$ TeV [22] and compared to LO NRQCD calculations [24] including feed-down contributions. Adapted from Ref. [22].

2.4.1 The quarkonium polarization puzzle

Figure 2.9 illustrates what has come to be known as the “polarization puzzle” of quarkonium production: the theory’s good agreement with cross section measurements, yet inability to describe the measured polarization.

In response to this puzzle, there was an effort on the theory side to improve the NRQCD calculations, extending them from LO to NLO in order to run new fits and obtain updated polarization predictions [62, 65, 63]. Although there was great success in reproducing the cross sections of different collision systems, the predicted polarizations remained similar to those of the LO fits, strongly transverse in the HX frame, and the puzzle remained.

Finding a large difference between LO and NLO colour-singlet results, which opened the possibility that the colour-singlet ${}^3S_1^{[1]}$ state could have a significant contribution after all, partial Next-to-Next-to-Leading Order (NNLO) corrections for the colour-singlet ${}^3S_1^{[1]}$, denoted as NNLO*, were also calculated and compared with the data [66, 67, 68], although it was found that the colour-singlet contribution alone still could not reproduce the data and the colour-octet terms continued to be needed.

Another further complication at this time was on the experimental side, with the Tevatron experiments CDF and D0 publishing polarization measurements that were mutually inconsistent, as shown in Fig. 2.10. The left panel compares the CDF measurements of prompt J/ψ polarization in the HX frame

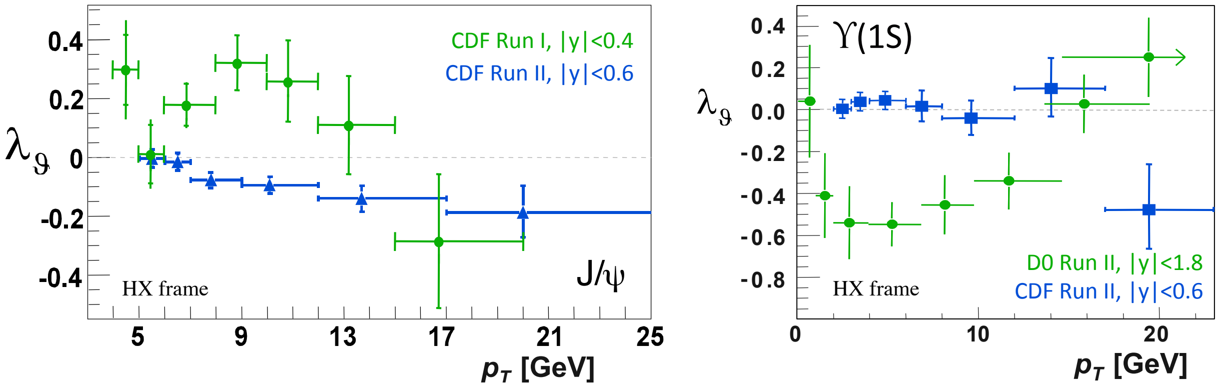

Figure 2.10: Measurements of the polar anisotropy parameter λ_ϑ in the HX frame, by the Tevatron experiments, for the prompt J/ψ (left, [21, 22]) and for the $\Upsilon(1S)$ (right, [69, 23]).

from the data-taking Runs 1 and 2 [21, 22]. The results are clearly incompatible within associated uncertainties, far more than the slight change in data-taking conditions could explain: the CM energy changes from 1.8 to 1.96 TeV and the rapidity region is increased from $|y| < 0.4$ to $|y| < 0.6$. On the right panel, $\Upsilon(1S)$ polarization measurements in the HX frame are compared between the CDF Run 2 [69] and D0 Run 2 [23], both taken at $\sqrt{s} = 1.96$ TeV. Again, there is a large difference that cannot be justified by the difference in rapidity region of each measurement.

The inability of the theory to reproduce the polarization results, coupled with the inconsistencies seen in the polarization measurements themselves, was an unfortunate combination that undermined the value of the polarization dimension in all subsequent discussions of the topic. Considering the strong discriminating power of the polarization dimension, as illustrated in Fig. 2.8, the loss of information is far from negligible.

Although it was never established why the Tevatron experiments were plagued by such inconsistencies, the discussion in Section 2.3.2 provides a possible explanation. The decision to only measure the polar anisotropy λ_ϑ and only in the HX frame, implicitly assuming that λ_φ is zero in that frame, left the measurements in the delicate situation of extreme ambiguity illustrated in that section. Any experimental issues or biases potentially arising in the process of the measurement could have gone unnoticed, with no cross-check to uncover such systematic problems.

2.4.2 Quarkonium measurements at the LHC

Just as the quarkonium polarization puzzle motivated efforts towards the improvement of SDC calculations and a better modelling of quarkonium production on the theory side, the inconsistencies of the polarization measurements at the Tevatron experiments drove significant progress in understanding quarkonium polarization and the methodology required for the corresponding measurements [25, 26, 27, 28, 29, 30], some of which is documented in Section 2.3. Following this methodology, all quarkonium polarization measurements conducted at hadron colliders have since shown consistent results throughout various experiments.

Driving these results are the four LHC experiments, which have performed cross section and polarization measurements for multiple quarkonium states, at various collision energies and in different kinematic regions. The prompt (or inclusive, combining prompt and non-prompt) production cross sections of $\psi(nS)$ states have been measured by CMS [70, 71, 72, 73], ATLAS [74, 75, 76], LHCb [77, 78, 79, 80, 81, 82] and ALICE [83, 84, 85, 86, 87, 88, 89]. $\Upsilon(nS)$ production cross section measurements have also been reported by all four experiments CMS [73, 90], ATLAS [75, 91], LHCb [80, 92, 93, 94, 95] and ALICE [86, 87]. In terms of polarization, CMS has reported measurements for the promptly-produced J/ψ and $\psi(2\mathrm{S})$ [37], as well as for the $\Upsilon(nS)$ states [38], as has LHCb [39, 96, 97]. ALICE has reported polarization measurements only for inclusive J/ψ production [36, 98].

These measurements supplement earlier measurements by the Tevatron experiments, mostly $\psi(nS)$ and $\Upsilon(nS)$ production cross sections measured by CDF [17, 99, 100, 101, 16, 102, 103] and D0 [19, 104, 105]. There are also updated polarization results from CDF, for the $\Upsilon(nS)$ [103, 35].

For the S-wave states $\psi(nS)$ and $\Upsilon(nS)$, there are cross section measurements for multiple CM energies, covering wide p_{T} and y ranges. At central rapidity, the statistical reach of existing data extends up to a p_{T} of around 100 GeV, with some variations between states, while at forward rapidity the measurements are up to around 30 GeV. There is also at least one polarization measurement for each of these states, although the statistically demanding nature of these measurements limits them to lower p_{T} regions.

The P-wave state measurements have mainly been restricted to cross section ratios [106, 107, 108, 109], with only ATLAS providing a cross section measurement for the two states χ_{c1} and χ_{c2} individually [110]. The first polarization measurement for P-wave states was performed recently by CMS, constraining the difference between the χ_{c1} and χ_{c2} polarizations [111].

The polarization measurements for the S-wave charmonium and bottomonium states, from the LHC and Tevatron experiments, using the updated methodology, show a clear consistency across kinematic ranges and collision energies. They show, furthermore, λ_φ and $\lambda_{\vartheta\varphi}$ parameters in the HX frame compatible with zero within uncertainties, supporting the assumption that, in the data-taking conditions of these experiments, the HX frame is close to the natural one. Given this, for the rest of this thesis, the HX frame is assumed unless otherwise stated. Figure 2.11 shows the measured λ_ϑ for these experiments.

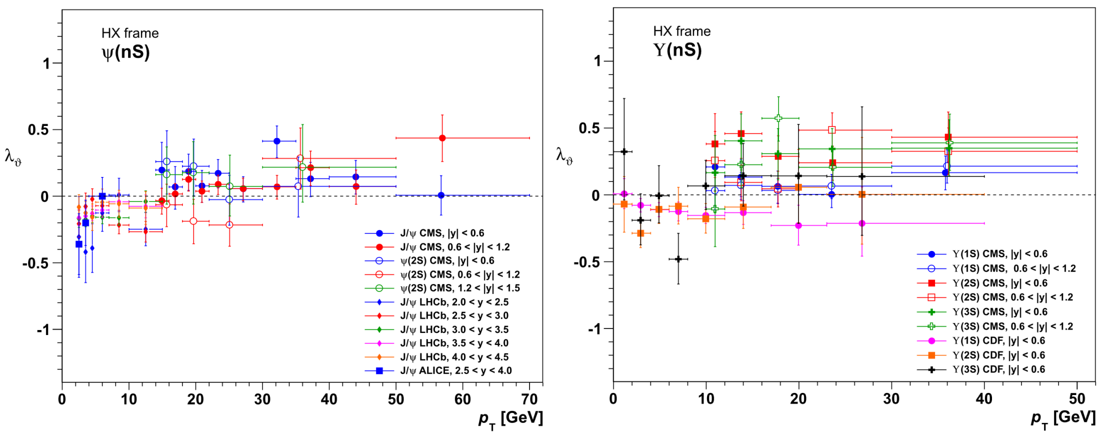

Figure 2.11: Measured λ_ϑ of charmonium (left) and bottomonium (right) states, by CDF [35], ALICE [36], CMS [37, 38] and LHCb [39]. Adapted from Ref. [31].

The LHC results, expected to be free from the issues of past measurements, all show nearly unpolarized production. This continues to be at odds with the theory predictions of strongly transverse polarization, as shown in Fig. 2.12, which compares the CMS 7 TeV polarization results for J/ψ (left panel) and $\psi(2\mathrm{S})$ (right panel) [37] with several NLO NRQCD calculations [112, 65, 63]. The clear conclusion is that the polarization puzzle cannot be attributed to experimental issues.

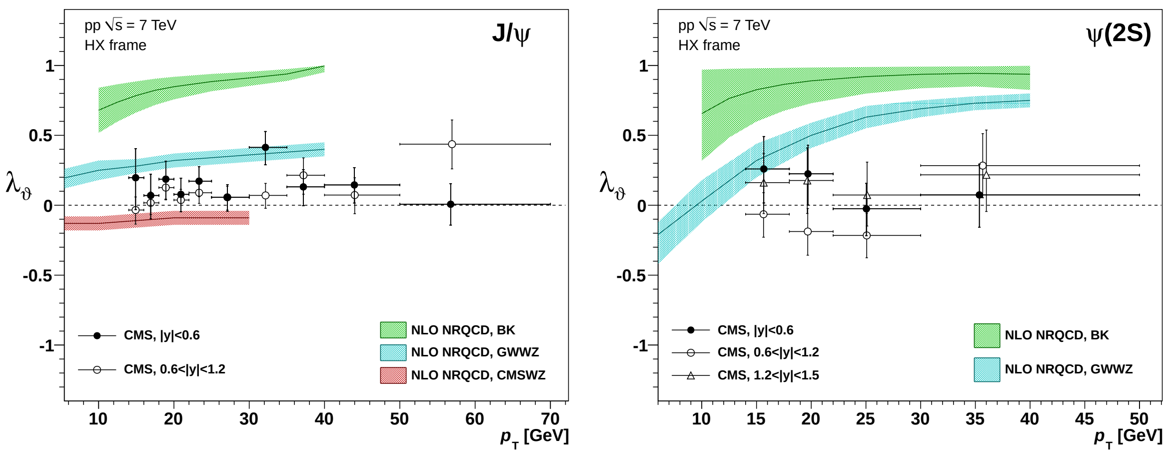

Figure 2.12: Measured λ_ϑ of 7 TeV prompt J/ψ (left) and $\psi(2\mathrm{S})$ (right) by CMS [37], compared to several polarization predictions from NLO NRQCD: BK [112], GWWZ [65], CMSWZ [63]. From Ref. [113].

2.4.3 Non-prompt charmonium measurements

Several production cross section measurements have been reported for the NP charmonia, commonly published together with the prompt measurements. At the LHC, measurements have been reported by CMS [70, 71], ATLAS [74, 75, 76, 110], LHCb [77, 78, 80, 81, 82] and ALICE [84, 89].

For the NP polarization, the experimental panorama is much poorer. The only existing measurement in the case of hadron collisions was performed by CDF [21], determining λ_ϑ in $p\overline{p}$ collisions at $\sqrt{s} = 1.8$ TeV, for p_T between 4 and 20 GeV and $|y| < 0.6$. The data are shown in Fig. 2.13, together with predictions based on a simulation described in Ref. [55], for the two-body and multi-body cases discussed in Section 2.3.3. The multi-body λ_ϑ prediction is compatible with NRQCD calculations of non-prompt J/ψ polarization in the CDF conditions, where colour-octet contributions are found to dominate [114, 115].

The precision of the data is not sufficient to distinguish between the two-body and multi-body cases. A measurement of NP quarkonium polarization performed at a high-energy hadron collider such as the LHC should have enough statistics to determine the relative contribution of each case, given the large difference in λ_ϑ between the two.

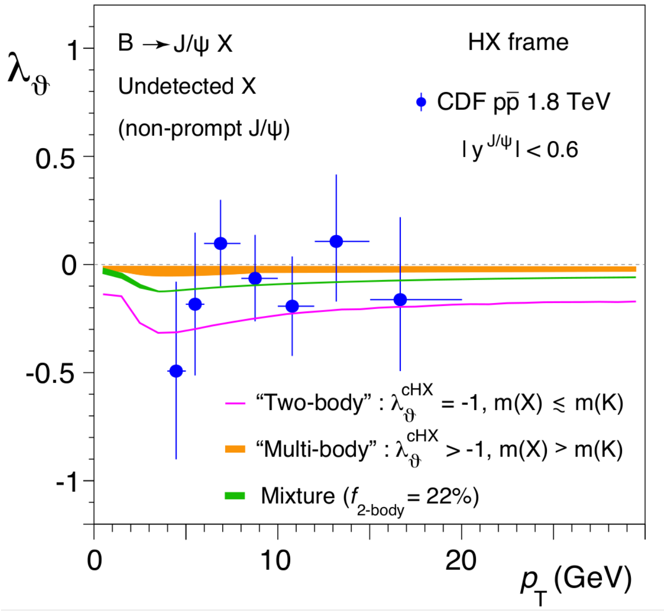

Figure 2.13: Polarization parameter λ_ϑ measured by CDF [21] for NP J/ψ in $p\bar{p}$ collisions at $\sqrt{s} = 1.8$ TeV, as a function of p_T, for $|y| < 0.6$ (blue markers), compared to predictions from the two-body (pink curve) and multi-body (orange band) cases, as well as a mixture of the two (green band), as described in Ref. [55].

2.5 Phenomenological interpretation of the experimental results

Given the developments in both experimental methodology and theory calculations, the apparent mismatch between predictions and measurements of the prompt polarization parameters remains a puzzle. But this conclusion overlooks one key ingredient: the comparison itself. The analysis reported in Ref. [31] highlights several elements that are crucial for a correct fit of the theory SDCs and LDMEs to the available measurements, and which can significantly alter the fit results: the treatment of the polarizations and of the low-p_T measurements.

When it comes to experimental measurements, the polarization and cross section dimensions are not uncorrelated. In fact, the polarization scenario significantly affects the cross section measurement due to the strong dependence of the acceptance determinations on the shape of the dilepton decay distributions, and the corrected production yields can vary by more than 50% depending on the assumed polarization. Taking this into consideration, the LHC experiments provide a measurement under a given hypothesis, the unpolarized case by default, and a further set of acceptance corrections that account for the dependence of each cross section data point on the polarization, making it possible to recalculate the cross sections *a posteriori* for any polarization hypothesis. However, previously-reported NRQCD global fits [116, 112, 63, 65], even those using the polarization as a constraint, did not apply these corrections, and thus compared theory curves corresponding to significantly polarized quarkonia to differential cross sections reported under the assumption of unpolarized production (i.e., obtained with acceptance corrections computed under that assumption).

In addition to this strong correlation, there is also the question of the region of validity of the SDCs. These are determined through perturbative calculations at fixed order in α_s, neglecting non-perturbative (low-p_{T}) effects. It cannot be expected that they reproduce the data down to arbitrarily low p_{T}, but rather that they should have a limit of validity, and thus that data fits should only be performed above this p_{T} threshold. This issue gains added significance when considering that measurements at low p_{T} often have the smallest uncertainties, therefore having a disproportionate weight in constraining the fit.

The analysis in Ref. [31] focused on the $\psi(2\mathrm{S})$ and $\Upsilon(3S)$ states, considered to be free of feed-down contributions, and took these elements into consideration. A series of fits was performed initially to determine the p_{T} cutoff for which the results stabilized, and the polarization was taken into account both as a constraint of the fit and in the form of an iterative correction to the cross section values. Having determined a threshold of $p_{\mathrm{T}}/M > 3$, it was possible in these conditions to fit both the cross section and polarization measurements, determining a dominant contribution of the unpolarized ${}^1S_0^{[8]}$ colour-octet. In this way, the same theory inputs and experimental measurements, which seemed so strongly mismatched, were found to be compatible, and the quarkonium polarization puzzle was solved.

2.5.1 A data-driven approach

The data-driven considerations of Ref. [31] were further developed into a fully data-driven approach in subsequent analyses [32, 33, 34]. Expanding the framework to include more quarkonium states and measurements at different collision energies, a pattern of universality is clear. When transformed to p_{T}/M distributions, the differential cross sections of the seven states $\psi(nS)$, $\Upsilon(nS)$ and $\chi_{c1,2}$ are well described, at mid-rapidity and for $p_{\mathrm{T}}/M > 2$, by a universal empirical function [32]. This is true both at $\sqrt{s} = 7$ and 13 TeV [34]. Additionally, the S-wave quarkonia appear nearly unpolarized, with no significant dependence on p_{T} or rapidity and no evident changes between charmonium and bottomonium or between directly-produced states and those affected by P-wave feed-down decays.

These results, illustrated in Figs. 2.11 and 2.14 for the polarizations and cross sections, respectively, seem at odds with the complexity of the NRQCD approach. This approach requires a linear combination of multiple terms with distinct kinematic dependences, as seen in Fig. 2.8 for the $\psi(nS)$ case, with the relative contributions and even the hierarchy of terms varying between states. In a comparison between states with almost pure S-wave or P-wave contributions or, due to feed-down effects, a mixture of the two, one would expect to see variations emerging from this diversity of production mechanisms. Instead, there is no experimental evidence of differences in production cross sections and polarizations between quarkonium states of different masses and quantum numbers, in the kinematic region covered by these measurements [32].

With this in mind, a fully data-driven fit of the charmonium measurements was attempted, accounting for the chain of feed-down decays and using, instead of the theory SDCs, an empirical power-law function. This resulted in two astounding conclusions. First, the available charmonium data can be described by a minimal set of contributions, universal across all states and reproducing both the shared p_{T}/M shape and the small measured polarizations. Second, the measurements are in agreement with NRQCD calculations, due to precise cancellations of the SDC shape differences [33].

A dimensional-analysis approach to the experimental data, at mid-rapidity and for $p_{\mathrm{T}}/M > 2$, per-

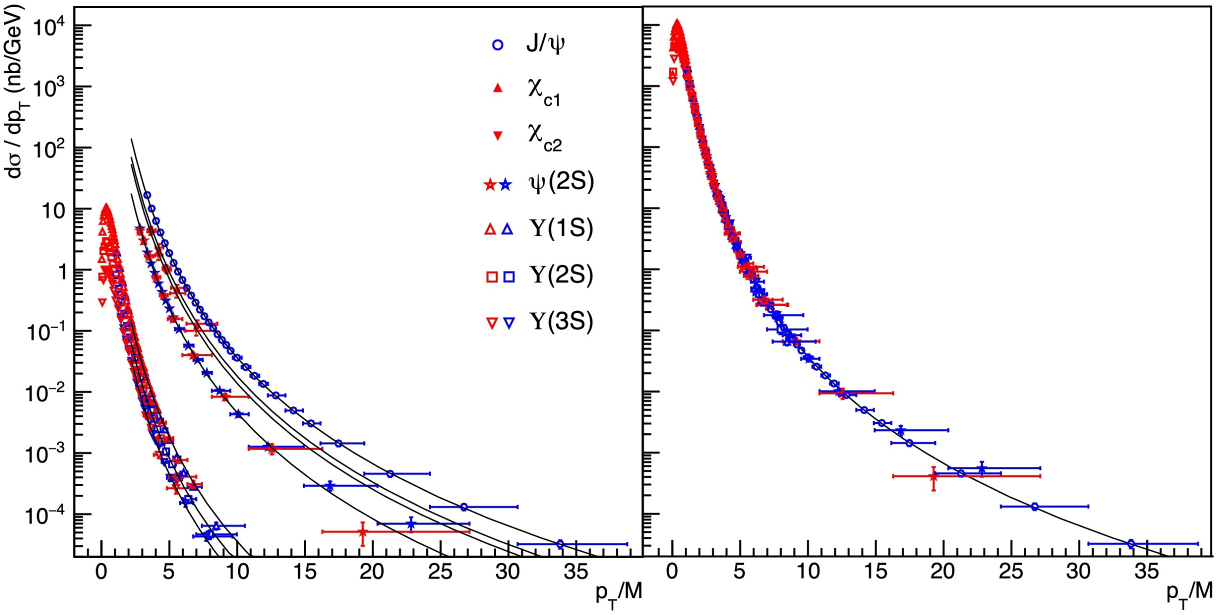

Figure 2.14: Prompt quarkonium cross sections at mid-rapidity measured in pp collisions at $\sqrt{s} = 7$ TeV by CMS (blue markers) [72, 90] and ATLAS (red markers) [75, 91, 110], as a function of $p_T\ /M$. The curves represent a single empirical function determined by a simultaneous fit to all data (with $p_T/M > 2$), with global shape parameters and normalizations specific to each state (left panel) or adjusted to the J/ψ points (right panel) [32].

formed in Ref. [34], also found experimental support for the NRQCD factorization hypothesis, which has not yet been demonstrated from first QCD principles [13].

2.5.2 Further probes of NRQCD

The seeming success of NRQCD in describing the unexpected simplicity of the data can be further tested with other measurements. One of these is in the χ sector, as the χ_c polarizations can be determined indirectly, within the NRQCD framework, using the available χ_{c2}/χ_{c1} cross section ratio measurements of CMS [106] and ATLAS [110]. This is because both the $\chi_{c1,2}$ polarizations and cross sections are functions of one global parameter K_χ, which can be determined from the ratios in an iterative procedure that takes the polarization into account for the acceptance corrections. The resulting K_χ, obtained in the "best-fit" case as described in Ref. [33], determines the $\chi_{c1,2}$ polarizations, as shown in Fig. 2.15. This polarization prediction is distinct from the mostly unpolarized measurements obtained for the S-wave states, as both the χ_{c1} and χ_{c2} have large polar anisotropies of opposite sign, especially at low p_T.

The recent experimental measurement of the $\chi_{c1,2}$ polarization difference by CMS [111], in pp collisions at $\sqrt{s} = 8$ TeV, while not allowing the determination of the λ_ϑ values themselves, strongly excludes the unpolarized hypothesis and shows good agreement with the NRQCD prediction. This is illustrated in Fig. 2.16, where the two hypotheses are used as input for $\lambda_\vartheta^{\chi_{c1}}$ and the resulting $\lambda_\vartheta^{\chi_{c2}}$ is determined.

A further data-driven fit of the charmonium sector, using the $\chi_{c1,2}$ polarization difference measurement as an added input, was able to obtain precise predictions for the direct $\psi(nS)$ polarization, determining $\lambda_\vartheta^\psi = 0.04 \pm 0.06$ with no significant p_T dependence [117]. This prediction raises, once again, the question of whether the unpolarized measurements are due to an accidental cancellation of the po-

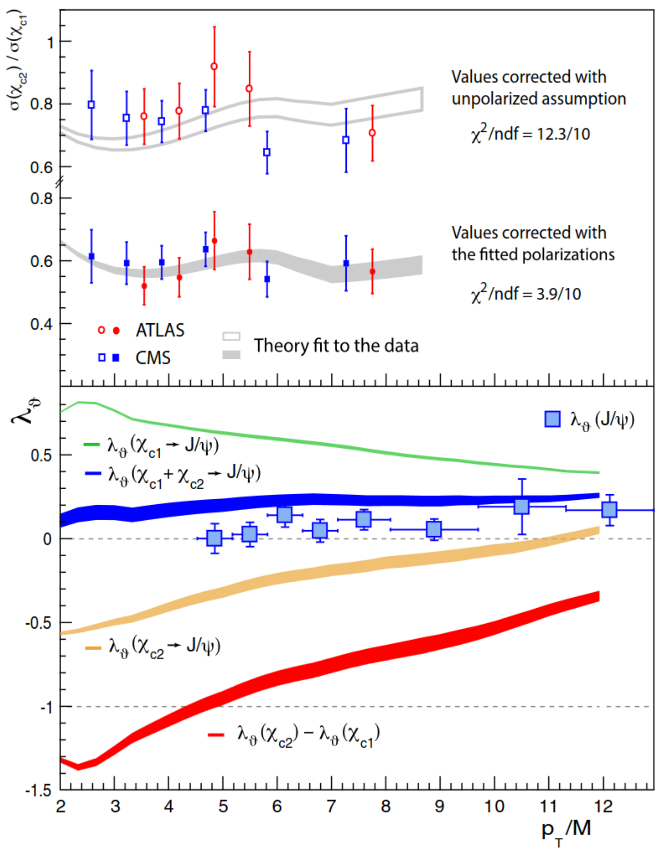

Figure 2.15: Top: χ_{c2}/χ_{c1} ratio measurements by CMS [106] and ATLAS [110], with acceptance corrections based on the unpolarized assumption (open markers) and with the "best-fit" polarizations (filled markers). The grey bands represent the respective theory fits. Bottom: The $\chi_{c1,2}$ polarizations, determined from the "best fit" [33].

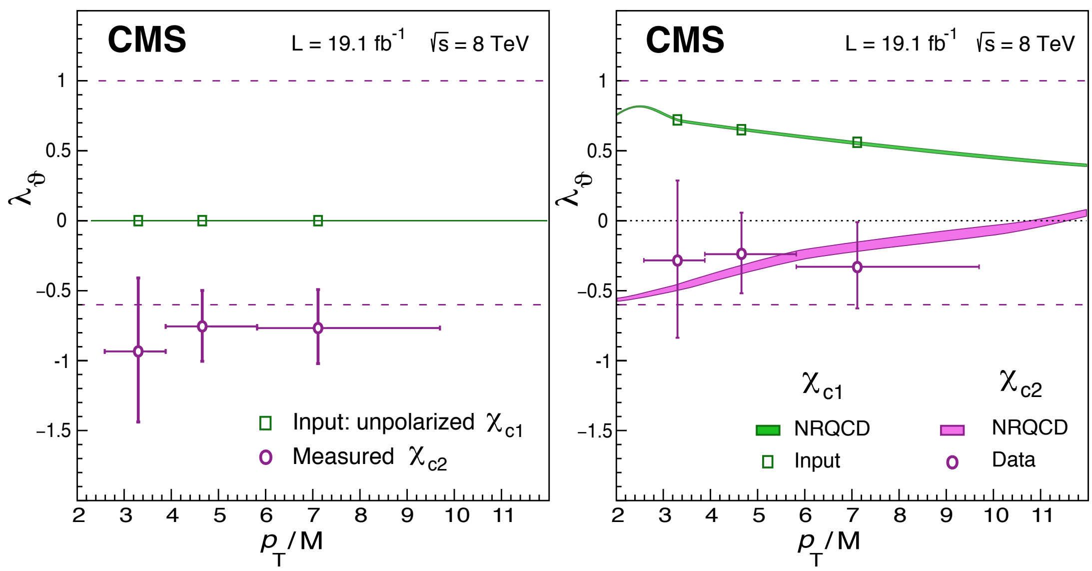

Figure 2.16: Resulting $\lambda_\vartheta^{\chi_{c2}}$ values (circles) when the $\lambda_\vartheta^{\chi_{c1}}$ values (squares) are fixed to the unpolarized (left) or the NRQCD (right) scenarios (green curves), as a function of J/ψ p_T $/M$. The purple band on the right is the NRQCD prediction for $\lambda_\vartheta^{\chi_{c2}}$ [33]. The dashed horizontal lines show the physically allowed range of $\lambda_\vartheta^{\chi_{c2}}$ [111].

larized contributions to quarkonium production, observed only in the limited kinematic domain that has been probed, or rather an exact degeneracy unpredicted by theory.

Another result obtained from theory considerations is discussed in Ref. [118]: at NLO, the shape of the ${}^1S_0^{[8]}$ SDC is indistinguishable from a linear combination of the other octet contributions to the $\psi(nS)$ states, ${}^3S_1^{[8]} + \kappa\,{}^3P_J^{[8]}$, when the parameter κ is between 1.8 and 1.85, and both are very close to the cross section data shape. Under these conditions, the cross section cannot be fitted with three degrees of freedom, so that the polarization is needed to determine all the LDMEs, as there is no such degeneracy for this observable at low p_{T} ($p_{\mathrm{T}}\,/M < 10$).

The low-p_{T}/M unpolarized data, however, is at odds with the ${}^3S_1^{[8]} + \kappa\,{}^3P_J^{[8]}$ term. As shown in Fig. 2.17, which compares λ_ϑ of ${}^1S_0^{[8]}$, ${}^3S_1^{[8]}$ and several combinations ${}^3S_1^{[8]} + \kappa\,{}^3P_J^{[8]}$, the latter term has non-zero p_{T}-dependent λ_ϑ at low p_{T}/M, for any value of κ.

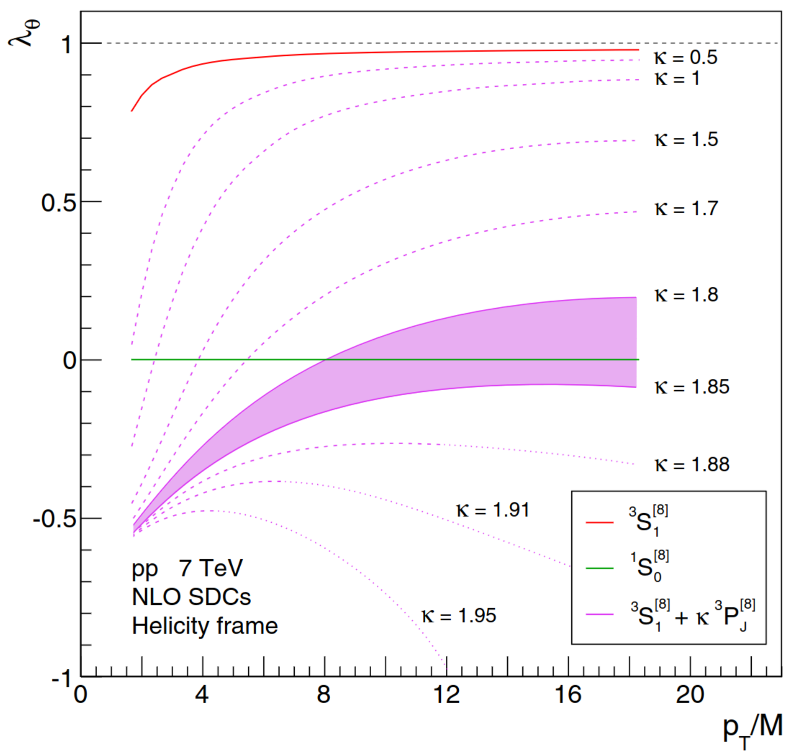

Figure 2.17: λ_ϑ for the three contributions to S-wave quarkonium production in NLO NRQCD, as functions of p_{T}/M: ${}^1S_0^{[8]}$ (green), ${}^3S_1^{[8]}$ (red) and ${}^3S_1^{[8]} + \kappa\,{}^3P_J^{[8]}$ (pink) for several values of κ. The band represents the range $\kappa = 1.8$–1.85 [118].

Current experimental results, while clearly rejecting a scenario with large λ_ϑ, are not yet precise enough to impose the stronger constraint of vanishing and p_{T}-independent polarization. If a measurement of enough precision confirms this scenario, only verified by the ${}^1S_0^{[8]}$ term, this will be a clear divergence from the principles of the NRQCD factorization approach. This discrepancy can possibly be reconciled by changes in the octet terms at higher orders, but will always lead to one of two conclusions: either the ${}^3S_1^{[8]} + \kappa\,{}^3P_J^{[8]}$ term remains incompatible with p_{T}-independent $\lambda_\vartheta = 0$, and thus its contribution is null and quarkonium production is driven entirely by the ${}^1S_0^{[8]}$ term, violating the v-scaling rules, or improved calculations will lead to $\lambda_\vartheta({}^3S_1^{[8]} + \kappa\,{}^3P_J^{[8]}) = 0$, in which case both this and the ${}^1S_0^{[8]}$ term can contribute with equal weights, but they are identical in terms of observable kinematic properties, and thus fully degenerate, pointing to a more natural formulation of the factorization expansion with fewer degrees of freedom, at least in the kinematic regions probed.

2.6 Summary

Quarkonium production, falling under the study of QCD, is an inherently complex field. The dominant theoretical approach to quarkonium production is NRQCD factorization [15], which is in good agreement with the experimental measurements of quarkonium production cross sections, but which shows some tension when it comes to polarization measurements.

The abundance of quarkonium measurements at the LHC, for multiple states, at various collision energies and in different kinematic regions, includes multiple polarization measurements [37, 38, 39, 96, 97, 36, 98], which reflect a scenario of unpolarized production for all S-wave states that remains incompatible with theory predictions of strongly transverse polarizations [62, 63, 65, 112], in what is known as the "quarkonium polarization puzzle".

Phenomenological studies have established that the polarization puzzle is dispelled by a careful treatment of the fit conditions [31]. They further establish that the data shows a universal pattern of production, at odds with the inherent complexity of the NRQCD framework [32]. Surprisingly, the theory is fully compatible with the comparatively simpler data results, through a series of precise cancellations [33].

Specific observables can be used to further probe the validity of NRQCD, such as the $\chi_{c1,2}$ polarization, determined to be significantly non-zero under NRQCD [33]. This prediction was confirmed by a measurement of the $\chi_{c1,2}$ polarization difference by CMS [111], breaking for the first time the panorama of universally unpolarized quarkonium production and validating the theory.

A data-driven analysis of the charmonium sector uncovers a prediction of $\lambda_\vartheta^\psi = 0.04 \pm 0.06$ for direct ψ production, with no p_T dependence [117], while a degeneracy in the theory SDCs imposes either a new hierarchy of $Q\overline{Q}$ contributions or a collapse of all contributions into a single one, if such a scenario of vanishing p_T-independent polarization is confirmed [118]. Current measurements are not precise enough to distinguish between the $\lambda_\vartheta = 0$ case and the alternative of weakly polarized, weakly p_T-dependent production.

The polarization dimension plays an essential role in determining the hierarchy of contributions to the production of quarkonium states, and can even be a direct probe of the validity of the theory, but the existing measurements have a limited impact, given their large uncertainties and small p_T coverage, restricted to the low p_T region. A new measurement of prompt $\psi(nS)$ polarizations, with a much larger event sample and covering a wider range in p_T, can provide the sensitivity needed to distinguish between the two polarization scenarios currently considered, and either strongly challenge NRQCD or finally disprove the hypothesis of production by a single unpolarized term, providing a clear evaluation of the relative proportions of the three colour-octet channels expected to contribute to $\psi(nS)$ production. Such a measurement is provided in this PhD thesis.

In the case of the NP polarization, a measurement in the LHC conditions would be the first of its kind since the CDF results of 2000 [21]. The size of the collected event samples should provide a statistical reach sufficient to distinguish between two main possible production topologies, each with different compositions in terms of singlet and octet contributions [55], providing an independent probe of the charmonium formation mechanism. Such a measurement is also reported in this PhD thesis.

Chapter 3

Experimental setup

The analysis described in this thesis uses data collected in pp collisions at the CMS detector in the years 2017 and 2018, and is based on $\psi(nS)$ decays to the $\mu\mu$ final state. As such, it's necessary to introduce the experimental setup used, with a brief description of the LHC and a more detailed discussion of the CMS experiment, focusing on the parts of the detector, the triggering and data storage system, and the offline reconstruction elements that are relevant to the analysis. A more detailed description of the LHC and CMS can be found in Refs. [119] and [120, 121, 122], respectively.

3.1 The Large Hadron Collider

The LHC is a superconducting hadron accelerator and collider built at CERN, operating at collision energies and rates far beyond those of previous hadron colliders. The main motivation for its development was the clarification of the nature of electroweak symmetry breaking, for which the Higgs mechanism was presumed to be responsible. This purpose was achieved in July 2012 with the announcement of the discovery of a Higgs-like boson by CMS and ATLAS [8, 9], with all subsequent studies of the properties of the boson showing compatibility with the SM Higgs boson.

The LHC is installed in a 26.7 km circular tunnel, previously constructed for the Large Electron-Positron Collider (LEP), at a depth ranging from 45 to 170 m below the surface. As a particle-particle collider, the LHC has two rings with counter-rotating beams that can achieve CM energies of up to $\sqrt{s} = 13.6$ TeV for proton-proton (pp) collisions. The machine is also capable of accelerating heavy ions, primarily lead, obtaining data for proton-lead, lead-lead and other collision systems. As the data used in this thesis is exclusively from pp collisions, the discussion will be limited to this case.

The LHC is supplied with protons from an injector chain, as seen in Fig. 3.1. The chain begins with the Linear Accelerator 2 (LINAC 2), which is the source of the protons, followed by the Proton Synchrotron Booster (PSB) and the Proton Synchrotron (PS), and finally the Super Proton Synchrotron (SPS), which feeds the protons to the LHC rings, at an energy of 450 GeV. The total filling time, from pre-acceleration to injection, is around 4 minutes per beam. The protons are not accelerated as a continuous source, but rather in "bunches" of protons. The LHC nominal performance values are of 1.15×10^{11} protons per

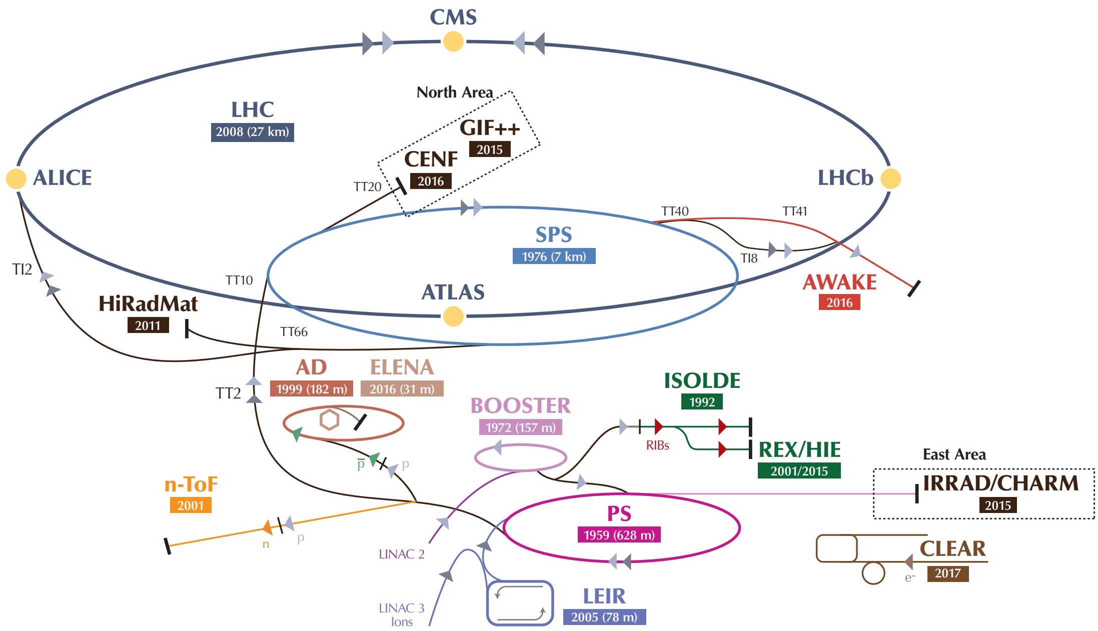

Figure 3.1: Overview of the CERN accelerator complex. Adapted from Ref. [123].

bunch, with 2808 bunches per beam and a bunch spacing of approximately 25 ns [119].

In the LHC, the protons are further accelerated using a 400 MHz superconducting cavity system, up to the desired collision energy. The beams are guided along the ring by superconducting electromagnets. Over 1000 dipole magnets are used to bend the beams, and nearly 400 quadrupole magnets to focus them. Accelerating each beam to the nominal design value of 7 TeV, for a collision energy of 14 TeV, takes approximately 20 minutes. Once this is achieved, the beams are brought to collision in the centre of the LHC experiments. This "collision mode" can be maintained for several hours, until the beam intensity decreases below a certain threshold. At this point, the full cycle restarts and a new "LHC fill" is injected [119].

The beam energy achieved at the LHC is limited by the strength of the dipole magnets, with a maximum value of 7 TeV per beam for a peak dipole field of 8.33 T. In Run 1, from 2010 to 2012, data was taken for beam energies of 3.5 and 4 TeV. In Run 2, from 2015 to 2018, this energy was increased to 6.5 TeV.

The LHC has four main collision points, located at the main experiments, also shown in Fig. 3.1:

- A Large Ion Collider Experiment (ALICE) [124], specialized in heavy-ion collisions;
- A Toroidal LHC Apparatus (ATLAS) [125], a general purpose detector and the largest of the four experiments;
- Compact Muon Solenoid (CMS) [122], another general purpose detector which will be described in more detail in Section 3.2;
- Large Hadron Collider beauty (LHCb) [126], mostly devoted to flavour physics measurements.

The expected number of events per second produced at the LHC, for a given process of cross section σ, is given by:

$$N = \mathcal{L} \cdot \sigma, \tag{3.1}$$

where $\mathcal{L}$ is the instantaneous luminosity, which depends on the beam parameters:

$$\mathcal{L} = \frac{N_b^2 n_b f_{rev} \gamma_r}{4\pi \varepsilon_n \beta^*} F. \tag{3.2}$$

with N_b the number of protons per bunch, n_b the number of bunches per beam, f_{rev} the revolution frequency, γ_r the relativistic gamma factor, ε_n the normalized transverse beam emittance, β^* the beta function at the collision point and F the geometric luminosity reduction factor due to the crossing angle at the interaction point [119]. The nominal instantaneous luminosity of the LHC design was $\mathcal{L} = 10^{34}$ cm^{-2}s^{-1}[1], but this value was exceeded during Run 2, and more than doubled by the end of 2018 [127].

The general-purpose detectors, ATLAS and CMS, are designed to be able to process at the LHC nominal design luminosity, while LHCb and ALICE are limited to lower values. The event rate at ALICE is limited by the relatively long readout time of their TPC (time projection chamber) tracking detector, while for LHCb, the limitation is due to their requirement of a negligible probability of a phenomenon called "pile-up" (PU): the occurrence of multiple pp collisions per "bunch crossing".

The total amount of collisions delivered by the LHC in a certain period of time Δt can be estimated as

$$\mathcal{L}_{int} = \int_{\Delta} \mathcal{L}(t) dt. \tag{3.3}$$

where $\mathcal{L}_{int}$ is called the "integrated luminosity". It is usually given in units of b^{-1}, or "inverse barn", and at the LHC the units pb^{-1} ($= 10^{12}$ b^{-1}) and fb^{-1} ($= 10^{15}$ b^{-1}) are more generally used. Over the course of Run 2, the LHC has delivered an integrated luminosity of 163.55 fb^{-1} to the CMS interaction point, of which CMS has recorded 150.78 fb^{-1} [127]. Figures 3.2 and 3.3 show the peak instantaneous luminosity and the integrated luminosity, respectively, recorded by CMS over Run 2.

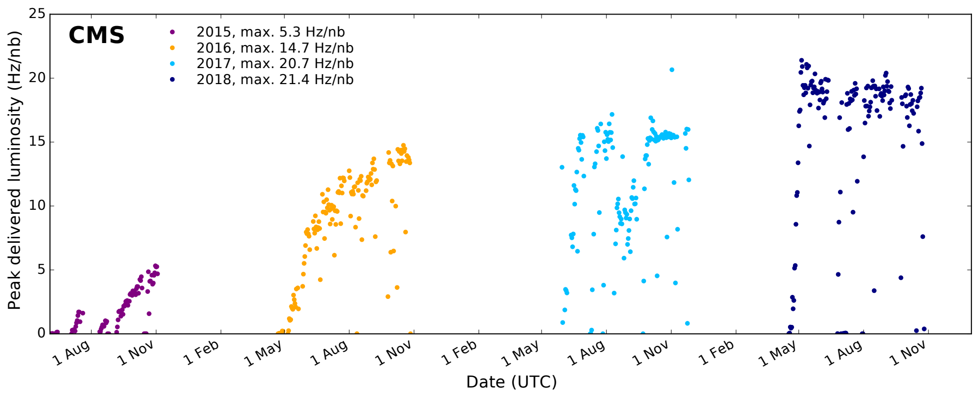

Figure 3.2: Peak instantaneous luminosity delivered to CMS in pp collisions vs. time, over the four years of Run 2 [127].

[1] $\mathcal{L}$ can also be written in units of Hz/b, with 1 b$= 10^{-24}$ cm^2.

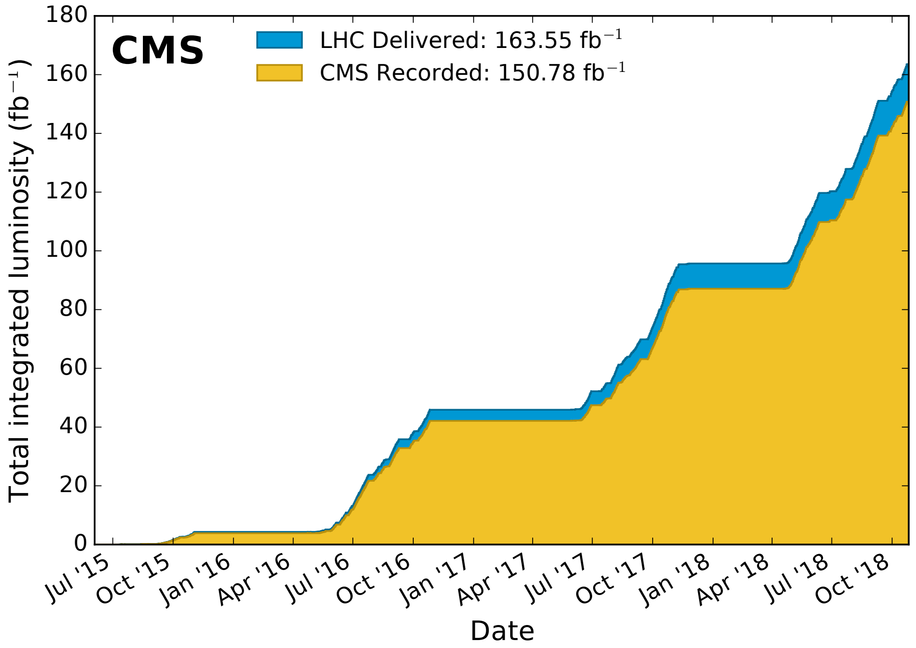

Figure 3.3: Cumulative delivered and recorded luminosity at CMS in pp collisions vs. time, over the four years of Run 2 [127].

3.2 The Compact Muon Solenoid experiment

The Compact Muon Solenoid (CMS) experiment is a general-purpose particle detector designed to cover a wide range of physics topics. It is located in Cessy, France, and built around the so-called "Point 5", one of the four interaction points of the LHC.

The CMS experiment was designed around the goals of the LHC physics programme and the associated detector requirements. Muon tracks are important and unique in the context of hadron collider physics, imposing a requirement of good muon identification and momentum resolution and good dimuon mass resolution, achieved by a dedicated muon detector. The reconstruction of charged particles requires good momentum resolution and reconstruction efficiency in the inner tracker, close to the interaction region, particularly the efficient identification of τ leptons and b-jets. The electromagnetic calorimeter (ECAL) must have good energy resolution, particularly the diphoton and dielectron mass resolution, a wide geometric coverage, and efficient isolation of photons and leptons at high luminosities. Finally, the hadron calorimeter (HCAL) is designed to measure missing transverse energy and requires a large geometrical coverage with good angular resolution [122].

The overall CMS apparatus dimensions are a length of 21.6 m and a diameter of 14.6 m, with a total weight of 12500 t. The layout of the CMS detector is cylindrically symmetric along the beam line, with the "barrel" at mid-rapidity being closed by the two "endcaps" at either end of the detector, and follows an onion-like structure of several concentric layers of complementary sub-detectors, as shown in Fig. 3.4. The solenoid magnet that gives CMS its name encloses the innermost detectors, providing a magnetic field of 3.8 T, and is in turn surrounded by a steel return yoke that forms the bulk of the detector's mass, interleaved with the muon detection stations [122].

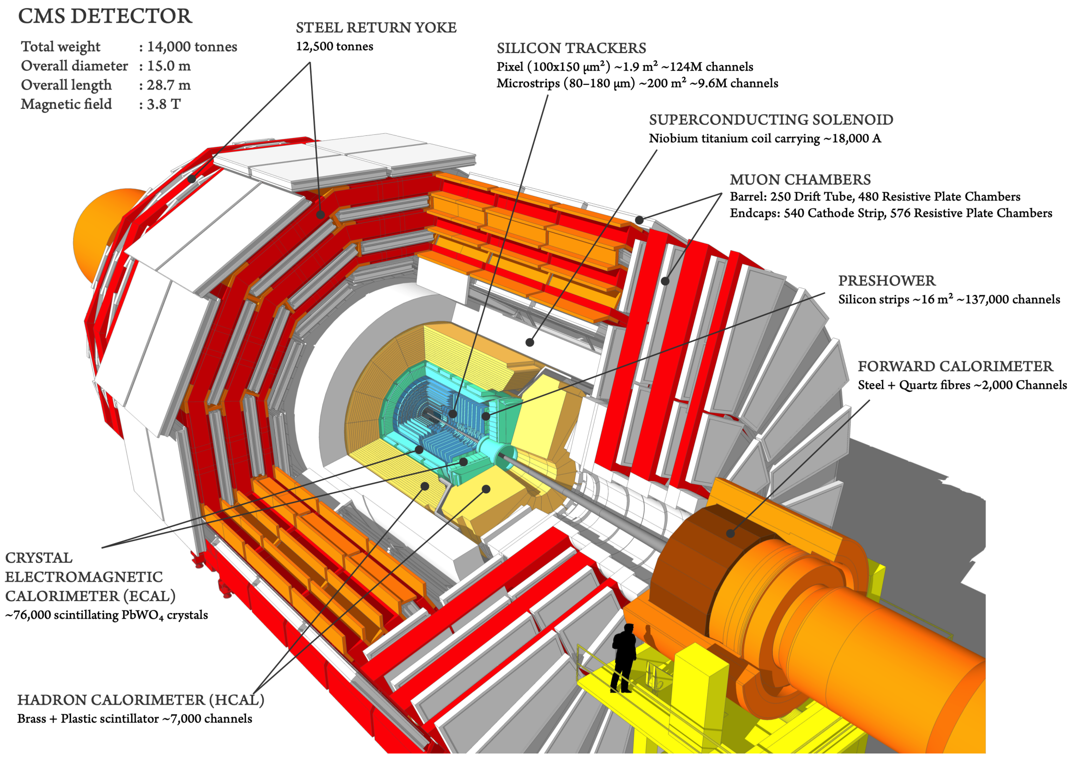

Figure 3.4: Cutaway view of the CMS detector, with all components labelled [128, 129].

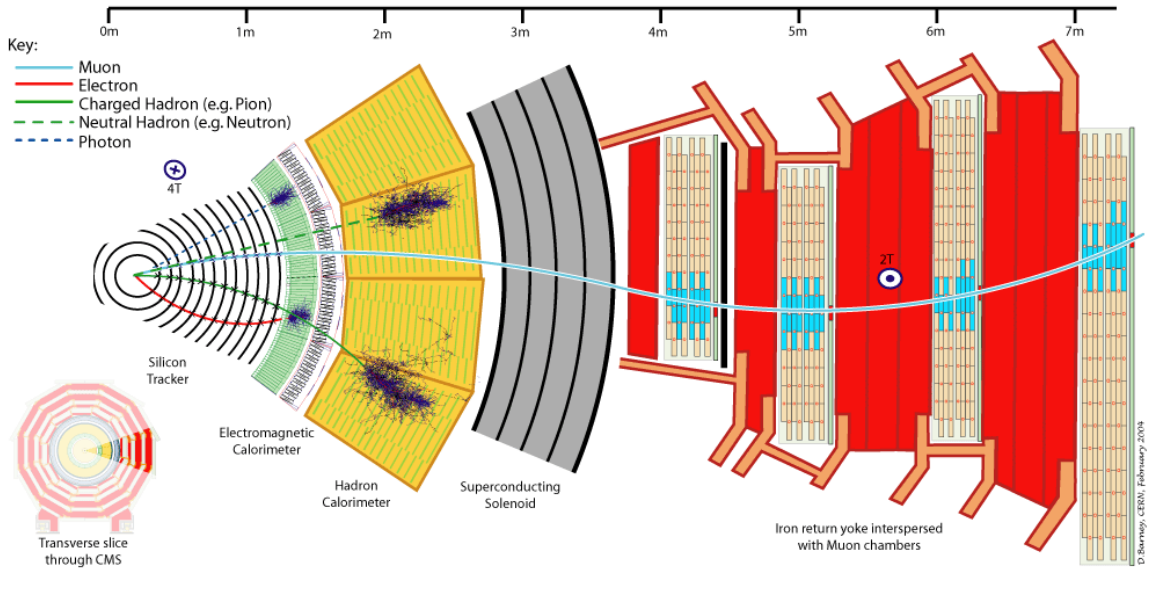

Figure 3.5: Transverse slice through CMS, illustrating the trajectory of different types of particles [130].

Figure 3.5 shows a transverse slice through the barrel of the detector, illustrating the interactions of different types of particles passing through CMS. The silicon pixel and strip trackers measure the positions and momenta of charged particles, reconstructing their tracks. Next is the ECAL, measuring the energy deposited by particles like photons and electrons, followed by the HCAL, where hadrons deposit their energy, allowing for the reconstruction of jets and missing transverse energy. The solenoid encasing these systems generates a magnetic field that bends the trajectories of charged particles, an essential element to determine their charge and momenta. Finally, the muon chambers beyond the magnet identify and reconstruct the muons [122].

Before moving on to a more detailed description of the sub-detectors relevant to the analysis described in this thesis, it is important to introduce some conventions and the coordinate system used in the experiment.

An "event" is defined as the complete information on all collisions that take place during one bunch crossing. A physics analysis will define, for each event, a "primary vertex" (PV), consisting of the point of collision of two protons most likely to have produced the interaction under study. The PVs are located inside the "beam spot" (BS), a region that approximates the overlap region of the two proton bunches. There can also be "secondary vertices" (SV), for long-lived particles produced in a PV that travel a certain distance before decaying. This is the case for b-hadrons that decay into non-prompt charmonia, as mentioned in Chapter 2.

The coordinate system of CMS is centred around the nominal "interaction point" (IP) inside the experiment, with the z-axis pointing along the counter-clockwise beam direction. The x-axis points radially inward towards the centre of the LHC ring, and the y-axis points vertically upwards. The spherical coordinate system is also commonly used: the polar angle θ is measured with respect to the z-axis and the azimuthal angle ϕ is measured from the x-axis in the xy plane. In this way, the energy and momentum transverse to the beam line, E_{T} and p_{T}, respectively, are computed from the x and y components. Rather than the polar angle, it is more common to use the pseudo-rapidity η, defined as [122]

$$\eta = -\ln\tan(\theta/2). \tag{3.4}$$

For highly energetic particles ($E \gg m$), this quantity is a good approximation of the rapidity y, defined in Eq. 2.5.

3.2.1 Tracking detectors

The silicon tracking system is closest to the beam line, surrounding the IP, with a length of 5.8 m and a diameter of 2.5 m. It precisely and efficiently measures the trajectories of charged particles emerging from the LHC collisions and allows for a precise reconstruction of SVs. The magnetic field generated by the solenoid is homogeneous over the full volume of the tracker, so that the particle momentum can be determined with high precision from the curvature of the track.

At the LHC nominal luminosity, there are around 1000 particles crossing the tracker for each bunch crossing, with an interval of 25 ns between bunches, making it necessary that the tracker has high granularity and fast response. There is also significant radiation damage from the high particle flux, adding the requirement of a radiation-resistant tracker. Finally, it is desirable to minimize the material budget in order to limit unwanted interactions as the particles traverse the detector. These requirements lead to the choice of silicon detectors for CMS's tracking system. This system detects charged particles through "hits": when a particle traverses the tracker, it interacts electromagnetically with the silicon, producing small electrical signals that are collected and amplified. The individual hits are then joined together to form tracks.

The CMS tracking system is composed of a pixel detector followed by a strip tracker, installed in layers along the barrel and completed with disks in the endcaps for an acceptance up to $|\eta| = 2.5$. The layout of the inner tracking system is shown in Fig. 3.6. In total, the CMS tracker is composed of 1856 pixel and 15148 strip detector modules, and it ensures efficient tracking for transverse momenta above 1 GeV [122, 131].

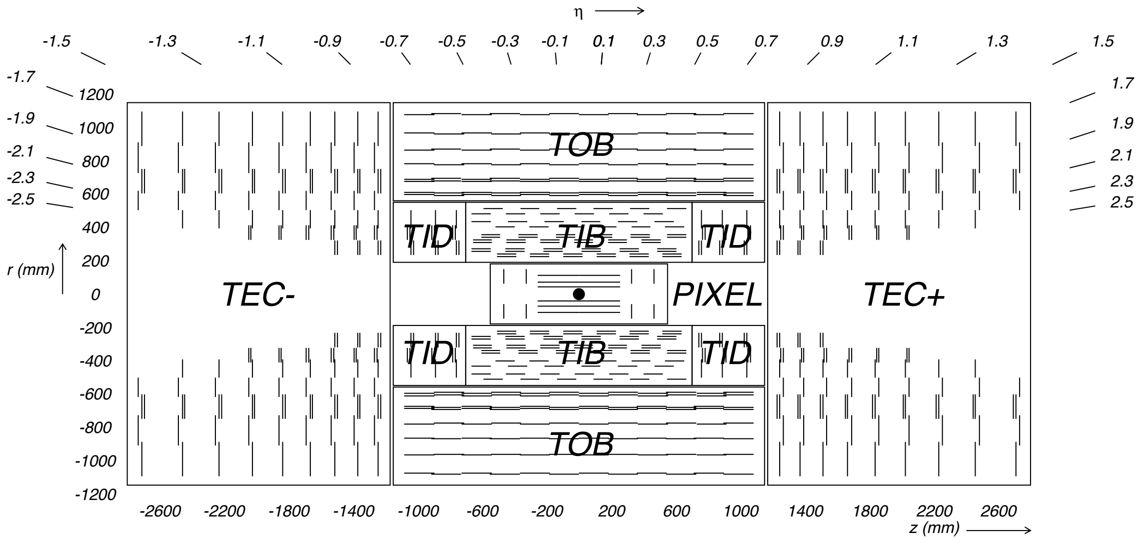

Figure 3.6: Layout of the inner tracking system, before the Phase 1 pixel detector upgrade. Each line represents a detector module. Double lines represent back-to-back modules, as described in the text [122].

Silicon pixel detector

The pixel system is the innermost part of the tracking system and provides precise tracking points in $r - \phi$ and z, with a pixel cell size of 100×150 μm^2, allowing for a 3D vertex reconstruction in space with similar track resolution in both directions. It originally consisted of three barrel layers (BPix) at radii of 44, 73 and 102 mm and two endcap disks at each end (FPix), at distances of 345 and 465 mm from the IP [122].

The installation of the CMS Phase-1 pixel detector, which took place during the LHC technical stop from December 2016 to April 2017, optimized this layout, taking advantage of the installation of a new beam pipe with a smaller radius. This upgrade was motivated by the instantaneous luminosity achieved for Run 2, which exceeded the nominal value by a factor of two, also doubling the average PU. The original tracker system was not designed for these values and it was necessary to replace it with one with improved performance at higher rates, improved radiation tolerance, and more robust tracking. The upgraded pixel detector has four concentric barrel layers at radii of 29, 68, 109 and 160 mm, with a length of 540 mm, and three disks at the endcaps, at distances of 291, 396 and 516 mm from the centre of the detector, with a radial coverage of 45–161 mm [131].

The layout of the upgraded pixel detector is compared with the original in Fig. 3.7. The arrangement of barrel layers and forward pixel disks on each side ensures that there are 4 tracking points over the full $|\eta| < 2.5$ range.

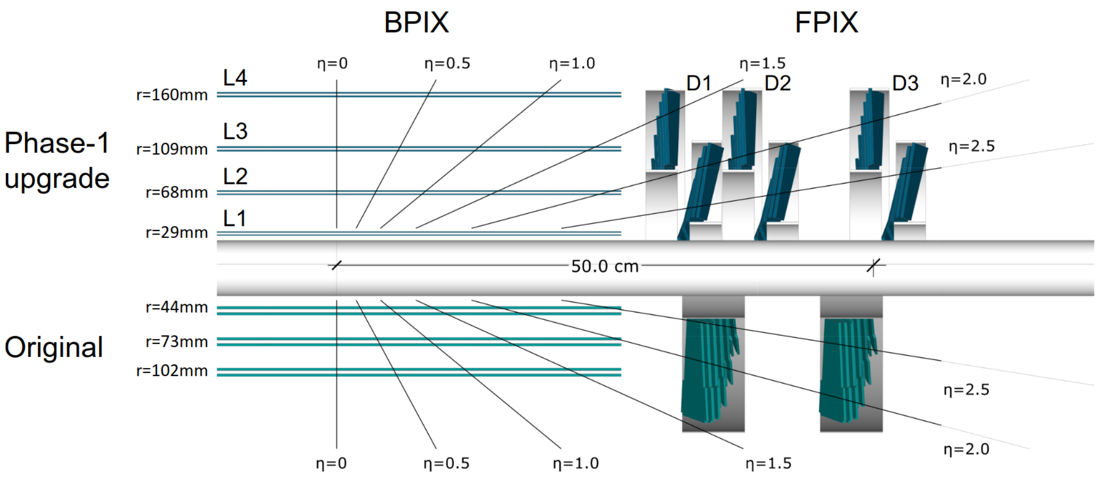

Figure 3.7: Comparison between the layouts of the CMS Phase-1 pixel detector and the original detector, in the longitudinal view [131].

Silicon strip tracker

Around the pixel detector, at larger radii, the reduced particle flux allows the use of less granular silicon strip detectors. The geometrical layout of the strip detector is shown in Fig. 3.6. The Tracker Inner Barrel and Disks (TIB/TID) compose the innermost layer of the strip tracker, covering the intermediate radii, $20 < r < 55$ cm. This region has typical strip sizes of 10 cm$\times$80 μm. The TIB is composed of 4 barrel layers and the TID of 3 disks at each end. Surrounding it is the Tracker Outer Barrel (TOB), covering the region up to $r = 116$ cm. The TOB consists of 6 barrel layers, covering the $|z| < 118$ cm region. Beyond this z range are the Tracker EndCaps (TEC+ and TEC-), which cover the region $124 < |z| < 282$ cm and $22.5 < r < 113.5$ cm and are composed of 9 disks each. In this outer region, cell sizes can go up to about 25 cm$\times$180 μm.

In some of the layers, both in the barrel and in the disks, a second micro-strip detector module is added, mounted back-to-back to the main module, with a stereo angle of 100 mrad in order to provide a measurement of the second coordinate (measuring z in the barrel and r on the disks). The tracker layout ensures at least 9 hits in the silicon strip tracker over the range $|\eta| < 2.4$, with at least 4 being in back-to-back modules [122].

3.2.2 Muon detectors

The muon detectors play an essential role in the analysis described in this thesis, which relies on the efficient and accurate reconstruction of the dimuon final state. More generally, the muon detectors are essential for most of the experimental signatures studied by CMS, and so special attention was devoted to their development, as suggested by their presence in the experiment's name. The muon system has three functions: identifying muons, measuring their momentum, and triggering on them. As shown in Fig. 3.4, the muon systems are the outermost detectors, surrounding the superconducting solenoid and integrated in the return yoke structure. The high magnetic field ensures good muon momentum resolution and triggering, while the layers of detectors between the IP and the muon stations, as well as the return yoke, ensure that most particles are absorbed before reaching the stations, especially hadrons.

As was described for the silicon trackers, the muon system is composed of a cylindrical, barrel section and two planar endcap regions, following the geometry of the detector. It is integrated in the return yoke, which is composed of 5 wheels in the barrel region and 3 disks in each endcap. The muon system consists of about 25000 m^2 of detection planes, composed of three types of gaseous particle detectors, which are reliable and cost-effective [122].

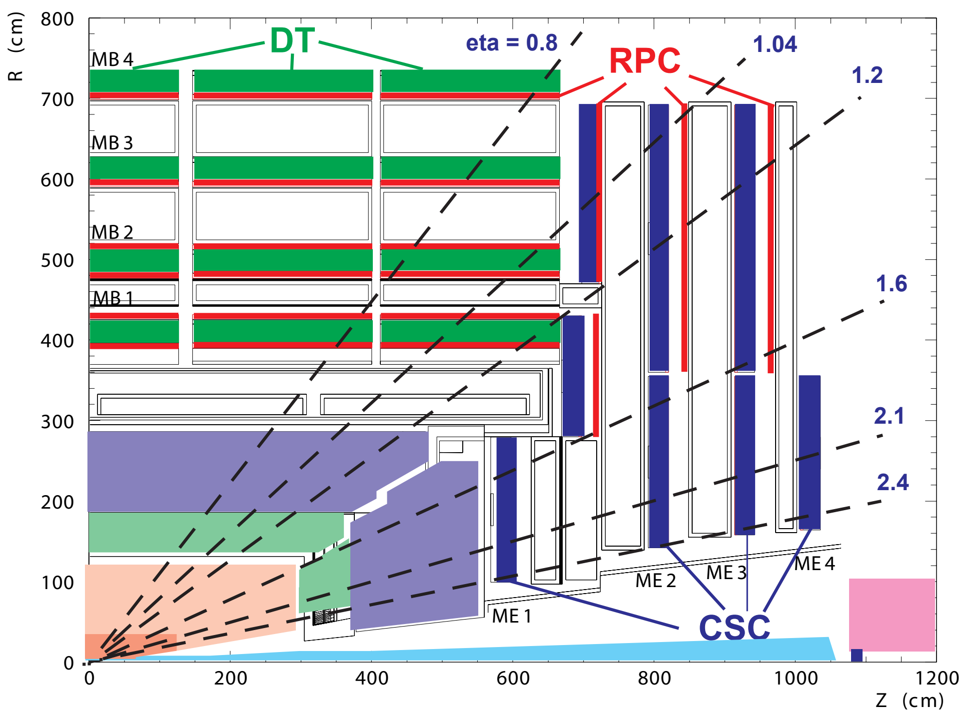

Figure 3.8: Layout of one quarter of the CMS muon system [120].

The geometric layout of the detectors in the muon system is shown in Fig. 3.8. In the barrel region, characterized by low background and muon rates, and a uniform magnetic field, muons are detected by aluminium drift tubes (DT). The chambers cover the pseudorapidity region $|\eta| < 1.2$ in 4 stations (MB1-MB4) interspersed among the layers of the flux return plates. The first 3 stations contain 8 chambers, in 2 groups of 4, measuring the muon coordinate in the $r - \phi$ plane, in addition to 4 chambers measuring in the z direction. The fourth and outermost station only measures in the $r - \phi$ plane, with 8 chambers. The drift cells in each chamber are offset by the width of a half-cell with respect to their neighbours, to eliminate dead spots [122].

In the endcap regions, with higher rates and a non-uniform magnetic field, cathode strip chambers (CSC) are used, covering the range $0.9 < |\eta| < 2.4$. There are also 4 CSC stations (ME1-ME4), with chambers perpendicular to the beam line, in between the flux return plates. The cathode strips of each chamber provide a precision measurement in the $r - \phi$ plane [122].

Complementing these detectors is a dedicated trigger system consisting of resistive plate chambers (RPC), present both in the barrel and endcap regions. The RPCs have coarser spatial resolution than the DTs and CSCs, but they have a fast response and good time resolution, helping to identify the correct bunch crossing, ensuring good operation at high rates. There are 6 layers of RPCs in the barrel, 2 in each of the first two stations and 1 in each of the last two. In the endcap region, there are 3 layers of RPC, one in each of the first three stations [122].

Drift Tube Chambers

The DT chambers are filled with a mixture of 85% argon and 15% CO_2. A muon entering the chamber causes gas molecules to ionize along its path and the resulting ions and electrons, oppositely charged, drift to the respective electrodes. With the known drift time, precisely determined with the help of the RPCs, and the known drift-velocity of the material, the muon trajectory through the DT can be reconstructed with a spatial resolution of around 100 μm in position and 1 mrad in angle [120, 122].

Cathode Strip Chambers

The CSCs are multiwire proportional chambers made of 7 trapezoidal cathode panels. The panels encase 6 gas layers, composed of 40% argon, 50% CO_2 and 10% CF_4, with anode wire planes. If a charged particle traverses the CSC, the gas molecules in each plane of the chamber are ionized, inducing an electron avalanche that produces a charge on the strips. The spatial resolution for the CSCs is around 100 μm in position and 10 mrad in angle [120, 122].

Resistive Plate Chambers

RPCs are gaseous parallel-plate detectors, filled with a mixture of 96.2% $C_2H_2F_4$, 3.5% iC_4H_{10} and 0.3% SF_6, with spatial resolution of the order of 1 cm and providing a much better time resolution than the DTs and CSCs. Operated in avalanche mode, their time resolution is of the order of 1 ns [120, 122].

3.2.3 Trigger and Data Acquisition Systems

At the nominal design parameters of the LHC, proton-proton collisions occur every 25 ns, corresponding to a bunch crossing frequency of 40 MHz. At the nominal design luminosity of 10^{34} cm^{-2}s^{-1}, the PU is approximately 20, taking even larger values at the increased instantaneous luminosity achieved in Run 2. This results in a significantly larger amount of data than what can be stored and processed, making it necessary to achieve a drastic reduction in rate. This task is performed by the trigger system, considered the start of the physics event selection process. The trigger reduces the rate of events by selecting the “interesting” events, rejecting those that don’t fit its requirements. This is achieved, in a first step, by a hardware-based “level 1 trigger” (L1) and, subsequently, by a software-based “high level trigger" (HLT). A combined rate reduction factor of about 10^5 is achieved, limiting the output rate to the order of 1 kHz. This limit has been steadily increasing, from 100 Hz in Run 1, and is determined by the computing resources involved in the offline reconstruction. The accepted events are then forwarded to mass storage devices and their content is reconstructed to identify high-level analysis objects, to later be accessed to perform physics data analysis [122, 132].

Level 1 Trigger

As the first step in the trigger system, the L1 trigger must reduce the output rate to less than 100 kHz. Data from a particular beam crossing is held in buffers while trigger data is collected and the decision to store or discard events is reached. The time allocated for this is 3.2 μs, of which the trigger calculations account for less than 1 μs. The time constraint limits the information that can be used at L1, excluding information from the silicon tracker, and also limits trigger calculations and resolution. For example, for muon objects, pattern recognition algorithms are applied to track segments from the DT and CSC systems or to hits from the RPCs, with muon candidates being assigned p_{T} and (η, ϕ) values with limited granularity. If the L1 decision is positive, a full-detector readout is triggered and the event is further processed by the HLT [122, 133].

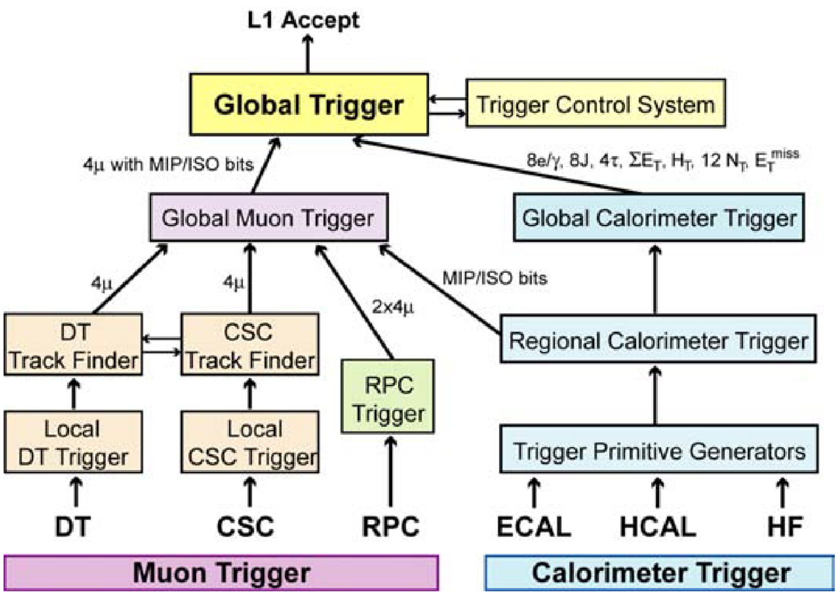

Figure 3.9: Layout of the L1 trigger at CMS [122]

The L1 trigger consists of custom hardware processors, involving the calorimeters and muon systems as well as some correlated information. Figure 3.9 shows a diagram of the L1 layout, with all its major subcomponents. These are divided into local, regional and global components. The local triggers, also called trigger primitive generators, are based on energy deposits in calorimeters and hits in the muon detectors. Regional triggers combine the trigger primitive information in limited spatial regions to determine trigger objects such as electron or muon candidates. The global calorimeter and muon triggers combine the information of the full respective subsystem and transfer it to the global trigger, the highest-level entity of the L1 hierarchy. It is this final entity that makes the decision to reject a given event or accept it for further evaluation by the HLT [122].

The requirements for approval or rejection of an event are defined by the L1 triggers, also called “L1 seeds”. Each of these requires certain physics objects, subjected to certain cuts. These seeds are grouped together into an L1 menu, which evolves over time according to experimental needs, always respecting the imposition that the rate of accepted events for the full L1 menu must be below the limit of 100 kHz. Rates for individual seeds can be reduced either by tightening the requirements on the physics objects (for example, increasing a p_{T} cut) or by prescaling by a factor of n_{PS}, which means that only every n_{PS}^{th} event passing that trigger's cuts is forwarded to the HLT. An L1 menu is typically composed of around 100 different seeds, whose rates partially overlap as an event can satisfy the conditions of multiple seeds. In this way, the menu rate is lower than the sum of individual rates [133].

The L1 trigger was updated in the Long Shutdown 1 (LS1), which took place in 2013–14, between Runs 1 and 2. The expected increase in luminosity and PU for Run 2 led to a projected increase in trigger rates of around a factor of 6. In order to avoid a straightforward increase in thresholds and prescaling to limit this rate increase, which would have a negative impact on the physics performance of CMS, several new features were introduced to improve performance instead, focusing on PU subtraction and improved object isolation and jet finding. The L1 menu was further updated to allow a greater number of triggers and include more sophisticated relations involving the input objects [134].

The electronics for the calorimeter, muon and global triggers were upgraded, including added interconnections between the systems. The upgraded trigger was commissioned in parallel with the Run 1 trigger, after the LHC restart in 2015, becoming available for CMS data taking in 2016.

High Level Trigger

The events that are accepted by the L1 trigger are forwarded to the HLT, which performs more complex software reconstruction algorithms on the complete read-out data, including the tracker information. It is implemented in a dedicated processor farm using commercial CPUs, regularly upgraded so that it totalled over 30 thousand cores in 2018. The calculations performed at this level are similar to those performed in offline analyses, with an added emphasis on speed of execution which results in worse resolution. The information content of the full event is stored in buffers during the processing, with some events requiring up to 1 s of processing time [122, 135, 136].

There are a few hundred HLT algorithms, or “HLT paths”, forming an HLT menu similarly to the L1 menu. This menu evolves over time, depending on the instantaneous luminosity of the LHC, so that the data rate can be kept at the allowed limit of 1 kHz. Each path starts from an L1 seed, or a selection of seeds, so that it only runs on events that triggered at least one of these seeds. Following this initial selection, the path is then composed of a sequence of reconstruction modules, the “HLT producers”, which perform the steps in the reconstruction of a physics object, and filter modules, the “HLT filters”, which reject events based on the objects reconstructed up to that point. This allows the processing time to be optimized, by first reconstructing and filtering on the simpler objects, such as those relying on information from the calorimeters and the muon detectors, and only proceeding to more complex and time-intensive reconstruction involving the tracker on the smaller sample of events that survive the prior cuts. The event is accepted if the last filter of a path is passed, at which point it is written in permanent storage for offline physics analysis [133].

The individual HLT paths are assigned to different Physics Analysis Groups (PAGs), with accepted events being stored in the corresponding primary data sets (PDs). The sum of the rates of all PDs must be within the overall HLT output rate limit, which also includes smaller data sets for calibration purposes. Each PAG is allocated a fraction of the total allowed bandwidth.

Most of the data is processed immediately after collection, and this prompt reconstruction is one of the main limitations of the HLT output rate. However, in 2012, the last year before the LS1, a special "parked" data stream was collected and stored, to be analysed only after the run was over, using the processing resources that were freed up during the shutdown [133]. This procedure was repeated for Run 2, with the implementation of a variety of specialized parking triggers running over 2016, 2017 and 2018. Over the final year, there was a main focus on B physics, storing around 10^{10} $b\bar{b}$ events [137].

3.3 Quarkonium selection and reconstruction at CMS

As mentioned in Section 2.1, the most important decay modes for S-wave quarkonium states, favoured experimentally, are the dimuon decays. These provide a simple, non-hadronic signature, which requires only the detection of muons, for which the CMS apparatus is particularly good. The analysis of S-wave quarkonia in CMS begins with the selection of events through the appropriate triggers, followed by the offline reconstruction of these events, producing the physics objects from the information delivered by the silicon tracker and muon detector systems. This process, described in a general way in this section, gives rise to quarkonium candidates, which can then be used in a physics analysis.

3.3.1 Dimuon triggers

The selection of dimuons from S-wave quarkonium decays is done through dimuon triggers, which select events with a pair of muons. Such a selection condition would vastly exceed the allocated bandwidth at the instantaneous luminosity delivered by the LHC, so these triggers, both for L1 and HLT, require additional conditions, leading to a family of dimuon triggers with different cuts on kinematic variables, quality requirements, and prescale values, each of which can be used in the study of particular states or decays.

The dimuon triggers aimed at quarkonium S-wave states in particular begin with L1 triggers using information from the muon detectors. At the beginning of Run 1, they simply required a pair of muons, but as the dimuon rate increased due to increasing instantaneous luminosity, further conditions such as a requirement of "high quality" for both muons and a maximum single muon $|\eta|$ were added to keep the L1 rate under control.

As mentioned in Section 3.2.3, the L1 trigger was updated in the LS1, allowing for more sophisticated cuts to keep the rates at acceptable values in Run 2, coping with the much larger instantaneous luminosities. The further requirement of oppositely-charged muons was added, as well as limits on the dimuon $\Delta\eta$, taking advantage of the ability to consider correlations between two trigger objects. During the extended year-end technical stop between the 2016 and 2017 data-taking periods, a final set of L1 triggers was established for quarkonium analyses in 2017 and 2018, maintaining the requirements on quality, charge and $|\eta|$, introducing cuts in single muon p_{T}, and implementing a dimuon invariant mass range or a maximum $\Delta R = \sqrt{(\Delta\eta)^2 + (\Delta\phi)^2}$, the angular distance between the two muons. The triggers were aimed at both charmonium and bottomonium, balancing p_{T} and $|\eta|$ requirements to achieve both efficiency and rates requirements [138].

The L1 algorithms related to charmonium studies used in 2017 and 2018 are:

- `L1_DoubleMu0er1p4_SQ_OS_dR_Max1p4` and `L1_DoubleMu0er1p5_SQ_OS_dR_Max1p4`: require two muons of opposite charge with $|\eta| < 1.4$ or $|\eta| < 1.5$, respectively, $\Delta R < 1.4$ and no p_{T} cut;
- `L1_DoubleMu4p5_SQ_OS_dR_Max1p2` and `L1_DoubleMu4_SQ_OS_dR_Max1p2`: require two muons of opposite charge with $p_{\mathrm{T}} > 4.5$ GeV or $p_{\mathrm{T}} > 4$ GeV, respectively, and $\Delta R < 1.2$;
- `L1_DoubleMu8_SQ`: requires two muons with $p_{\mathrm{T}} > 8$ GeV and no other cuts, so that there is no correlation between the two muons.

The label “SQ” refers to the quality requirement and “OS” to the requirement of opposite charges.

At the HLT, more complex cuts can be applied, due to the availability of information from the tracker and the more sophisticated reconstruction algorithms. As was the case for the L1, no rate-reducing requirements were needed at the beginning of Run 1, and more were added as the instantaneous luminosities increased. Most HLT dimuon triggers include the distance of closest approach between the two muons and the χ^2 probability of the dimuon vertex fit, which is a fit of the positions and momenta of the two muon candidates to a common vertex. Cuts in invariant mass and dimuon p_{T} are also used for quarkonium HLT paths, as a way to reduce the rates. The former are intended to reject non-signal events, restricting the data-taking to the regions of interest around the quarkonium masses, while the latter inevitably lead to the rejection of signal events, and are considered a necessary sacrifice given the focus of most physics analyses on high-p_{T} regions.

At the beginning of Run 2, in 2015 and 2016, the quarkonium trigger menu was mostly based on the one used at the end of Run 1, in 2012, limiting the increased rate from the higher $\sqrt{s}$ and instantaneous luminosity with simple adaptations such as increased p_{T} thresholds or prescaling. During the extended technical stop, an effort was made to review the HLT strategy, keeping the lowest possible dimuon p_{T} thresholds and reducing the rates with other types of cuts, but the nature of these triggers leaves few avenues for rate reduction, and the final selection of triggers for Run 2 combines paths of higher p_{T} thresholds with those using reduced p_{T} cuts accompanied by limitations such as restricting the data-taking to the barrel region ($|y| < 1.25$) [138].

The charmonium triggers used for the analysis described in this thesis are `HLT_Dimuon25_Jpsi` and `HLT_Dimuon18_PsiPrime`, for the J/ψ and $\psi(2\mathrm{S})$, respectively. The values after “Dimuon” indicate the dimuon p_{T} cut and the state label (“Jpsi” or “PsiPrime”) indicates the invariant mass window selected by the trigger, centred on the corresponding state’s mass. More information on the exact cuts and requirements of the triggers is given in Chapter 4.

To exemplify the manner in which quarkonium triggers target the regions of interest for quarkonium analyses, ensuring the collection of large samples of candidates for study, Fig. 3.10 shows the data collected by the CMS HLT dimuon triggers for a small fraction of the total luminosity registered in 2017, highlighting the data collected by specific triggers.

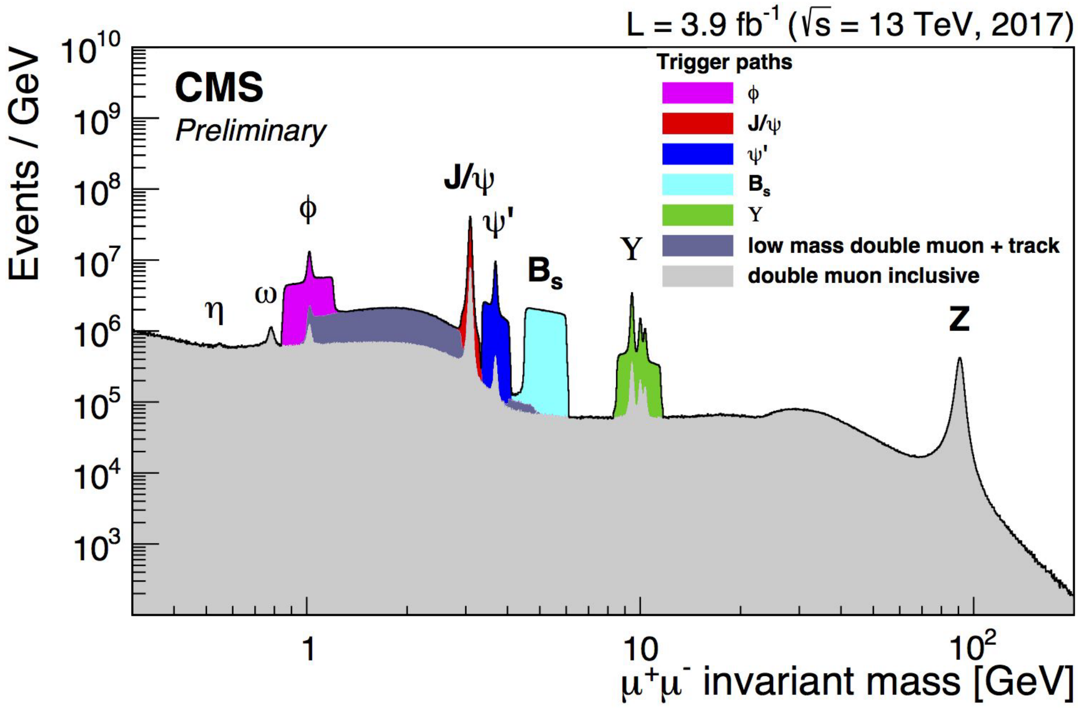

Figure 3.10: The dimuon invariant mass distribution reconstructed by the CMS HLT for a small fraction of the total luminosity registered in 2017, using the inclusive double-muon trigger (light gray) and other triggers aimed at low-mass resonances [139].

3.3.2 Muon reconstruction and identification

Muon reconstruction in CMS uses both the muon detectors and the inner tracker, achieving improved momentum resolution through this combination. This is illustrated in Fig. 3.11, comparing the momentum resolution using each system and using both.

Tracks are first reconstructed independently in each system, defining “tracker tracks” and “standalone muon tracks” for the tracker and muon detectors, respectively [139].

Tracker tracks are reconstructed through an iterative approach, beginning with the tracks that are easiest to find and, after each iteration step, removing the hits associated with the reconstructed tracks from the set of available input hits, so that the next step is run on the reduced set of inputs. In this way, the combinatorial complexity is reduced at each iteration step, simplifying subsequent searches for more difficult types of tracks [140].

Standalone muon track reconstruction begins with seeds composed of groups of DT or CSC segments, and then proceeds by gathering all information (from CSC, DT or RPC hits) along a muon trajectory, using a Kalman-filter[2] technique [139].

[2]The Kalman filter is an algorithm used in track and vertex fitting [141].

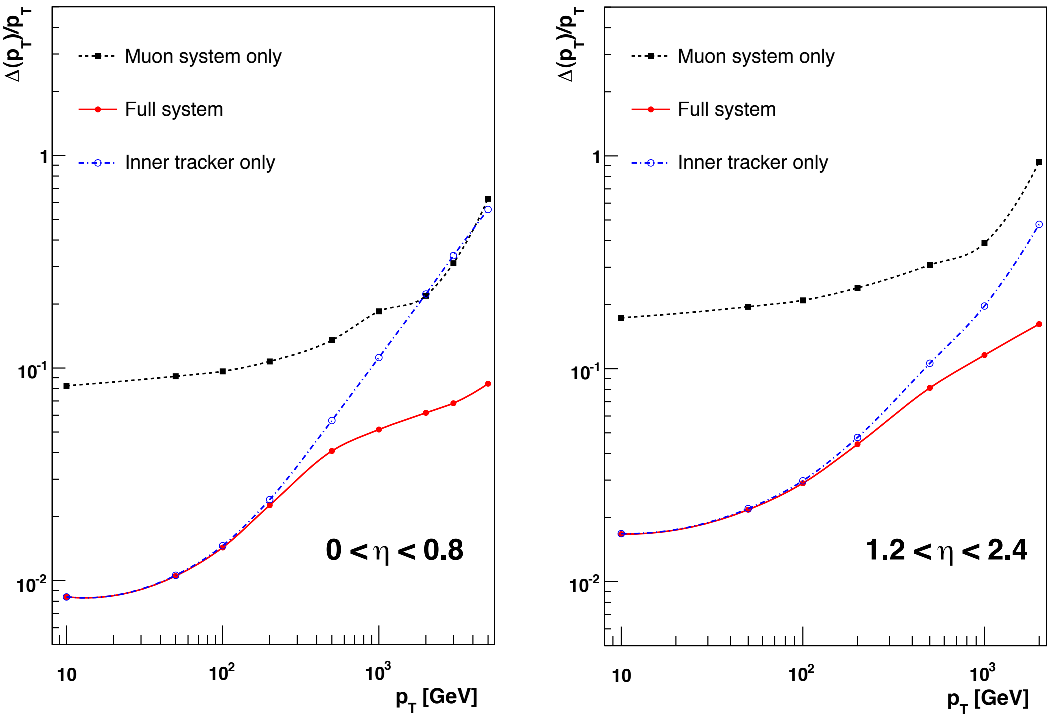

Figure 3.11: Muon transverse momentum resolution as a function of transverse momentum when using only the muon system, only the inner tracker, or both, for $|\eta| < 0.8$ (left) and $1.2 < |\eta| < 2.4$ (right) [122].

Muon reconstruction combining the two tracks is performed according to two different algorithms, resulting in either "global muons" or "tracker muons" [139]:

- Tracker muons are built from the inside out, propagating tracker tracks to the muon system if they satisfy certain kinematic properties. The tracker track is identified as a tracker muon track if at least one muon segment (straight-line tracks built within a single CSC or DT chamber) matches the extrapolated track.

- Global muons are reconstructed from the outside in, beginning with standalone muon tracks and matching them to tracker tracks. This is done by propagating both tracks to a common surface, after which a combined fit is performed with the Kalman filter, using information from both tracks.

Due to high reconstruction efficiency, about 99% of the muons produced within the geometrical acceptance of the muon system are reconstructed as either a global or a tracker muon, and often as both. If a global muon and a tracker muon share the same tracker track, they are merged into a single candidate [139].

For low-p_{T} muons, tracker muons have a higher efficiency than global muons, given that only one muon track segment is required, usually in the innermost station. On the other hand, tracker muons that are not global muons have a higher probability of muon misidentification. Global muons have a reduced misidentification rate in comparison, also showing improved p_{T} resolution for $p_{\mathrm{T}} > 200$ GeV due to their use of information from both the tracker and muon systems [139].

Given the relatively low p_{T} of the muons used in this thesis, their momentum is measured only using the silicon tracker (see Fig. 3.11) and the muon stations are only used for trigger and identification.

In order to increase the purity of the reconstructed muons, defined as the fraction of reconstructed tracks that correspond to real muons, a set of selection criteria have been established, known as "muon identification". There are several types of identification, chosen for each physics analysis depending on the desired balance between sample efficiency and purity. More information on these criteria can be found in Ref. [139].

Separation of PR and NP events

As mentioned in Chapter 2, non-prompt charmonia can be distinguished from prompt charmonia using the displacement between the production of a b-hadron in the PV and its decay into a charmonium state in a SV. The typical distance of a few 100 μm between the two vertices can be resolved by the CMS tracker, allowing for the definition of a variable to discriminate between the PR and NP charmonia, the "pseudo-proper lifetime" or simply "lifetime" [70], defined using the dimuon properties as the b-hadron is not reconstructed,

$$\ell = L_{xy} \cdot \frac{M_{\mu\mu}}{p_{\mathrm{T}}^{\mu\mu}}, \tag{3.5}$$

where L_{xy} is the most probable transverse decay length in the laboratory frame, defined as

$$L_{xy} = \frac{\mathbf{u}^T \sigma^{-1} \mathbf{x}}{\mathbf{u}^T \sigma^{-1} \mathbf{u}}, \tag{3.6}$$

with $\mathbf{x}$ the vector joining the PV and the dimuon vertex in the transverse plane, $\mathbf{u}$ the unit vector of the dimuon p_{T}, and σ the sum of the PV and SV covariance matrices.

The CMS tracker measures the lifetime variable with a resolution around 10 μm at high p_{T}, degrading to around 30 μm at low p_{T}, so that PR and NP events can be statistically separated, with the former being clustered around $\ell = 0$ and the latter covering the region $\ell > 0$. By defining a lifetime window for PR and NP samples, it is possible to reduce the contamination of NP events in the PR sample and to define a pure NP sample.

Chapter 4

Event samples and selection criteria

The analysis described in this thesis provides the polarizations of the prompt and non-prompt J/ψ and $\psi(2S)$ mesons. The prompt and non-prompt events are selected using the pseudo-proper lifetime observable introduced in Chapter 2. Besides the directly-produced component, the prompt J/ψ event sample includes feed-down contributions, with around 8% of mesons produced in $\psi(2S)$ decays and around 25% produced in χ_c decays [142]. No such feed-down sources contribute to the $\psi(2S)$ sample.

The polarization measurement procedure is described in Chapter 5, up to the determination of the prompt and non-prompt J/ψ and $\psi(2S)$ $\lambda_\vartheta(p_T)$. Before proceeding to the analysis strategy and results, it is first necessary to characterize the event samples used and the selection criteria applied, both online and offline. That is the subject of this chapter.

4.1 Event samples

4.1.1 Data samples

The analysis uses the data samples collected by CMS during the 2017 and 2018 running periods. The integrated luminosity adds up to 103.3 fb^{-1}, distributed as 42.0 and 61.3 fb^{-1} for 2017 and 2018, respectively. The polarization measurement is independent of the exact value of the integrated luminosity, which is reported as it offers a qualitative measure of the size of the analysed event sample.

The events were collected with two dimuon triggers, the HLT paths `HLT_Dimuon25_Jpsi` for the J/ψ and `HLT_Dimuon18_PsiPrime` for the $\psi(2S)$. The L1 seeds are the same for both HLT paths, an OR sum of `L1_DoubleMu4_SQ_OS_dR_Max1p2`, `L1_DoubleMu0er1p5_SQ_OS_dR_Max1p4` and their tighter counterparts `L1_DoubleMu4p5_SQ_OS_dR_Max1p2` and `L1_DoubleMu0er1p4_SQ_OS_dR_Max1p4`, as described in Section 3.3.1.

The HLT path requires an opposite-sign muon pair, with invariant mass in the ranges 2.9–3.33 GeV for the J/ψ and 3.35–4.05 GeV for the $\psi(2S)$, with a distance of closest approach between the two muons smaller than 0.5 cm and a dimuon vertex fit χ^2 probability larger than 0.5%. In addition, the dimuon transverse momentum must be larger than 24.9 GeV for the J/ψ and 17.9 GeV for the $\psi(2S)$. No explicit p_T requirement is imposed on the single muons at this level.

The data samples used in this analysis have been reconstructed with the so-called "ultra-legacy" offline reconstruction software version, which includes the final evaluation of the time-dependent reconstruction parameters, reflecting the alignment and calibration conditions of the detector [143].

The reconstructed data were processed ensuring that both reconstructed muons must match, in pseudorapidity and azimuthal angle, those that triggered the detector readout. Both muon tracks must have more than five hits in the tracker, at least one of them being in a pixel detector layer. They must also fulfil the other standard quarkonium muon selection cuts, as mentioned in Section 3.3.2 (in this case, the so-called "soft-muon selection" [139]).

4.1.2 Monte-Carlo samples

The analysis also uses simulated Monte-Carlo (MC) event samples, generated with the PYTHIA 8 event generator [144], with the standard charmonium production settings. The MC samples are exclusively composed of prompt mesons (pure signal). The generated J/ψ and $\psi(2\mathrm{S})$ mesons only decay to dimuons, for processing efficiency. The decays are isotropic, reflecting unpolarized production. The emitted muons undergo final-state radiation, which is generated through the PHOTOS 3.61 package [145]. The simulation includes PU, with the multiplicity distribution tuned to match the data; the average number of pileup interactions was 32 in the 2017–2018 period. The simulated events are then processed through a detailed simulation of the CMS detector, based on the GEANT4 package [146], using the same trigger and reconstruction algorithms as used to collect and process the data. These samples are independently generated for each of the two years and are expected to faithfully reproduce the running conditions of the CMS experiment during the data collection periods. All samples are generated with the single muons in the kinematical window $p_{\mathrm{T}} > 4$ GeV and $|\eta| < 1.5$, looser than the cuts applied in the offline analysis, mentioned below, to account for smearing effects.

Some of the MC samples were "officially produced" and are available for processing by any CMS analysis. These were complemented by additional MC samples, generated "privately" following the procedures used in the official production, to ensure that the final results are not significantly affected by the statistical uncertainties of the simulated samples.

Particularly, to improve the statistical uncertainties at high p_{T}, several complementary J/ψ MC samples were generated. The MC samples for J/ψ are used in four exclusive ranges: 25–45; 45–50; 50–70; 70–120 GeV. For the $\psi(2\mathrm{S})$ case, a single high-statistics MC sample was used.

4.2 Event selection criteria and definition of analysis samples

The event sample obtained after the triggers is subjected to a further set of offline event selection criteria used to define the "final-analysis event sample":

- Single muon kinematics: $p_{\mathrm{T}} > 5.6$ GeV and $|\eta| < 1.4$;
- Dimuon rapidity: $|y| < 1.2$;

- Dimuon p_T: $25 < p_T < 120$ GeV (J/ψ) or $20 < p_T < 100$ GeV (ψ(2S));
- Dimuon mass: $2.92 < m < 3.28$ GeV (J/ψ) or $3.4 < m < 4.0$ GeV (ψ(2S));
- Dimuon vertex fit χ^2 probability larger than 1%.

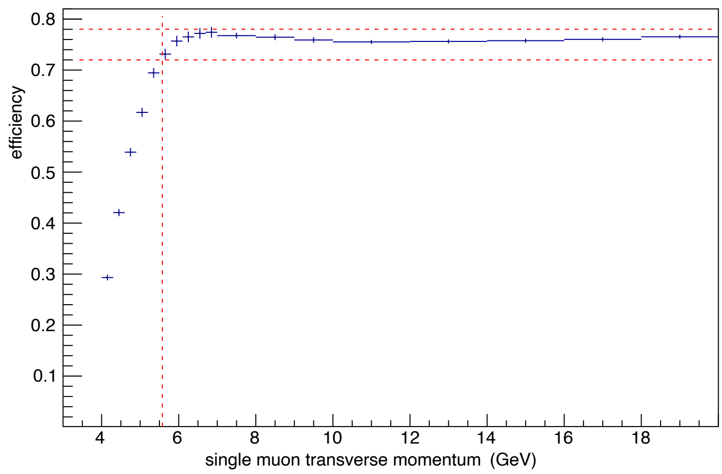

Figure 4.1: Single muon efficiency as a function of p_T, as evaluated from the simulated events.

The offline cut of single muon $p_T > 5.6$ GeV is significantly higher than the cuts applied by the trigger selection. This choice is due to an added consideration, illustrated in Fig. 4.1: with a cut of 5.6 GeV, all the selected muons have detection efficiencies that vary by less than 5%. It is important to note that the polarization measurement is insensitive to the absolute magnitude of the detection efficiencies, so that we only need to worry about the variations of efficiency within the analysed sample matter. By selecting muons in the "plateau" region of the detection efficiency, we avoid the p_T-dependent "turn-on" region of the efficiency curve. This minimises the potential residual effects of a less-than-perfect efficiency correction, so that the results become almost unaffected by the uncertainties on the assumed efficiencies.

The analysis makes use of the $|\cos\vartheta|$ distributions measured in six independent event samples, subsets of the final-analysis event sample defined by two ranges in the dimuon lifetime (denoted by the labels PR and NP) and three in the dimuon mass (J/ψ or ψ(2S) signal region, left and right sidebands):

- PR: $|\ell| < 50$ μm; NP: $100 < \ell < 800$ μm;
- J/ψ signal region: 3.0–3.2 GeV; J/ψ LSB: 2.92–2.95 GeV; J/ψ RSB: 3.21–3.28 GeV;
- ψ(2S) signal region: 3.57–3.81 GeV; ψ(2S) LSB: 3.4–3.52 GeV; ψ(2S) RSB: 3.82–4.0 GeV.

For illustration purposes, the six windows used in the J/ψ and ψ(2S) analysis are graphically represented in Fig. 4.2.

The 2D region of $100 < \ell < 800$ μm and mass in the ψ signal region is labelled as "NPS", for NP in the signal mass window. It includes mesons produced in decays of B mesons (the interesting "signal") as well as a background contribution from non-prompt "mass-continuum" muon pairs. These are the muon pairs resulting from other processes, mostly decays of uncorrelated heavy flavour mesons.

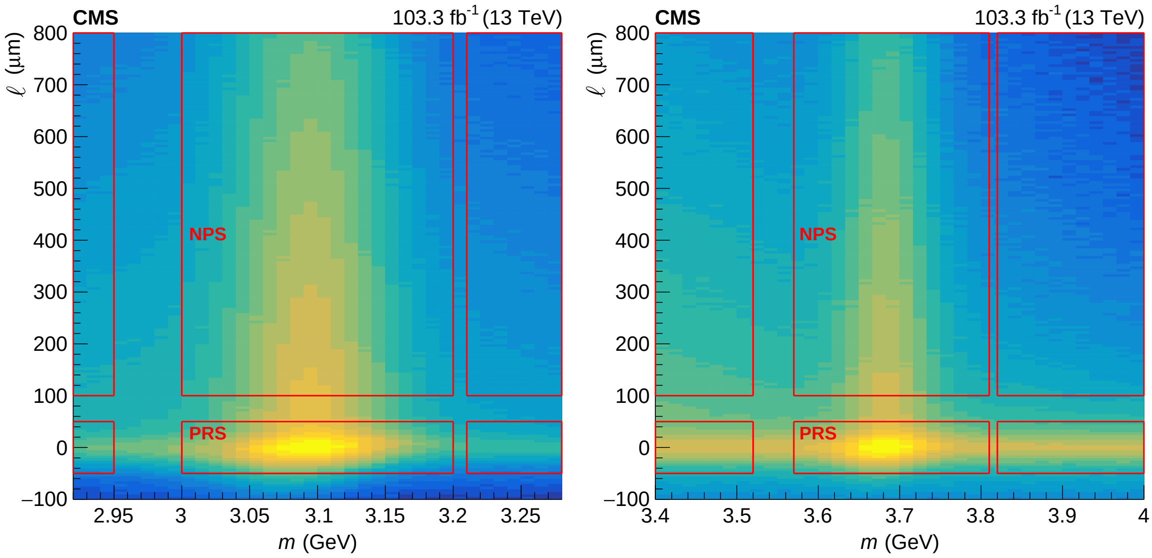

Figure 4.2: Two-dimensional event distribution in the dimuon lifetime vs. mass dimensions, for the 2018 J/ψ (left) and $\psi(2\mathrm{S})$ (right) data samples, showing the rectangular windows defining the six regions used in the analysis. The PRS (NPS) windows include the prompt (non-prompt) signal as well as the background contamination. The other four "control windows", are used to evaluate the $|\cos\vartheta|$ distributions of those backgrounds.

The 2D region of $|\ell| < 50\ \mu$m and mass in the ψ signal region is labelled as "PRS", for PR in the signal mass window. It contains the (signal) prompt mesons plus two background contributions, from "mass continuum" muon pairs and from mesons produced in decays of short-lived B mesons. These mesons are sometimes called "non-prompt", a nomenclature that can be misleading as they have, by definition, $|\ell|$ close to zero.

The MC samples are exclusively composed of prompt J/ψ or $\psi(2\mathrm{S})$ mesons.

The dimuon mass resolution at the J/ψ mass is 20 MeV at $y \sim 0$ and degrades as we depart from mid-rapidity, up to almost 40 MeV in the least favourable phase space regions (rapidity and p_T). Therefore, the 200 MeV window that determines the J/ψ mass signal region corresponds to a coverage between $\pm 5\,\sigma$ and $\pm 2.5\,\sigma$. The same coverage is provided by the 240 MeV window used in the $\psi(2\mathrm{S})$ analysis, given that the relative mass resolution, σ_m/m, is essentially independent of the dimuon mass.

The dimuon pseudo-proper lifetime observable, ℓ, is measured with a resolution around 20–30 μm, so that the range $|\ell| < 50\ \mu$m corresponds to a coverage of around $2\,\sigma$. The PV is selected among all the reconstructed proton-proton collision vertices in the event as the one closest to the line extrapolating the dimuon momentum back to the beam line.

The J/ψ polarization is measured in 19 p_T bins, of widths increasing with increasing p_T:

- 10 bins of 2.5 GeV in the range 25–50 GeV;
- 6 bins of 5 GeV in the range 50–80 GeV;
- 2 bins of 10 GeV in the range 80–100 GeV;
- 1 bin of 20 GeV in the range 100–120 GeV.

Given the smaller event sample, the $\psi(2S)$ polarization measurement is made in only 8 p_T bins, of variable width:

- 4 bins of 5 GeV in the range 20–40 GeV;
- 3 bins of 10 GeV in the range 40–70 GeV;
- 1 bin of 30 GeV in the range 70–100 GeV.

In each of those p_T bins, the $|\cos\vartheta|$ distribution (or ratio of distributions) is analysed in 20 equidistant bins between 0 and 1.

4.2.1 Event yields per year of data taking

After applying the event selection criteria described in the previous section, we are left with almost 15 million prompt and almost 11 million non-prompt J/ψ dimuons with p_T between 25 and 120 GeV. The number of $\psi(2S)$ events is significantly smaller: 2.1 million prompt and 1.3 million non-prompt. All the event yields, for data and MC, are collected in Tables 4.1 and 4.2.

4.3 Illustrations of some kinematical distributions

To characterize the measured and simulated data, and evaluate how the two compare to each other, the distributions of several kinematic variables are shown in the following figures: dimuon invariant mass, p_T, rapidity and lifetime. These illustrations are made with the 2018 J/ψ data, with the 2017 distributions showing identical behaviour in all variables.

Figure 4.3-left compares the measured and simulated invariant mass distributions of the prompt dimuons ($|\ell| < 50\ \mu$m) in the 25–45 GeV (red) and 70–120 GeV (blue) p_T ranges. There are no con-

	2017	[25, 45]	[45, 50]	[50, 70]	[70, 120]	[25, 120]
Data	Prompt signal region (PRS)	5379.7 k	209.5 k	282.2 k	72.7 k	5944.0 k
	Non-prompt signal region (NPS)	4988.5 k	230.9 k	324.0 k	85.6 k	5629.0 k
	Prompt left mass SB (PRLSB)	44.6 k	2.1 k	3.0 k	1.0 k	50.7 k
	Prompt right mass SB (PRRSB)	52.9 k	2.9 k	4.5 k	1.6 k	61.9 k
	Non-prompt left mass SB (NPLSB)	80.6 k	3.8 k	5.2 k	1.4 k	90.9 k
	Non-prompt right mass SB (NPRSB)	86.9 k	4.2 k	5.9 k	1.6 k	98.6 k
MC	Only PRS region	20507.7 k	1555.2 k	1998.9 k	1275.0 k	25336.9 k
	2018	[25, 45]	[45, 50]	[50, 70]	[70, 120]	[25, 120]
Data	Prompt signal region (PRS)	7982.0 k	307.2 k	416.2 k	107.3 k	8812.7 k
	Non-prompt signal region (NPS)	7382.9 k	340.2 k	477.5 k	126.8 k	8327.4 k
	Prompt left mass SB (PRLSB)	69.2 k	3.2 k	4.7 k	1.4 k	78.5 k
	Prompt right mass SB (PRRSB)	79.5 k	4.4 k	6.8 k	2.4 k	93.1 k
	Non-prompt left mass SB (NPLSB)	125.4 k	5.7 k	8.0 k	2.2 k	141.3 k
	Non-prompt right mass SB (NPRSB)	131.6 k	6.2 k	8.5 k	2.3 k	148.6 k
MC	Only PRS region	20984.3 k	1590.1 k	1760.1 k	1598.8 k	25933.3 k

Table 4.1: Event yields of the measured and simulated J/ψ samples, for the 2017 and 2018 sets, per p_T range (in GeV).

	2017	[20, 100]
Data	Prompt signal region (PRS)	854.2 k
	Non-prompt signal region (NPS)	708.0 k
	Prompt left mass SB (PRLSB)	162.0 k
	Prompt right mass SB (PRRSB)	183.9 k
	Non-prompt left mass SB (NPLSB)	191.0 k
	Non-prompt right mass SB (NPRSB)	70.0 k
MC	Only PRS region	5572.2 k
	2018	**[20, 100]**
Data	Prompt signal region (PRS)	1275.8 k
	Non-prompt signal region (NPS)	1053.0 k
	Prompt left mass SB (PRLSB)	242.9 k
	Prompt right mass SB (PRRSB)	275.6 k
	Non-prompt left mass SB (NPLSB)	285.9 k
	Non-prompt right mass SB (NPRSB)	104.7 k
MC	Only PRS region	6660.2 k

Table 4.2: Event yields of the measured and simulated $\psi(2S)$ samples, for the 2017 and 2018 sets, in the full p_T range.

tinuum background dimuons in the MC samples, which are pure (prompt) signal. We see that the mass resolution degrades from low to high p_T.

Figure 4.3-right shows the p_T distributions of the measured PRS data (black) and of the samples simulated in four p_T ranges: 25–46 GeV (in red), 40–52 GeV (in purple), >46 GeV (in green), and >66 GeV (in blue). It should be kept in mind that the “data” sample includes contaminations from J/ψ dimuons produced in B meson decays (even if with $|\ell| < 50$ μm) and from “continuum mass dimuons”, while the simulated samples are pure prompt J/ψ signal.

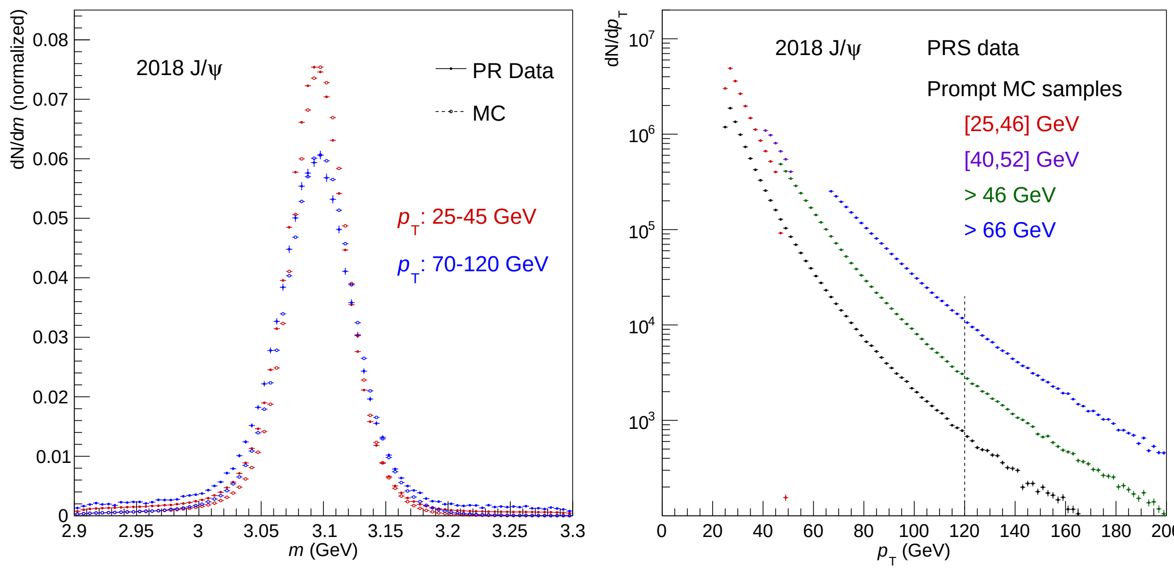

Figure 4.3: Left: Invariant mass distribution of the measured (solid histograms) and simulated (dashed histograms) prompt dimuons ($|\ell| < 50$ μm), in the 25–45 GeV (red) and 70–120 GeV (blue) p_T ranges, for the 2018 J/ψ. Right: Measured (black histogram) p_T distribution of the dimuons in the prompt J/ψ signal region (PRS window: $|\ell| < 50$ μm and $3.0 < m < 3.2$ GeV), compared to the distributions of the four samples of simulated events (red, purple, green, and blue histograms), for 2018.

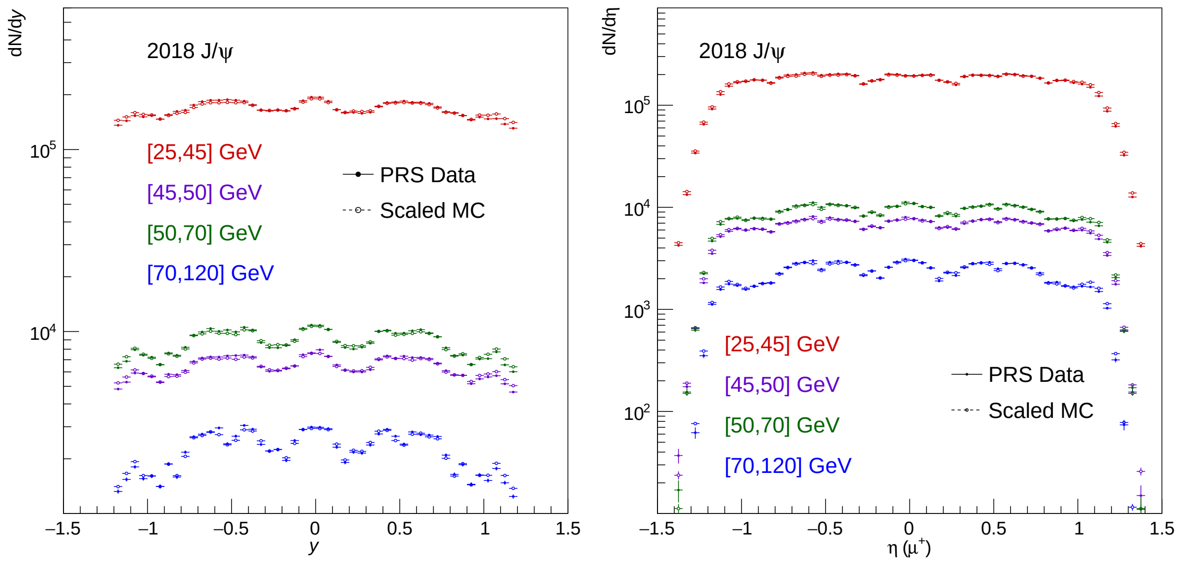

Figure 4.4: Dimuon rapidity (left) and single muon η (right) distributions of the 2018 measured (solid histograms) and simulated (dashed histograms) samples in the prompt J/ψ mass region (PRS), in four dimuon p_T ranges (red, purple, green, and blue histograms), rescaling the MC distributions for an easier comparison with the data shapes.

We have verified the compatibility of the four MC samples used for the J/ψ analysis, each generated over a different interval in dimuon p_T. In order to do this, several distributions of variables were obtained in p_T intervals where the samples overlap, obtaining pairs of distributions that can be compared for the 2017 and 2018 samples: dimuon mass, p_T and rapidity, as well as single muon p_T and η. All distributions show good agreement across all three overlap p_T regions for both 2017 and 2018.

Figure 4.4 compares the J/ψ data and MC dimuon rapidity distributions (left panel) and single muon η distributions (right panel), in the four p_T ranges As both muons have identical distributions, only the positive muon is shown. For an easier comparison of the shapes, the MC distributions are scaled to the data. The data-MC agreement is quite remarkable.

As previously mentioned and graphically shown in Fig. 4.2, the PRS, PRLSB, and PRRSB event samples only include dimuons of pseudo-proper lifetime between -50 and +50 μm. Instead, the NP event sample is composed of dimuons with pseudo-proper lifetime between 100 and 800 μm. Figure 4.5 shows the lifetime distribution of the measured J/ψ dimuons, indicating the prompt and non-prompt windows with the vertical dashed lines and the two horizontal arrows. No simulated distributions are shown here because the MC is exclusively composed of prompt signal J/ψ events. We can see that the resolution of the lifetime measurement improves from low to high p_T and that the NP fraction increases with p_T and then flattens out.

As mentioned above, the 2017 and 2018 samples show equivalent distributions for all plotted single muon and dimuon distributions. This is illustrated in Fig. 4.6, where the dimuon p_T and lifetime distributions are plotted identically to Figs. 4.3-right and 4.5, now overlapping the 2017 distributions after scaling them to their 2018 counterparts. The agreement is remarkable for both variables.

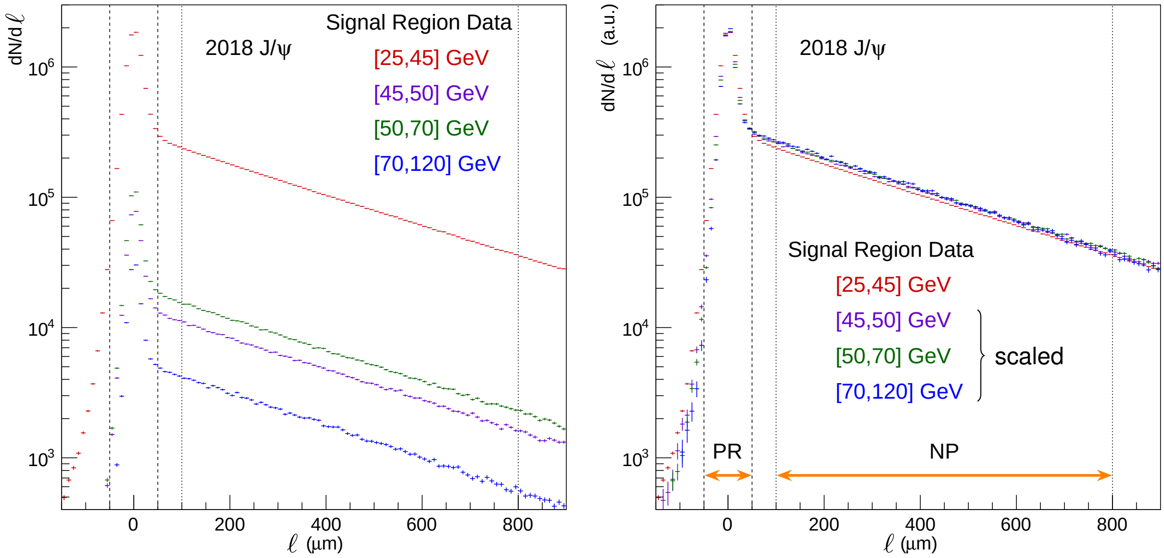

Figure 4.5: Pseudo-proper lifetime distributions of the 2018 dimuons measured in the 3.0–3.2 GeV mass window. The vertical lines indicate the “prompt” (dashed) and “non-prompt” (dotted) windows.

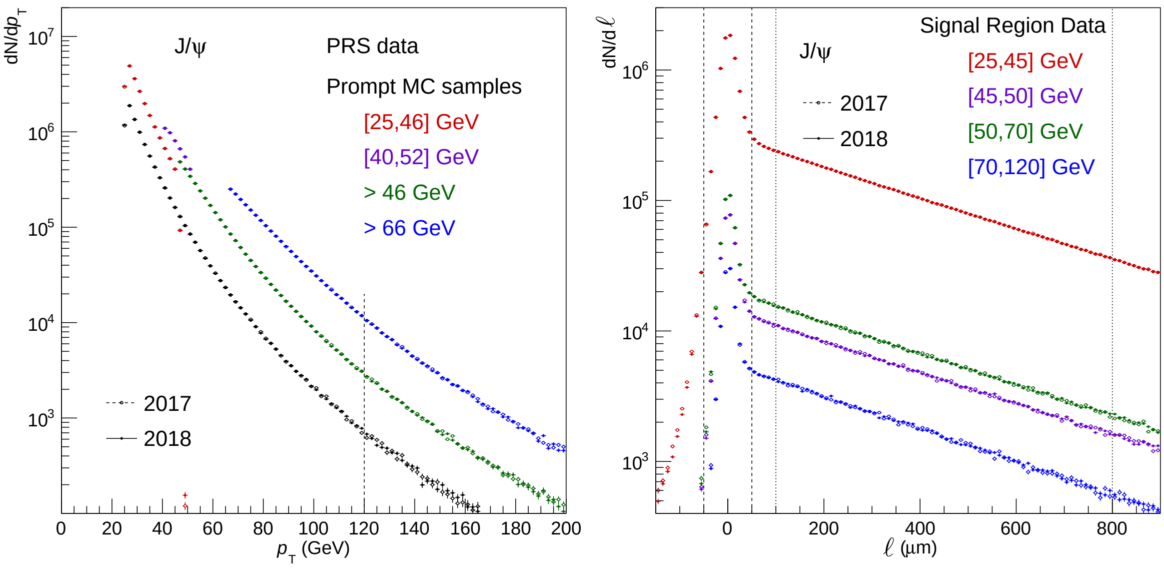

Figure 4.6: Comparison of 2017 and 2018 dimuon distributions, rescaling the 2017 distributions for an easier comparison: p_{T} in the J/ψ PRS region (left) and lifetime in the J/ψ signal mass window (right).

Equivalent illustrations are obtained for the $\psi(2\mathrm{S})$ case, where there is a single MC sample and so the full p_{T} range of [20,100] GeV is the single p_{T} interval used for plotting. As for the J/ψ, the illustrations are made with the 2018 samples and, for the single muon η distributions, with μ^+.

In this case, as can be seen in Fig. 4.7-left, the measured sample includes a significant contribution from continuum background dimuons.

Figure 4.7-right shows the p_{T} distributions of the measured and simulated samples. The upper limit of $p_{\mathrm{T}} = 100$ GeV for the $\psi(2\mathrm{S})$ measurement is illustrated by a dashed vertical line, and the statistical fluctuations above this p_{T} cut are clearly visible, reflecting the smaller sample size for this state.

The dimuon rapidity distributions, illustrated in the left panel of Fig. 4.8, show great agreement between data and MC, as do the single muon η distributions on the right panel.

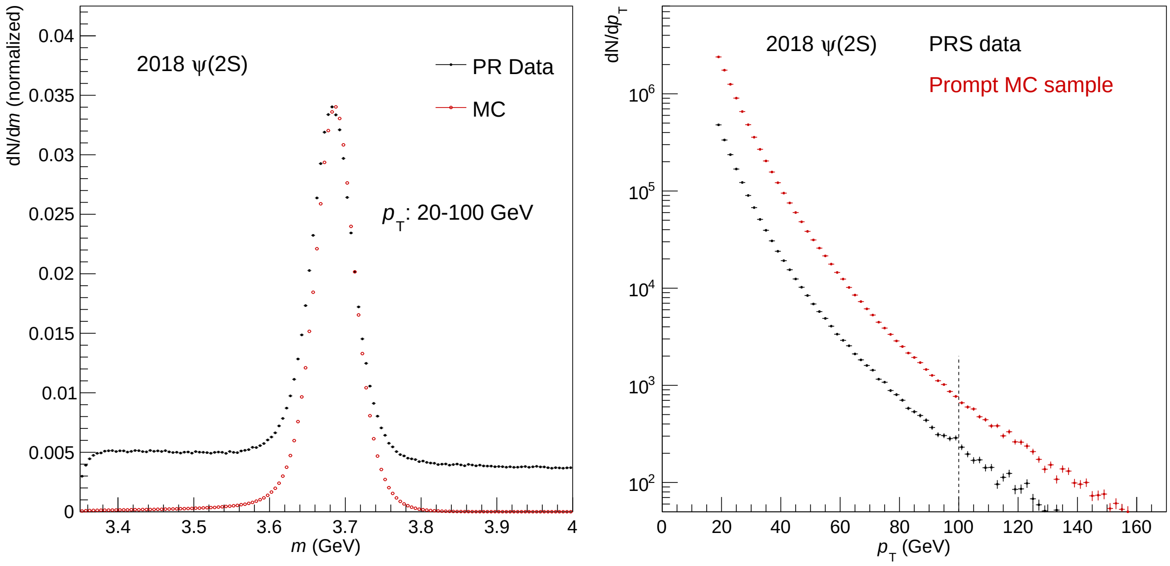

Figure 4.7: Left: Invariant mass distribution of the measured (solid) and simulated (dashed) prompt dimuons ($|\ell| < 50$ μm), integrated over $p_{\rm T}$, for the 2018 $\psi(2{\rm S})$. Right: Measured (black) and simulated (red) $p_{\rm T}$ distributions of the dimuons in the prompt $\psi(2{\rm S})$ signal region ($|\ell| < 50$ μm and $3.57 < m < 3.81$ GeV), for 2018.

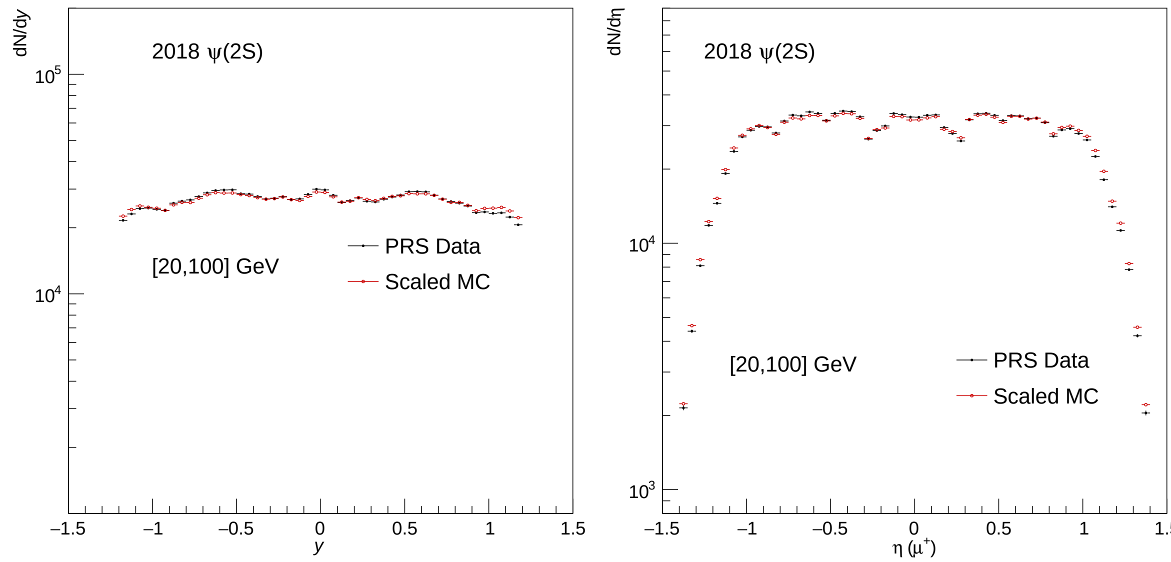

Figure 4.8: Dimuon rapidity (left) and single muon η (right) distributions of the 2018 measured (solid histograms) and simulated (dashed histograms) samples in the prompt $\psi(2{\rm S})$ mass region (PRS), integrated over $p_{\rm T}$, rescaling the MC distributions for an easier comparison with the data shapes.

Chapter 5

Measurement of the J/ψ and $\psi(2\mathrm{S})$ polarizations

5.1 A brief overview of the analysis

The polarization measurement is, as mentioned previously, based on the analysis of the angular distributions of the dimuons resulting from the decay of the quarkonium mesons. The 4-momentum vectors of the two muons, containing the spin alignment information of the decaying meson, are used to extract the anisotropy parameters λ.

In the phase space window of the analysis, studying mid-rapidity and high-p_T quarkonia, the HX frame appears to be the most natural, as indicated in Section 2.4.2. In these conditions, it is very reasonable to focus the analysis by presenting the main results in the form of the polar anisotropy parameter, λ_ϑ, in the HX frame. Other anisotropy parameters offer useful cross-checks.

The polar anisotropy parameter is determined using a simplified version of Eq. 2.2, integrating over the azimuthal decay angle,

$$W(\cos\vartheta) \propto 1 + \lambda_\vartheta \cos^2\vartheta \; . \tag{5.1}$$

This integration is possible because the angular variables $\cos\vartheta$ and φ show little correlation in the HX frame, at high p_T and mid-rapidity. An alternative reference frame, such as the Collins–Soper frame, would not allow for such an approach, as the $\cos\vartheta$ vs. φ phase space has zero-acceptance domains, so that a two-dimensional analysis becomes necessary. This is illustrated in Fig. 5.1, which shows the two-dimensional acceptance and efficiency maps in the HX and Collins–Soper (CS) frames, in two p_T bins, using the simulated J/ψ samples. The "holes" in the CS distributions correspond to zero-acceptance regions that impose an inextricable correlation between the two ($\cos\vartheta$ and φ) dimensions, while the HX distributions are nearly rectangular, especially at high p_T.

To probe the possible existence of a residual azimuthal anisotropy, as will be considered when performing the systematic checks of Chapter 6, the analysis can be redone, in exactly the same way,

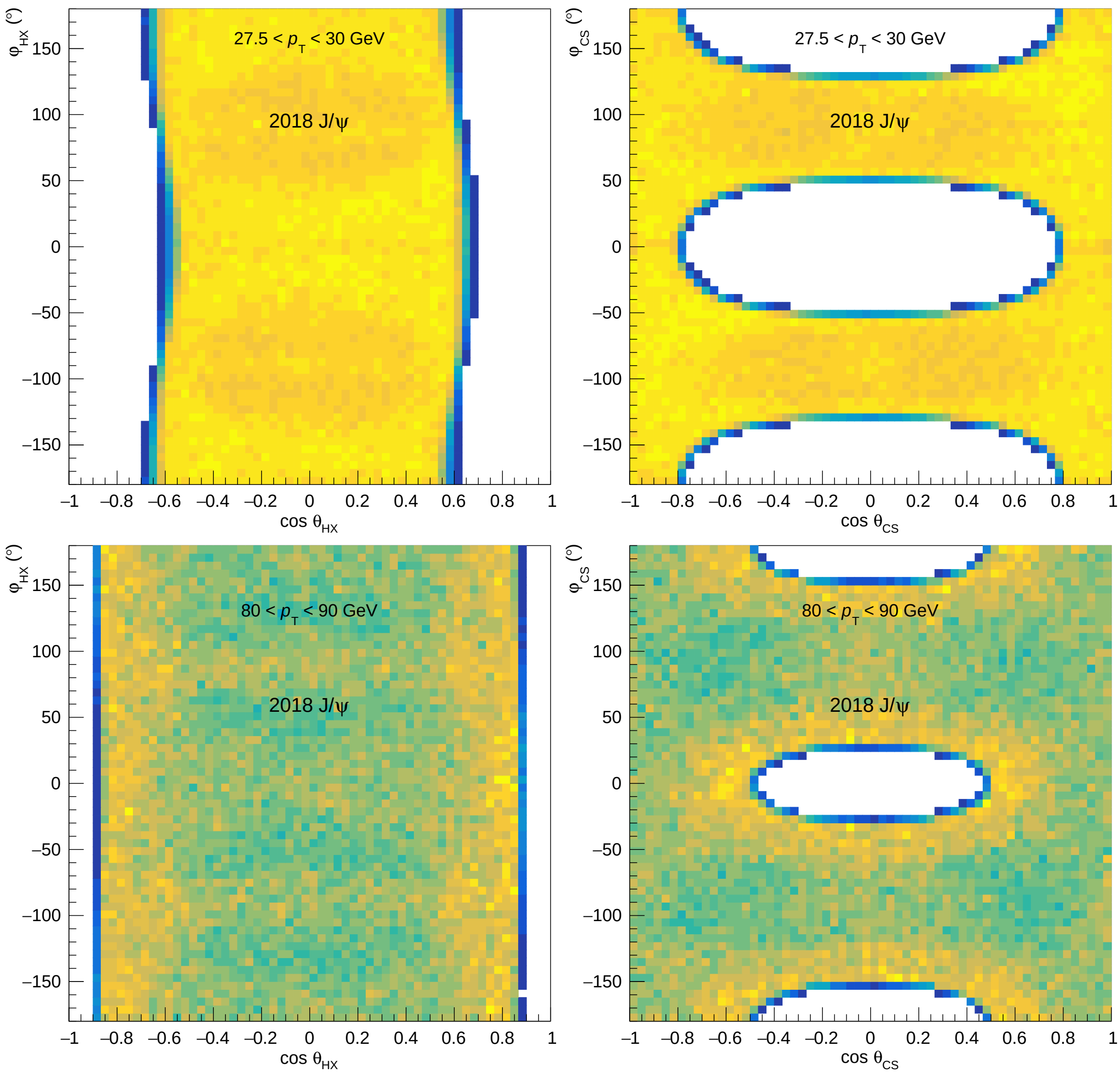

Figure 5.1: Two-dimensional J/ψ $(\cos\vartheta, \varphi)$ acceptance maps in the HX (left) and CS (right) frames, for two p_T bins.

replacing the $\cos\vartheta$ polar angle by the φ azimuthal angle. The φ distributions are fitted with the function

$$W(\varphi|\vec{\lambda}) \propto 1 + \beta\cos 2\varphi\ , \tag{5.2}$$

with $\beta = (2\,\lambda_\varphi)/(3+\lambda_\theta)$, obtained from Eq. 2.2 integrating over the polar decay angle.

A few additional considerations are required before the polarization measurement can be performed. Firstly, the analysis is made using the observable $|\cos\vartheta|$. Indeed, the symmetry of the underlying physics implies that the distribution must be symmetric around zero and, hence, there is no information gain in using the $\cos\vartheta$ variable. By graphically representing the distributions vs. $|\cos\vartheta|$, the statistical fluctuations of the data points are reduced.

More importantly, the analysis is made in many p_T bins, in order to measure the p_T dependence of λ_ϑ. The p_T bins are relatively narrow, especially at low p_T, with the further aim of ensuring that, within those bins, the variation of the polarization (if there is any) can be neglected.

This analysis is made integrated over the dimuon rapidity window $|y| < 1.2$, without splitting this (relatively narrow) mid-rapidity window into thinner bins. This integration is justified by the observation that no variations of the polarization are expected in any theory model within that mid-rapidity range, a prediction in good agreement with the results of previous CMS analyses.

In these conditions, Eq. 5.1 can be written as

$$W(|\cos\vartheta|, p_\mathrm{T}) \propto 1 + \lambda_\vartheta(p_\mathrm{T})\cos^2\vartheta \ . \tag{5.3}$$

A bigger challenge of the analysis is that Eq. 5.3 cannot be used to directly fit the measured ("raw data") $|\cos\vartheta|$ distributions because they are affected by sculpting effects introduced by the limited acceptance coverage of the detector and by the efficiencies of the trigger and reconstruction steps. In other words, the fit must be done on distributions previously corrected for those experimental effects.

As in all other previous analyses, the detection acceptance is evaluated through a very detailed ("full") simulation of the whole detection chain, from the trigger step to the offline reconstruction and event selection criteria. This Monte Carlo simulation is made assuming unpolarized production, corresponding to a flat $\cos\vartheta$ distribution, so that any non-flat trends seen in the simulated distributions are caused by the convolution of all the detection effects (mainly the acceptance, but also the single muon and dimuon efficiencies).

The procedure is thus to divide (in each p_T bin) the measured $|\cos\vartheta|$ distribution by the simulated one, before performing the fit using Eq. 5.3. In this way, the only remaining reason for potential modulations of the angular distribution is the polarization of the measured charmonium samples.

Given the considerations above, the basic inputs for the polarization measurement can be considered to be the two-dimensional $|\cos\vartheta|$ vs. p_T event distributions, for the data and for the MC. These are shown in Fig. 5.2, for the 2018 J/ψ event sample, in the PRS region, after applying all the event selection criteria. The analogous distributions for the NPS region, as well as for the 2017 data taking period, are virtually indistinguishable from the ones shown here. Since the MC samples are generated unpolarized, the non-flatness of this distribution versus $|\cos\vartheta|$, shown in the right panel, is a direct reflection of the detection acceptance. The measured data, instead, is also affected by the physics polarization effects that are the target of this analysis.

Besides the expected exponential decrease in event yields as p_T increases, which simply reflects the decreasing p_T-differential production cross section, the first observation that can be made from these figures is that the coverage in $|\cos\vartheta|$ extends to larger values when the dimuons have a larger p_T. In fact, it is the single muon p_T cut that limits the $|\cos\vartheta|$ vs. dimuon p_T phase space. When a dimuon has $|\cos\vartheta|$ close to 1, it means that the two muons are "back to back", one having a significantly higher momentum than the other. The muon with lower momentum is likely to fail the $p_\mathrm{T} > 5.6$ GeV requirement, especially at low dimuon p_T, making the $\cos\vartheta$ regions close to ±1 inaccessible. As the dimuon p_T increases, the impact of the muon p_T cut becomes less important and the measured $|\cos\vartheta|$ distribution extends towards higher values of $|\cos\vartheta|$, as shown in Fig. 5.3. In other words, the maximum value of the $|\cos\vartheta|$ variable that can be probed with the selected data increases with dimuon p_T, which is another good reason to

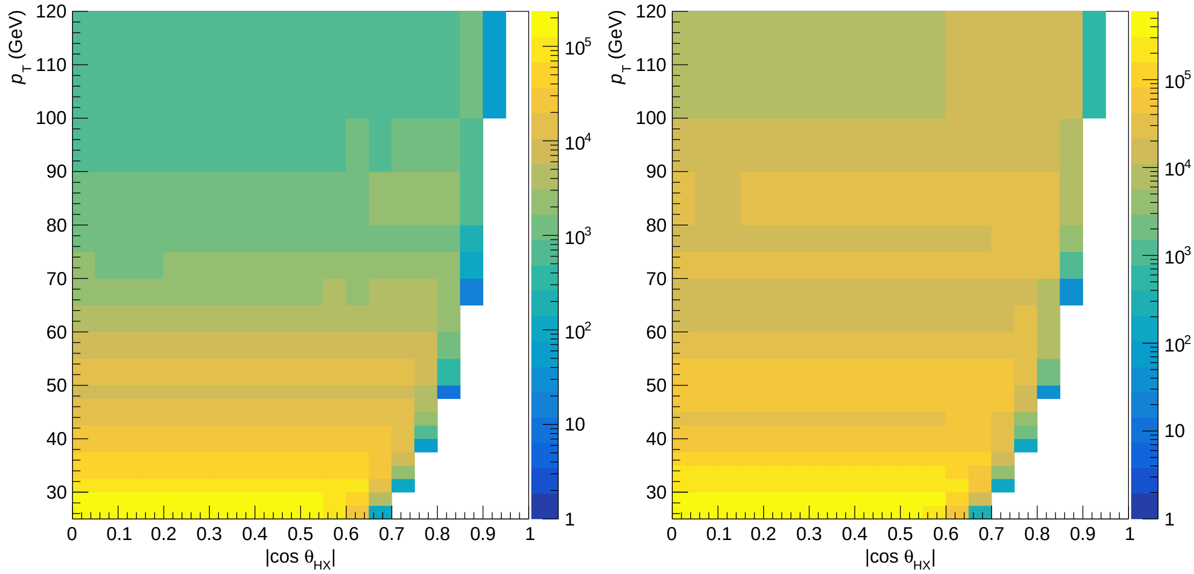

Figure 5.2: Two-dimensional J/ψ $(|\cos\vartheta|, p_{\mathrm{T}})$ distributions for 2018 PRS data (left) and signal-only MC (right).

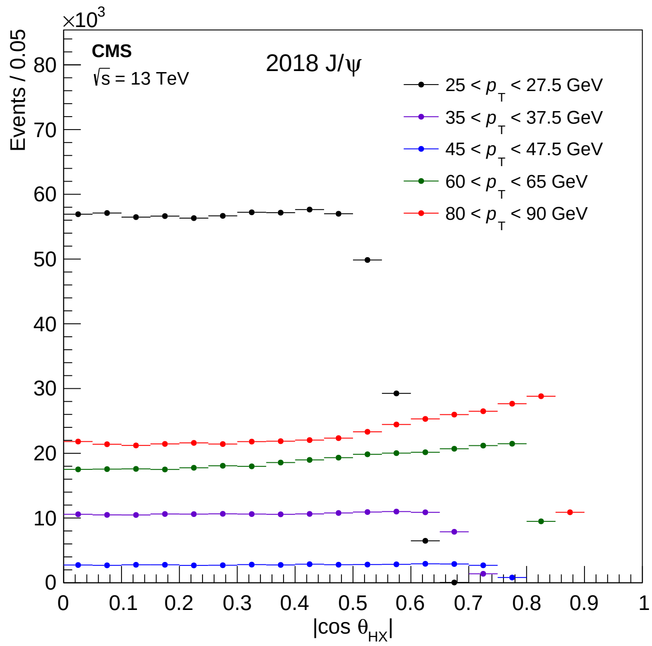

Figure 5.3: Simulated $|\cos\vartheta|$ distributions, in five J/ψ p_{T} ranges, showing that the $|\cos\vartheta|$ coverage increases with p_{T}.

perform the analysis as a function of p_{T}.

It is worth noting that this means that the polarization measurement becomes easier to perform as the J/ψ p_{T} increases (as long as the size of the event samples remains sufficiently large). Indeed, given the form of Eq. 5.3, the shape of the $\cos\vartheta$ distribution away from zero has the most significant contribution to the determination of λ_ϑ. Data that only cover a $\cos\vartheta$ range very close to zero are unable to provide a faithful measurement of λ_ϑ.

As mentioned before, the analysis must be made using the data over MC ratios. Figure 5.4 shows an example of such a ratio, for the PRS region, using the 2018 data and MC J/ψ samples. Note that the

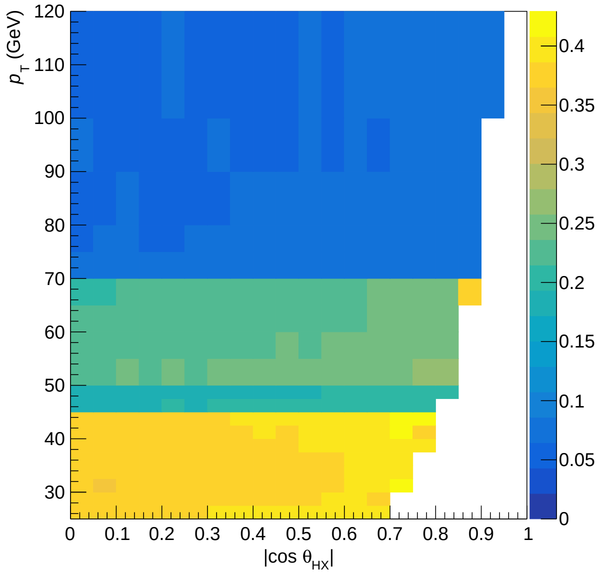

Figure 5.4: Data over MC ratio of the J/ψ $(|\cos\vartheta|, p_T)$ 2D distributions for the PRS region, using the 2018 samples.

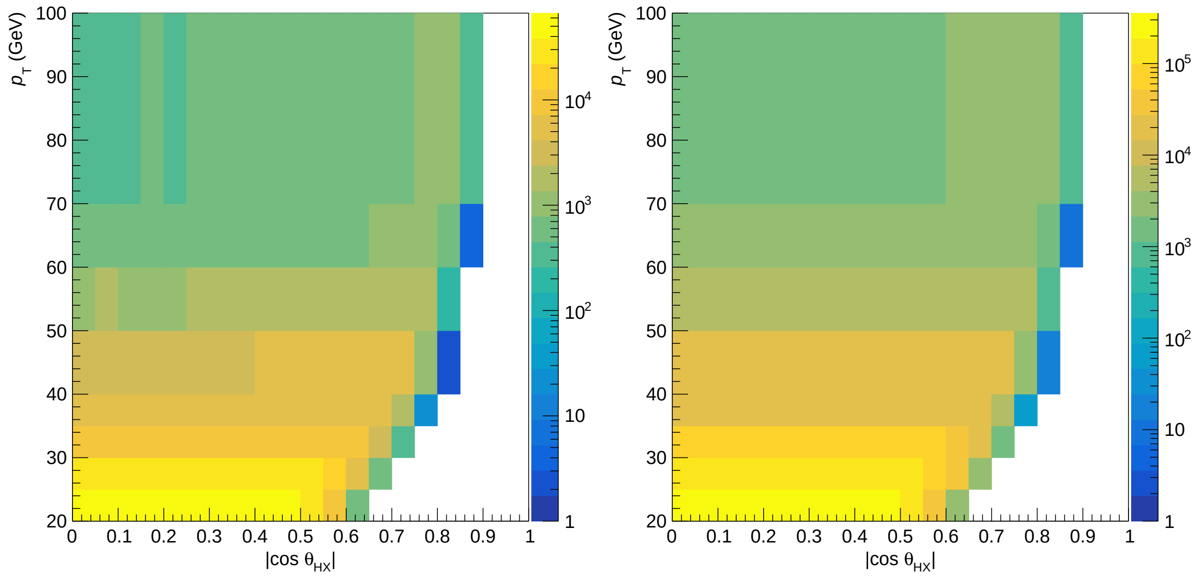

Figure 5.5: Two-dimensional $\psi(2S)$ $(|\cos\vartheta|, p_T)$ distributions for 2018 PRS data (left) and signal-only MC (right).

four "bands" visible in the figure are simply reflecting the four different MC generations used for the J/ψ. This is a visual artefact, due to the increased number of MC events generated at high p_T, but it will not affect the final λ_ϑ results, which only depend on the shape of the $|\cos\vartheta|$ distribution in each p_T bin.

The detection effects cancel in the ratio, so that its study will provide a reliable measurement of the polarizations. Indeed, the polarization is the only effect that is present in the measured distributions and not in the simulated ones, so that it is the only possible cause of any potential non-flatness of the ratios. Figures 5.5 and 5.6 show the $\psi(2S)$ equivalent of Figs. 5.2 and 5.4, respectively.

To ensure stable and reliable fit results, the $1 + \lambda_\vartheta \cos^2\theta$ function is fitted within a $|\cos\vartheta|$ range that excludes the most extreme values, where the distribution (corrected for acceptance and efficiency

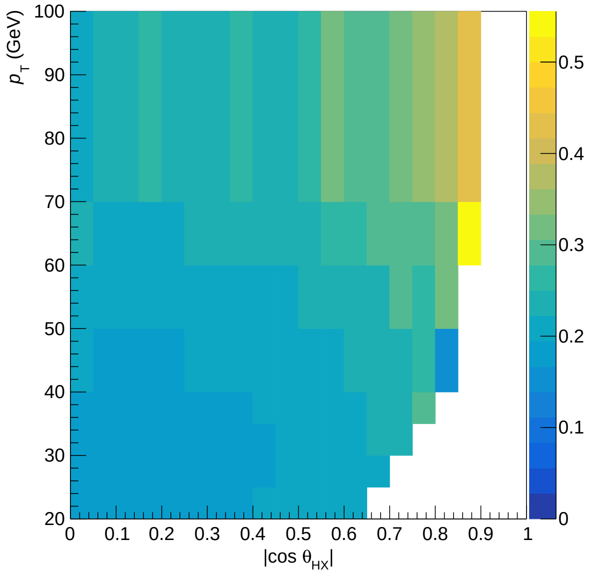

Figure 5.6: Data over MC ratio of the $\psi(2\mathrm{S})$ $(|\cos\vartheta|, p_\mathrm{T})$ 2D distributions for the PRS region, using the 2018 samples.

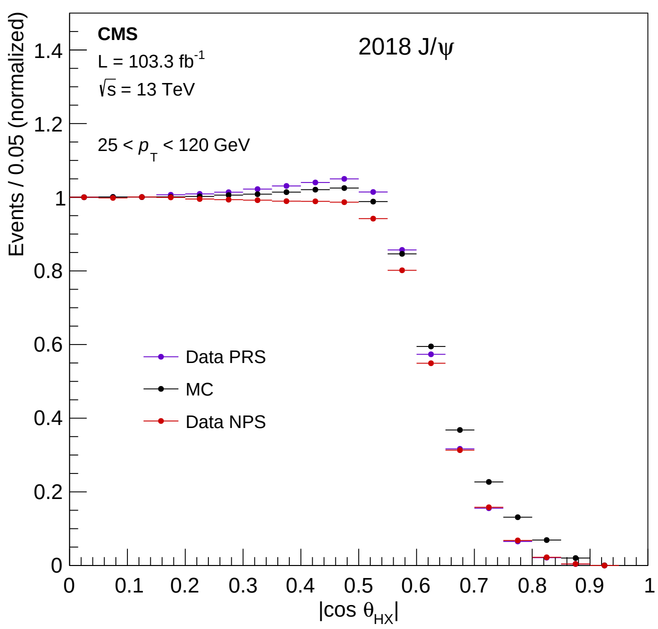

Figure 5.7: Measured PRS (purple) and NPS (red) J/ψ $|\cos\vartheta|$ distributions compared to the MC simulated (unpolarized) distribution (black), immediately illustrating the transverse or longitudinal polarizations of the measured samples.

effects) is the ratio of two steeply falling distributions and, hence, might be affected by spurious "edge effects".

Before going into more complex descriptions of the analysis procedures, it is worth noting that, even without doing any fits, a direct look at the J/ψ $|\cos\vartheta|$ distributions, shown in Fig. 5.7 for the PRS, NPS, and MC cases, integrated over p_T, is sufficient to see that the PRS dimuons are transversely polarized while the NPS dimuons, instead, are longitudinally polarized. This observation can be easily made by comparing the PRS and NPS shapes with that of the unpolarized MC distribution, taken as reference.

Several comparisons have been made between the 2017 and 2018 samples, including independent fits of the dimuon mass and lifetime distributions of each of those samples, leading to the conclusion that the two samples are in perfect agreement with each other, within uncertainties. This observation means that, moving forward, the analysis can be performed using the combined “Run 2” event sample. In this way, free parameters can be fitted with less statistical uncertainties and any dependences on variables such as the dimuon p_{T}, for example, can be determined more precisely. Residual variations between the two event samples, if any, will be considered as a potential systematic uncertainty, evaluated from the differences between the results independently obtained for each year. This applies, independently, to the prompt and non-prompt J/ψ and $\psi(2\mathrm{S})$ measurements.

Adding both years, the event yields, per 2D region and p_{T} range, are collected in the Tables 5.1 and 5.2, for the J/ψ and $\psi(2\mathrm{S})$ cases, respectively.

		[25, 45]	[45, 50]	[50, 70]	[70, 120]	[25, 120]
Data	Prompt signal region (PRS)	13361.7 k	516.7 k	698.3 k	180.0 k	14756.7 k
	Non-prompt signal region (NPS)	12371.5 k	571.2 k	801.5 k	212.3 k	13956.4 k
	Prompt left mass SB (PRLSB)	113.8 k	5.2 k	7.7 k	2.4 k	129.2 k
	Prompt right mass SB (PRRSB)	132.4 k	7.3 k	11.3 k	4.0 k	155.0 k
	Non-prompt left mass SB (NPLSB)	206.0 k	9.5 k	13.2 k	3.6 k	232.3 k
	Non-prompt right mass SB (NPRSB)	218.6 k	10.4 k	14.3 k	4.0 k	247.2 k
MC	Only PRS region	41492.1 k	3145.4 k	3759.0 k	2873.8 k	51270.2 k

Table 5.1: Event yields of the measured and simulated J/ψ samples, adding the 2017 and 2018 sets, per p_{T} range (in GeV).

		[20, 100]
Data	Prompt signal region (PRS)	2130.0 k
	Non-prompt signal region (NPS)	1761.0 k
	Prompt left mass SB (PRLSB)	404.8 k
	Prompt right mass SB (PRRSB)	459.5 k
	Non-prompt left mass SB (NPLSB)	476.8 k
	Non-prompt right mass SB (NPRSB)	174.8 k
MC	Only PRS region	12232.4 k

Table 5.2: Event yields of the measured and simulated $\psi(2\mathrm{S})$ samples, adding the 2017 and 2018 sets, in the full p_{T} range (20–100 GeV).

To conclude this section, the inputs needed for the polarization measurement are quickly introduced.

To begin, the measurement of the polarizations of the non-prompt J/ψ and $\psi(2\mathrm{S})$ mesons is described. These mesons are daughters of B mesons (and of a negligible contribution from other b baryon decays) and, hence, denoted as ψ_{B}. The dimuons contributing to the non-prompt signal $|\cos\vartheta|$ distribution in a given p_{T} bin, NPS$(|\cos\vartheta|, p_{\mathrm{T}})$, come either from decays of ψ_{B} mesons or from non-prompt mass-continuum background processes, B_{NP},

$$\begin{aligned}\text{NPS}(|\cos\vartheta|, p_{\mathrm{T}}) = {} & f^{\mathrm{NPS}}_{\psi_{\mathrm{B}}}(p_{\mathrm{T}}) \cdot \psi_{\mathrm{B}}(|\cos\vartheta|, p_{\mathrm{T}}) \\ & + f^{\mathrm{NPS}}_{\mathrm{B_{NP}}}(p_{\mathrm{T}}) \cdot B_{\mathrm{NP}}(|\cos\vartheta|, p_{\mathrm{T}})\,,\end{aligned} \tag{5.4}$$

with $f^{\mathrm{NPS}}_{\psi_{\mathrm{B}}}(p_{\mathrm{T}}) = 1 - f^{\mathrm{NPS}}_{\mathrm{B_{NP}}}(p_{\mathrm{T}})$.

Similarly, the polarizations of the prompt J/ψ and $\psi(2\mathrm{S})$ mesons, ψ_{P}, can also be measured, in each

p_{T} bin, using the $|\cos\vartheta|$ distributions of the dimuons in the prompt signal region, PRS($|\cos\vartheta|, p_{\mathrm{T}}$). However, besides the dimuons from prompt charmonia and from mass-continuum background processes, B_{PR}, the PRS window also includes events from charmonia produced in decays of short-lived B mesons, of $|\ell| < 50\,\mu$m,

$$\begin{aligned}\mathrm{PRS}(|\cos\vartheta|, p_{\mathrm{T}}) = & f^{\mathrm{PRS}}_{\psi_{\mathrm{P}}}(p_{\mathrm{T}}) \cdot \psi_{\mathrm{P}}(|\cos\vartheta|, p_{\mathrm{T}}) \\ & + f^{\mathrm{PRS}}_{\mathrm{B_{PR}}}(p_{\mathrm{T}}) \cdot B_{\mathrm{PR}}(|\cos\vartheta|, p_{\mathrm{T}}) + f^{\mathrm{PRS}}_{\psi_{\mathrm{B}}}(p_{\mathrm{T}}) \cdot \psi_{\mathrm{B}}(|\cos\vartheta|, p_{\mathrm{T}}) \,,\end{aligned} \tag{5.5}$$

with $f^{\mathrm{PRS}}_{\psi_{\mathrm{P}}}(p_{\mathrm{T}}) = 1 - f^{\mathrm{PRS}}_{\mathrm{B_{PR}}}(p_{\mathrm{T}}) - f^{\mathrm{PRS}}_{\psi_{\mathrm{B}}}(p_{\mathrm{T}})$.

The fractions of mass-continuum muon pairs in the signal windows, $f^{\mathrm{NPS}}_{\mathrm{B_{NP}}}$ and $f^{\mathrm{PRS}}_{\mathrm{B_{PR}}}$, are determined from fits of the dimuon mass distributions, while the fractions of charmonia from B decays in the prompt signal window, $f^{\mathrm{PRS}}_{\psi_{\mathrm{B}}}$, are obtained by fitting the dimuon lifetime distributions, accounting for the existence of non-prompt continuum muon pairs. It should be noted that the mass-continuum dimuons in the PR region also include, besides the prompt Drell–Yan dimuons, several possible combinations of muons produced in (non-prompt) decays of pions, kaons, D mesons, and B mesons. The next section explains how the three fractions are measured, for each of the two charmonia and as functions of p_{T}, and reports the results, which are then used in the measurement of the polarizations, as described in Section 5.3.

5.2 Dimuon mass and lifetime analysis

5.2.1 Background fractions in the non-prompt charmonia signal regions

As mentioned above, in the NPS region, there is a single background fraction to evaluate, $f^{\mathrm{NPS}}_{\mathrm{B_{NP}}}$. This fraction is determined from fits of the non-prompt J/ψ and $\psi(2\mathrm{S})$ dimuon mass distributions. While conceptually identical, the fits for each state differ in the fit functions used to describe the signal line shape. The $\psi(2\mathrm{S})$ case is described first, for simplicity.

The eight dimuon mass distributions (corresponding to the eight $\psi(2\mathrm{S})$ p_{T} bins) are simultaneously fitted by the sum of two Crystal-Ball (CB) functions [147] to describe the $\psi(2\mathrm{S})$ line shape (L_ψ) plus a decreasing exponential function to describe the underlying mass-continuum background (L_{Bg}):

$$L_\psi = f_{\mathrm{CB1}} \cdot g_{\mathrm{CB1}}(m) + (1 - f_{\mathrm{CB1}}) \cdot g_{\mathrm{CB2}}(m) \tag{5.6}$$

$$L_{\mathrm{Bg}} = A_{\mathrm{Bg}} \cdot \exp(-m/t_{\mathrm{Bg}}) \tag{5.7}$$

Independently fitting the dimuon mass distributions in each of the p_{T} bins would naturally lead to results affected by random statistical fluctuations, especially if all shape parameters were left free. Some of the parameters, such as the n and α tail parameters, are (anti-)correlated and, thus, it is not reasonable to leave all parameters free in the fit. Additionally, the shape parameters of the L_ψ and L_{Bg} functions are expected to change with p_{T} in a smooth way.

Given these considerations, a series of preliminary studies of the (simulated and measured) dimuon mass distributions were performed, aiming at reducing the number of free parameters of the fit. These

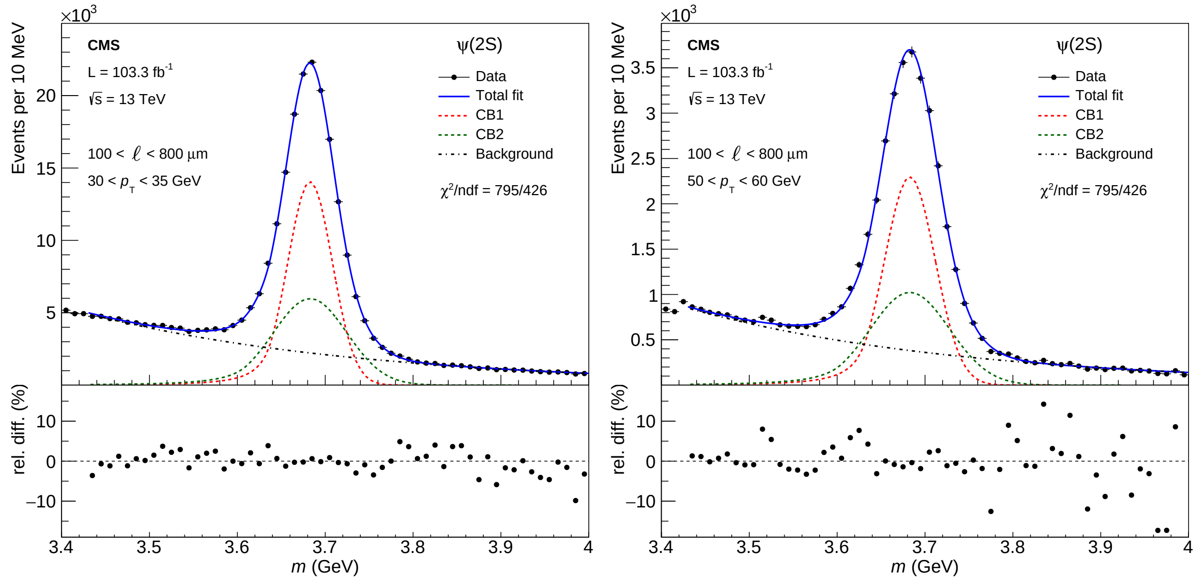

Figure 5.8: Dimuon mass distributions measured for the non-prompt $\psi(2\mathrm{S})$ in the two p_T bins mentioned in the legends. The total fit function (blue line), the two CB functions (red and green), and the background continuum (black) are also shown. The lower panels show the corresponding relative difference distributions.

converged on a fit model that is able to faithfully describe the data with a relatively small number of free shape parameters, by constraining their dependence on p_T. The two CB functions have common means ($\mu_1 = \mu_2$) and tail parameters n and α, but independent widths (σ_1 and σ_2). The CB means and their relative proportions are independent of p_T, as is the value of α, while the two widths increase linearly with p_T, with a common slope. The tail parameter n is fixed to the value 2.5 (given the strong correlation between n and α, it is reasonable to only leave one of them as a free parameter in the fit). This relatively simple model strikes a good balance, avoiding too many free parameters (leading to under-constrained fits and results affected by random statistical fluctuations) or too many arbitrarily-selected constraints (possibly leading to results biased by specific assumptions).

Figure 5.8 shows, for illustration, two measured non-prompt $\psi(2\mathrm{S})$ dimuon mass distributions, in two typical p_T bins. The lower panels show the corresponding distributions of relative differences, computed as the difference between the measured and fitted yields, divided by the fitted yield. The quality of the fit, simultaneously made to the eight mass distributions, is represented by the χ^2/ndf value mentioned in the figures, where ndf stands for the number of degrees of freedom.

Since there is a much larger number of J/ψ events than $\psi(2\mathrm{S})$ events, with respect to the yield of underlying mass-continuum dimuons, a slightly more complex J/ψ signal fit model is needed. First, the two CB functions are no longer constrained to have a common mean; instead, μ_1 is made independent of p_T and μ_2 is left free in each p_T bin. Second, a Gaussian function is added, with μ_1 as mean and an independent width, σ_G:

$$L_\psi = f_\mathrm{CB1} \cdot g_\mathrm{CB1}(m) + (1 - f_\mathrm{CB1} - f_G) \cdot g_\mathrm{CB2}(m) + f_G \cdot g_G(m) \tag{5.8}$$

The normalization of the Gaussian term is fixed, from studies of the MC event samples, so that it

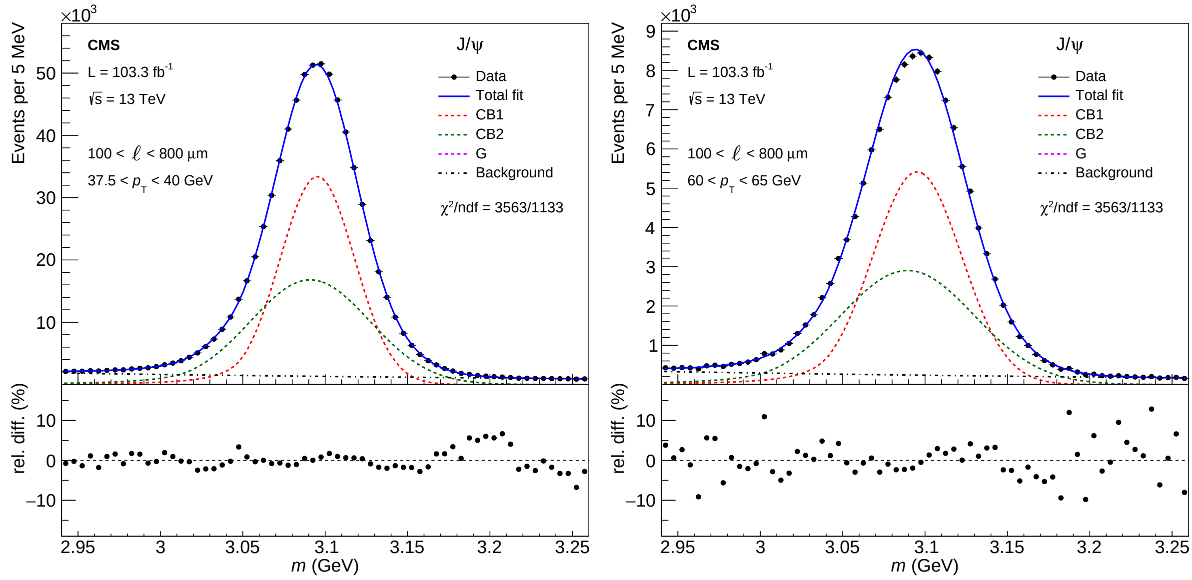

Figure 5.9: Dimuon mass distributions measured for the non-prompt J/ψ in the two p_{T} bins mentioned in the legends. The total fit function (blue line), the two CB functions (red and green), the Gaussian function (magenta), and the background continuum (black) are also shown. The lower panels show the corresponding relative difference distributions.

contributes 3.5% of the total J/ψ yield. Simultaneously fitting all the 19 J/ψ dimuon mass distributions, a good description of the data is obtained with a σ_G parameter that increases linearly with p_{T} with the same slope as σ_1 and σ_2. Although a small correction for the J/ψ shape, adding the Gaussian term provides an improved description of the mass-continuum region immediately above the J/ψ peak.

Figure 5.9 shows, analogously to Fig. 5.8, non-prompt J/ψ dimuon mass distributions, for the two p_{T} bins mentioned in the legends. Given the very large number of J/ψ events, the measured mass distribution in the peak region has almost zero relative uncertainty, so that a simple fit model such as the one chosen for this analysis is likely to result in pulls[1] that show systematic trends (in addition to the expected statistical fluctuations). Increasing the complexity of the fit function, for example by adding CB functions to the signal shape, would reduce the pulls and apparently improve agreement, but in this case it is preferred to keep the function as simple as possible (within reasonable agreement with the data) since, as will be described in the following, the fitted signal function is not used to evaluate the background fraction, and so a “perfect” description of the peak shape is not necessary. In any case, the fit model we have used provides a reasonable description of the measured distribution: the relative differences between the data and the fit function are at the few percent level, as shown by the lower panels of Fig. 5.9.

The most important shape parameters obtained from the dimuon mass fits are the amplitude and inverse slope of the mass-continuum exponential function, which are thus left free in each p_{T} bin. These are the only fit parameters required to determine the fraction $f^{\mathrm{NPS}}_{\mathrm{B_{NP}}}$, which is computed by integrating the fitted background function (in each p_{T} bin) in the signal mass window (NPS) and then dividing the result by the total number of events counted in that region. Figure 5.10 shows the obtained values, as

[1] Pulls are computed as the difference between the measured and fitted yields, divided by the statistical uncertainty of the data point.

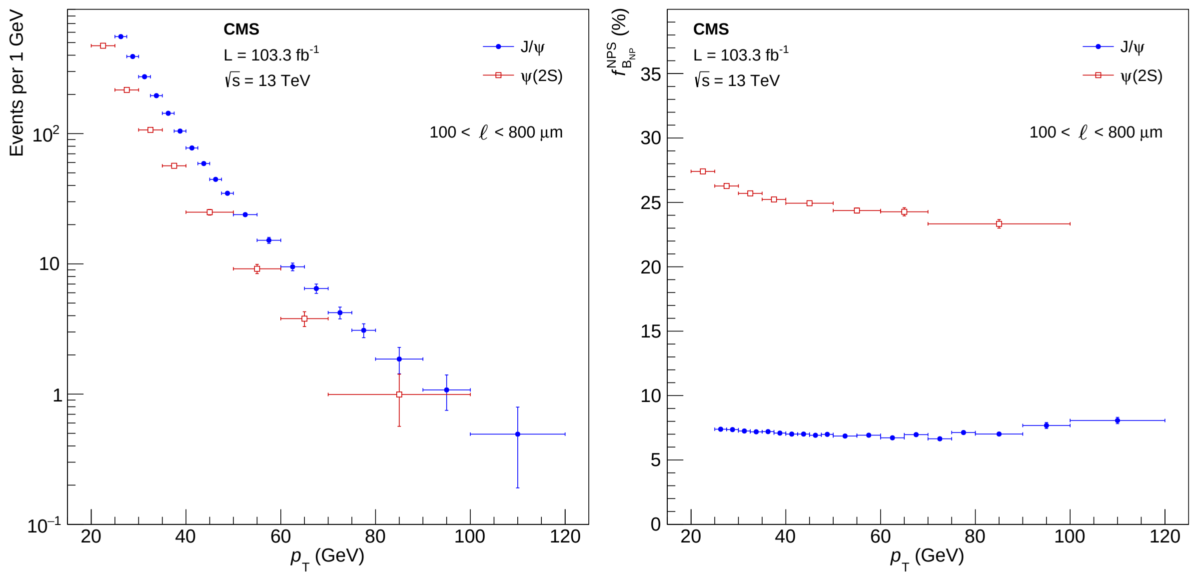

Figure 5.10: Variation with p_T of the integral of the fitted mass-continuum exponential function in the signal mass window (left) and of the fraction of events in the NPS region due to mass-continuum muon pairs (right), for the non-prompt J/ψ and $\psi(2\mathrm{S})$ events.

a function of p_T, for the integral of the fitted background function and $f^{\mathrm{NPS}}_{\mathrm{B_{NP}}}$ in the left and right panels, respectively.

5.2.2 Background fractions in the prompt charmonia signal regions

The fractions of mass-continuum muon pairs in the prompt signal windows, $f^{\mathrm{PRS}}_{\mathrm{B_{PR}}}$, for both the J/ψ and $\psi(2\mathrm{S})$ cases, are determined by fitting the dimuon mass distributions in the PR region ($|\ell| < 50\,\mu$m) using the same fit procedure and fit models as for the non-prompt cases; the only exception is that, for the J/ψ, the two CB functions have common μ parameters in this case, similarly to the $\psi(2\mathrm{S})$. Figures 5.11 and 5.12 show the dimuon mass distributions measured for the PR $\psi(2\mathrm{S})$ and J/ψ events, respectively, in the p_T bins already used in Figs. 5.8 and 5.9.

Figure 5.13 shows the variation with p_T of the integral of the fitted background function, in the left panel, and of the background fraction $f^{\mathrm{PRS}}_{\mathrm{B_{PR}}}$, in the right panel.

The other source of background contributing to the PRS region corresponds to charmonia produced in decays of short-lived B mesons. The fractions of events in the PRS windows due to those non-prompt charmonia, $f^{\mathrm{PRS}}_{\psi_\mathrm{B}}$, are obtained by fitting the lifetime distributions of the dimuons in the J/ψ or $\psi(2\mathrm{S})$ signal mass windows. It is important here to take into consideration that not all non-prompt contamination in the PRS region corresponds to charmonia: the non-prompt continuum muon pairs, already contributing to $f^{\mathrm{PRS}}_{\mathrm{B_{PR}}}$, must be accounted for separately.

The 19 J/ψ or 8 $\psi(2\mathrm{S})$ dimuon lifetime distributions (one per p_T bin) are fitted simultaneously, in the range from -50 to +500 μm, selecting the events with dimuon mass in the mass signal windows. As the aim of the fits is to obtain a model of the NP contribution in the PR window, the fit window does not need to be extended up to +800 μm. The fit model is composed of three contributions.

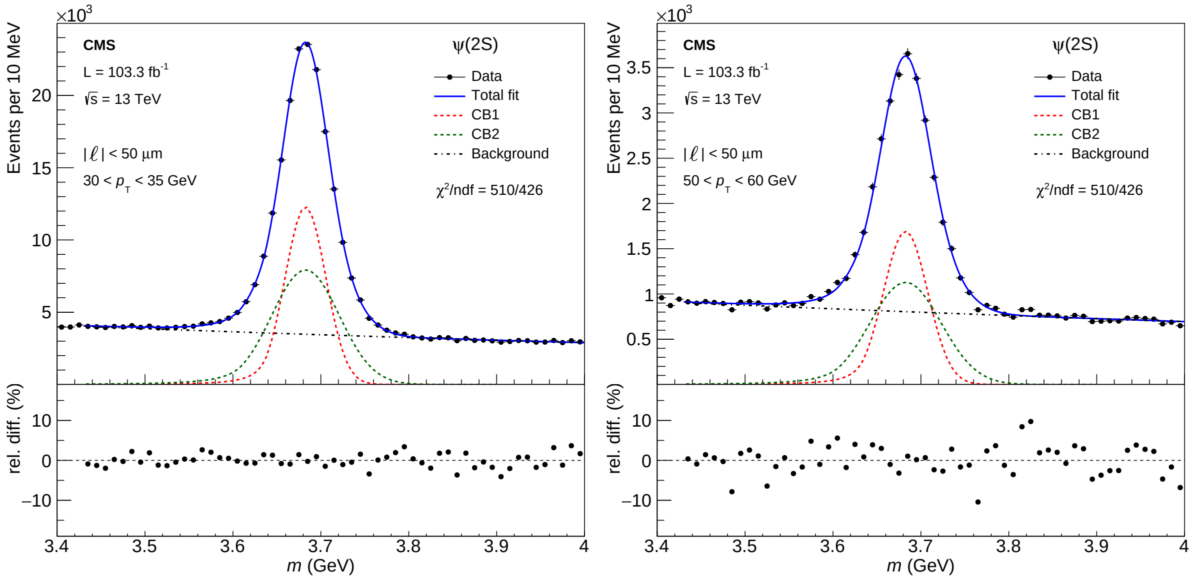

Figure 5.11: Dimuon mass distributions measured for the prompt $\psi(2S)$ in the two p_T bins mentioned in the legends. The total fit function (blue line), the two CB functions (red and green), and the background continuum (black) are also shown. The lower panels show the corresponding relative difference distributions.

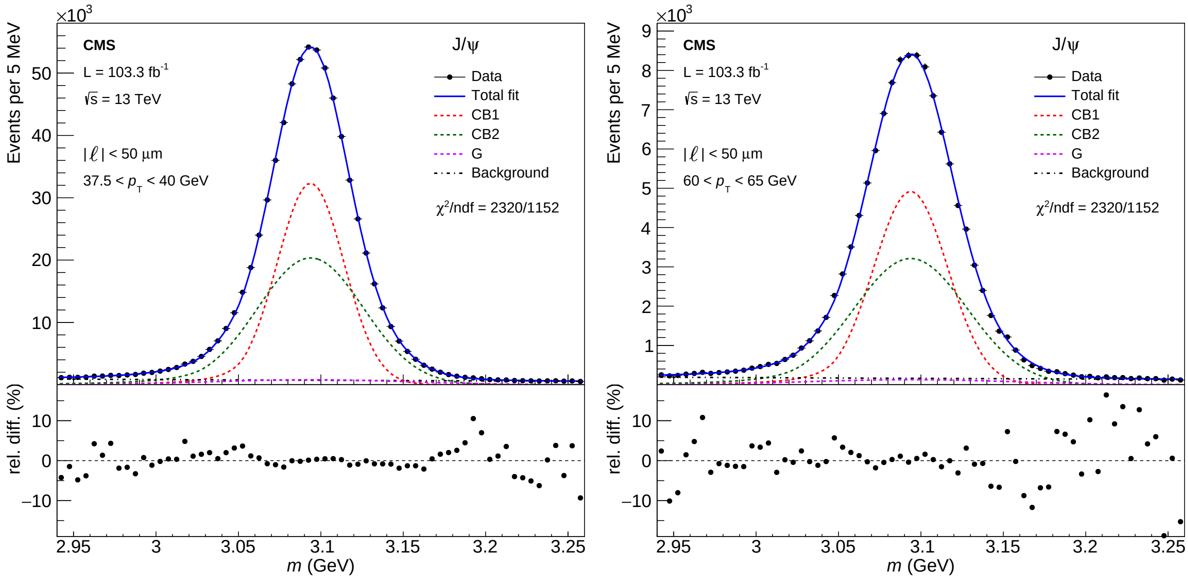

Figure 5.12: Dimuon mass distributions measured for the prompt J/ψ in the two p_T bins mentioned in the legends. The total fit function (blue line), the two CB functions (red and green), the Gaussian function (magenta), and the background continuum (black) are also shown. The lower panels show the corresponding relative difference distributions.

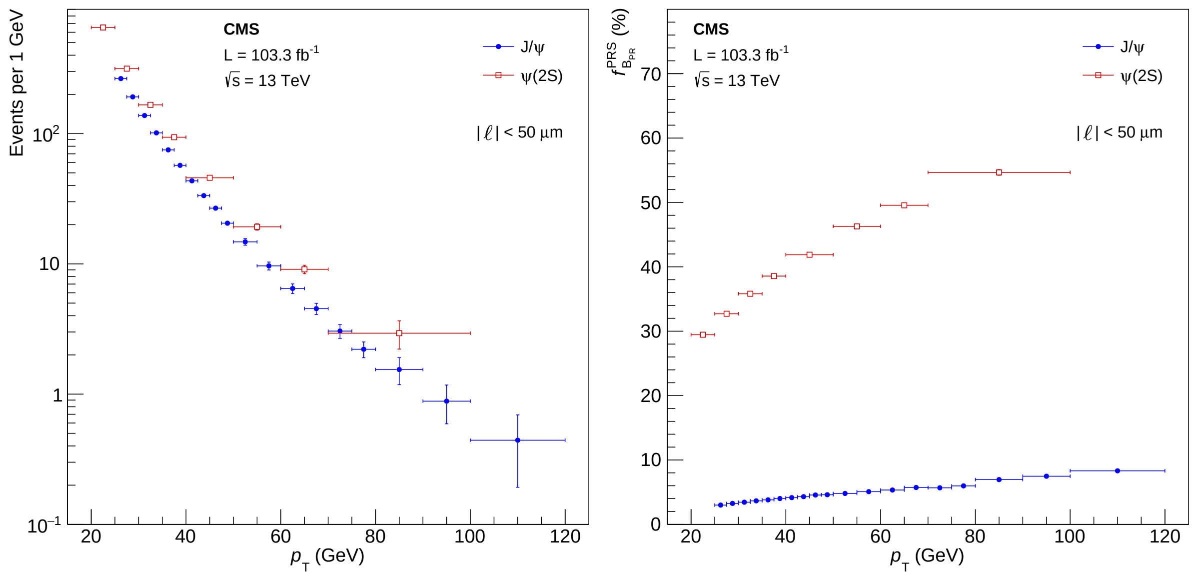

Figure 5.13: Variation with p_{T} of the integral of the fitted mass-continuum exponential function in the signal mass window (left) and of the fraction of events in the PRS region due to mass-continuum muon pairs (right), for the prompt J/ψ and $\psi(2\mathrm{S})$ events.

First there is the prompt term, represented by the lifetime resolution function, parametrised by the sum of three Gaussian functions with a common mean and independent widths, defined such that $\sigma_{G3} > \sigma_{G2} > \sigma_{G1}$:

$$L_{\mathrm{PR}} \equiv L_{\mathrm{res}} = f_{G1} \cdot G_1(\ell|\mu, \sigma_{G1}) + f_{G2} \cdot G_2(\ell|\mu, \sigma_{G2}) + (1 - f_{G1} - f_{G2}) \cdot G_3(\ell|\mu, \sigma_{G3}) \, . \tag{5.9}$$

Studies of MC event samples show that the superposition of three Gaussian functions provides a good description of the prompt lifetime distributions. They also show that several parameter constraints can be imposed: the relative contributions of the three terms, their mean value μ, as well as the ratios σ_{G2}/σ_{G1} and σ_{G3}/σ_{G1}, are made independent of p_{T}, so that the p_{T}-dependence of the lifetime resolution is fully described by the σ_{G1} parameter, which decreases as p_{T} increases, as shown in Fig. 5.14. The narrowest Gaussian, G_1, is the dominant term and the other two can be seen as successive corrections. In the J/ψ case, G_1 contributes 53.3% of the signal, G_2 contributes 42.7%, and G_3 the remaining 4%. In the $\psi(2\mathrm{S})$ case, the corresponding values are 70.8%, 28.0%, and 1.2%. The σ_{G2}/σ_{G1} and σ_{G3}/σ_{G1} ratios are 1.57 ± 0.01 and 3.16 ± 0.09 for the J/ψ distributions, respectively, while the corresponding $\psi(2\mathrm{S})$ values are 1.91 ± 0.01 and 9.3 ± 0.3.

The second term represents the contribution of ψ mesons from B decays and is parametrised by a decreasing exponential (for $\ell > 0$) convolved with the resolution function,

$$L_{\psi_{\mathrm{B}}} = [\exp(-\ell/t_{\psi_{\mathrm{B}}}) \cdot \mathcal{H}(\ell)] \otimes L_{\mathrm{res}}(\ell|\mu, \sigma_{G1}, \sigma_{G2}, \sigma_{G3}), \tag{5.10}$$

where $\mathcal{H}$ is the Heaviside step function. In the fits, the amplitude and inverse slope of this exponential function are left free in each p_{T} bin.

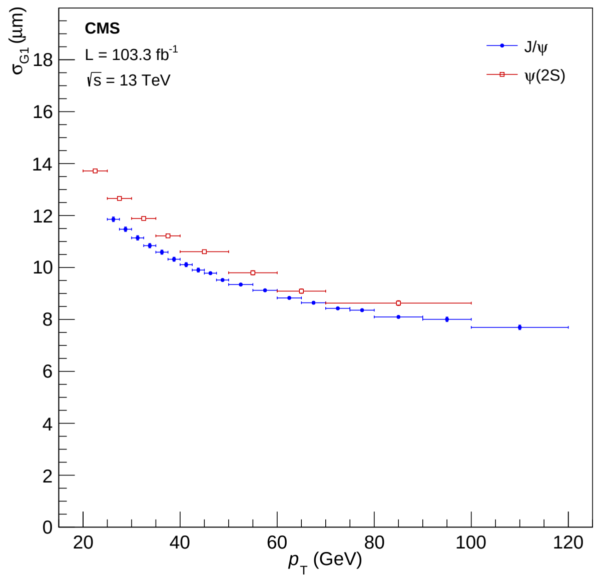

Figure 5.14: Variation with $p_{\rm T}$ of the width of the dominant Gaussian function parametrising the lifetime resolution function, G_1, for the J/ψ and $\psi(2\mathrm{S})$ events.

Finally, there is the term representing the non-prompt mass-continuum muon pairs, parametrised by one (for the J/ψ) or two (for the $\psi(2\mathrm{S})$) decreasing exponentials, also for $\ell > 0$ and convolved with the resolution function, similarly to $L_{\psi_{\rm B}}$. This term is fully fixed in the fit, with shape and normalization parameters determined by interpolating to the signal mass window the lifetime distributions measured in the mass sidebands (using the $100 < \ell < 500\,\mu$m range).

Beginning with the case of the $\psi(2\mathrm{S})$ analysis, the highly populated and wide mass sidebands allow for a study of the variations of the lifetime distribution with mass using four mass bins in each of the two sidebands. As shown in Fig. 5.15, the shapes of the mass-sideband $\psi(2\mathrm{S})$ lifetime distributions are essentially independent of $p_{\rm T}$. Therefore, it can be assumed that the function representing the lifetime distribution of this background term is similarly independent of $p_{\rm T}$. Fits are thus performed for the $p_{\rm T}$-integrated lifetime distributions, in the $100 < \ell < 500\,\mu$m range, in eight mass sideband bins: four 30 MeV bins between 3.4 and 3.52 GeV plus four 45 MeV bins between 3.82 and 4.0 GeV.

The 8 lifetime distributions are well described by the sum of two exponential functions with slopes that are independent of the dimuon mass,

$$L^{\rm 2exp}_{\rm NP} = N^{\rm Bg}_{\rm NP}\left[f_1 \cdot \exp\Big(-\ell/t^{\rm Bg}_{\rm NP_1}\Big) + (1-f_1)\cdot \exp\Big(-\ell/t^{\rm Bg}_{\rm NP_2}\Big)\right] . \tag{5.11}$$

Leaving free the relative weight of the two exponential functions, f_1, we see that it changes linearly with the dimuon mass, so the fits are redone imposing this condition, to minimize statistical fluctuations.

Figure 5.16 illustrates the fit quality for two mass bins, mentioned in the legends, one from each sideband. The measured lifetime distributions are well described by the fit, with no systematic trends in the pull distributions.

Having found the mass-dependent shape parameters of the lifetime function, from the $p_{\rm T}$-integrated distributions, they can now be fixed in a fit of the lifetime distributions for each $p_{\rm T}$ bin, to obtain the

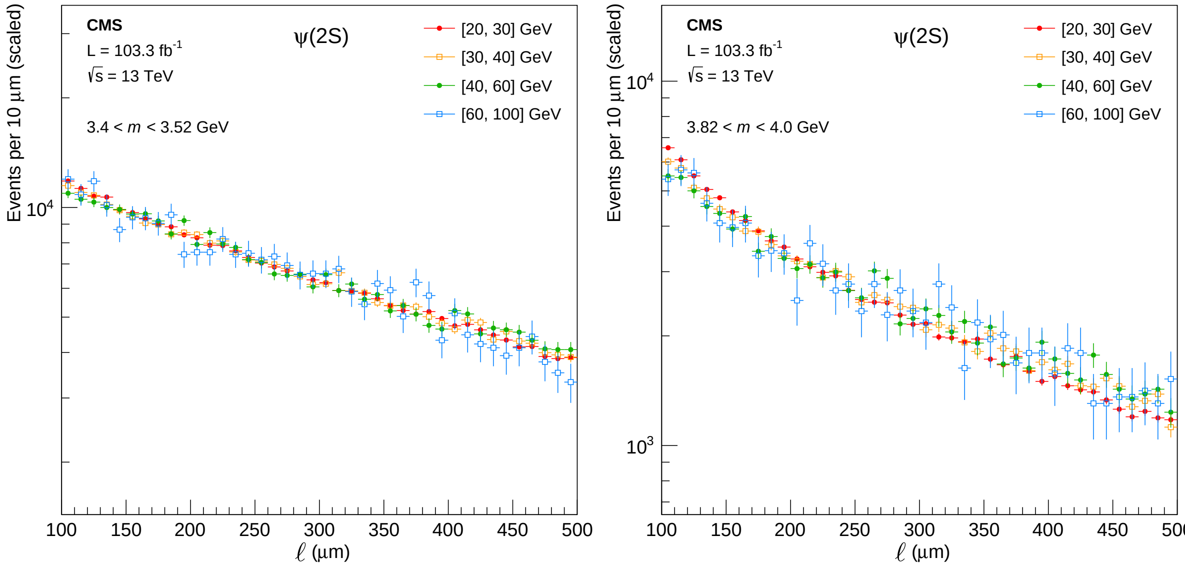

Figure 5.15: Dimuon lifetime distributions measured for the $\psi(2\mathrm{S})$ events in the left (left) and right (right) mass sidebands, for the p_{T} ranges mentioned in the legends. The distributions of the three highest p_{T} ranges were scaled so that their integrals are identical to that of the lowest p_{T} range.

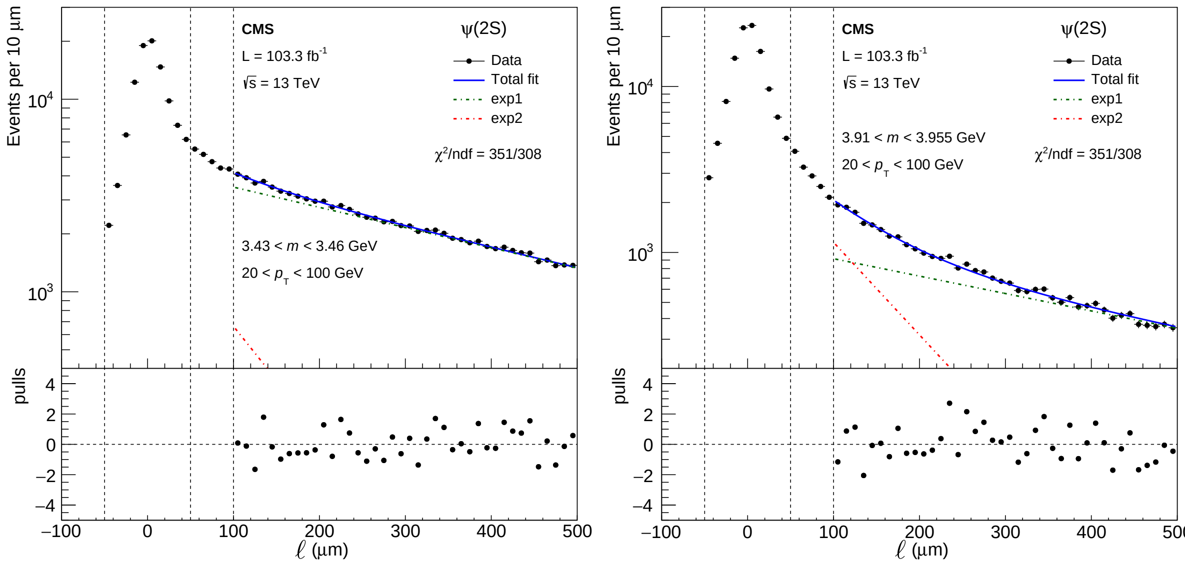

Figure 5.16: Measured LSB (left) and RSB (right) p_{T}-integrated $\psi(2\mathrm{S})$ lifetime distributions for the two mass bins mentioned in the legends; the fitted functions are also shown. The lower panels show the corresponding pull distributions.

normalization parameter, $N_{\mathrm{NP}}^{\mathrm{Bg}}$, as a function of dimuon mass and p_{T}. Not surprisingly, this parameter shows an exponential decrease with dimuon mass. Redoing the fits with this additional constraint, to minimize statistical fluctuations, $N_{\mathrm{NP}}^{\mathrm{Bg}}$ is obtained as an exponential function of dimuon mass, for each p_{T} bin. Figure 5.17 illustrates the fit quality, for two p_{T} bins.

Since all the parameters of the eight SB lifetime functions, including the normalizations, have been determined as functions of the dimuon mass, it is easy to obtain, by simple interpolation, the function that describes the lifetime distribution of the (non-prompt) mass-continuum dimuons in the signal mass window.

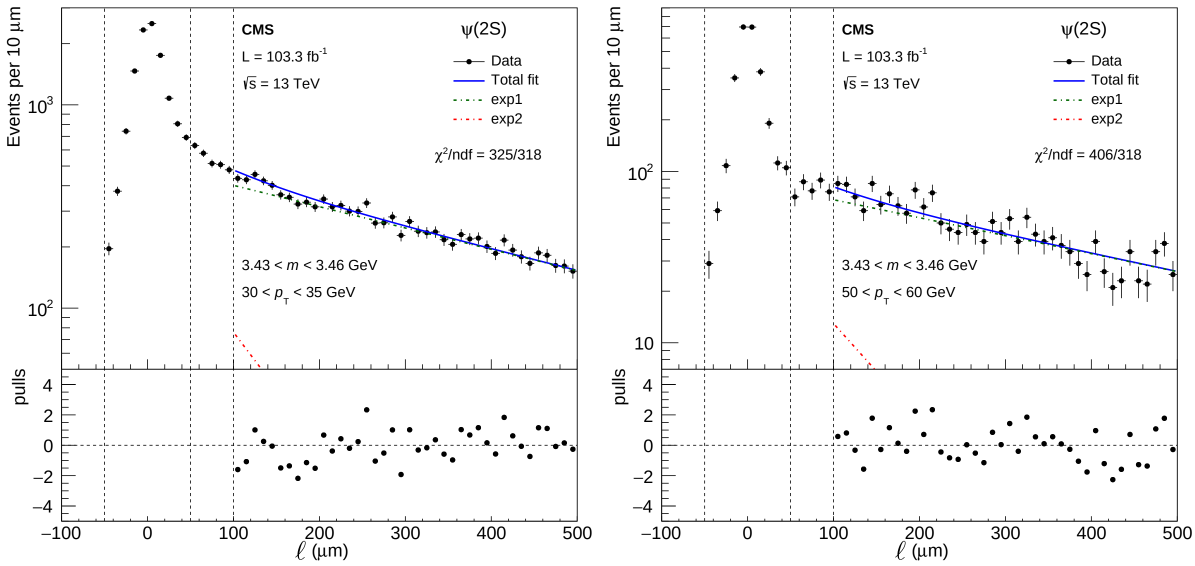

Figure 5.17: $\psi(2\mathrm{S})$ lifetime distributions measured in the 3.43–3.46 GeV sideband mass range for the two p_T bins mentioned in the legends; the fitted functions are also shown. The lower panels show the corresponding pull distributions.

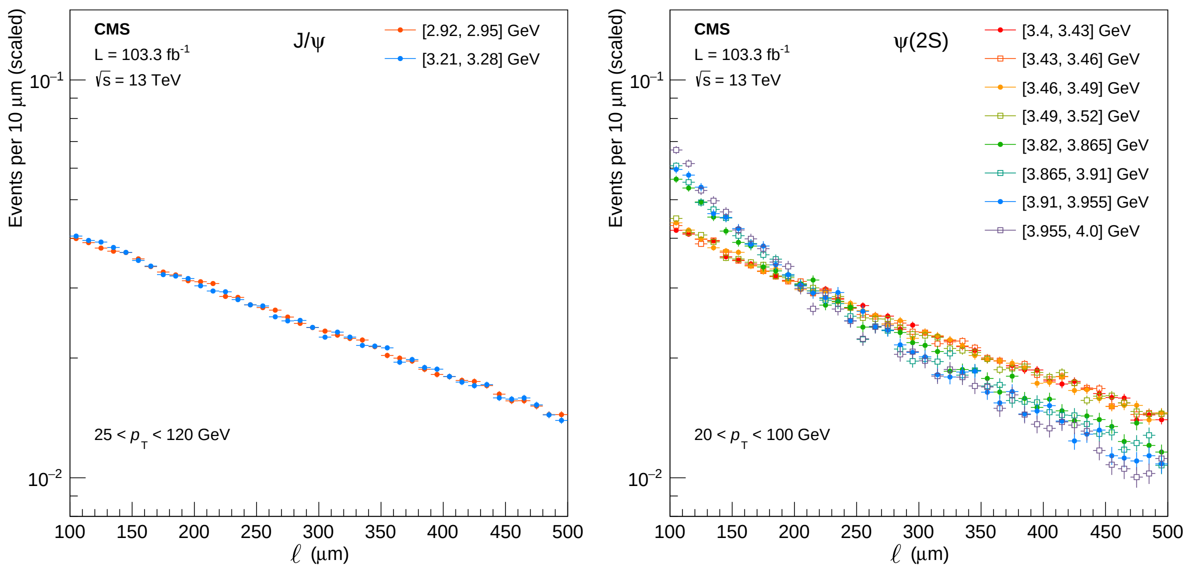

Figure 5.18: Dimuon lifetime distributions, integrated in p_T, measured for the sideband mass ranges mentioned in the legends, in the J/ψ (left) and $\psi(2\mathrm{S})$ (right) cases.

In the case of the J/ψ analysis, the interpolation to the signal window is straightforward because, as shown in the left panel of Fig. 5.18, the two J/ψ mass sidebands have identical lifetime distributions, unlike the $\psi(2\mathrm{S})$ case, where a variation with mass is clearly seen in the right panel of the same figure.

The $100 < \ell < 500\,\mu$m range of the J/ψ lifetime distributions is fitted in two sideband mass intervals, in this case using a single exponential function with a mass-independent slope,

$$L_\mathrm{NP}^\mathrm{1exp} = N_\mathrm{NP}^\mathrm{Bg} \exp\left(-\ell/t_\mathrm{NP}^\mathrm{Bg}\right) . \tag{5.12}$$

The quality of the p_T-integrated fits can be appreciated in Fig. 5.19. The subsequent fits, performed

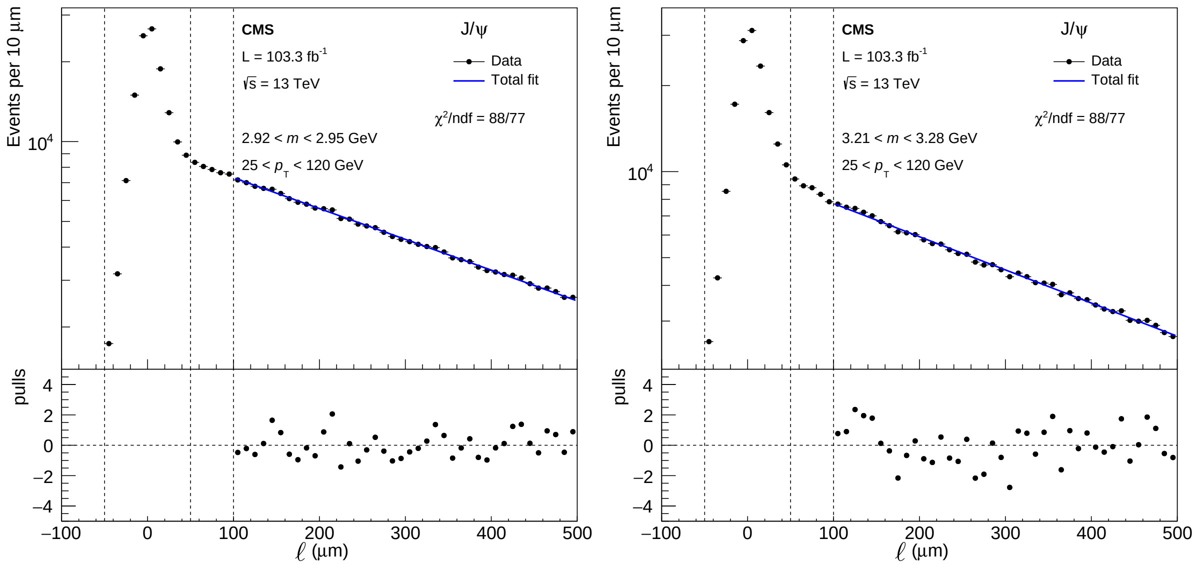

Figure 5.19: Measured LSB (left) and RSB (right) p_{T}-integrated J/ψ lifetime distributions; the fitted functions are also shown. The lower panels show the corresponding pull distributions.

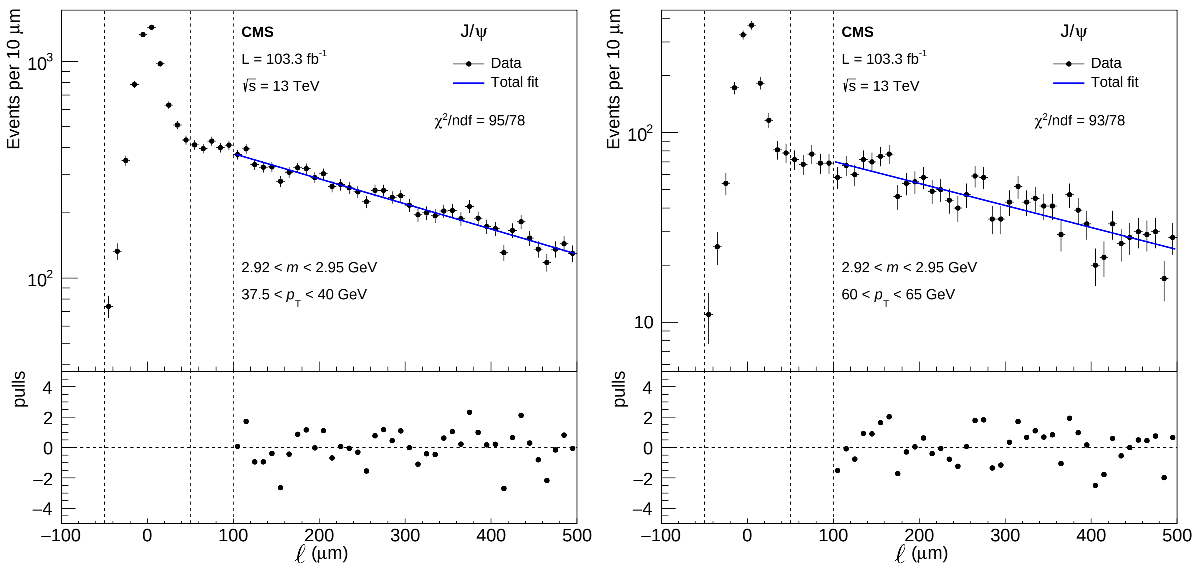

Figure 5.20: J/ψ lifetime distributions measured in the LSB mass range for the two p_{T} bins mentioned in the legends; the fitted functions are also shown. The lower panels show the corresponding pull distributions.

in each p_{T} bin to determine the p_{T}-dependence of $N_{\mathrm{NP}}^{\mathrm{Bg}}$, are illustrated in Fig. 5.20 for the two p_{T} bins mentioned in the legends.

Figure 5.21 shows, for illustration, the dimuon lifetime distributions measured in representative p_{T} bins for both charmonia, in the mass signal regions. The three contributions to the fit are shown separately: the prompt term, represented by the solid green line; the ψ mesons from B decays, represented by the dashed red line; and the non-prompt mass-continuum muon pairs, represented by the dashed grey line. The measured distributions are well described by the fit model, given the reasonable pull distributions.

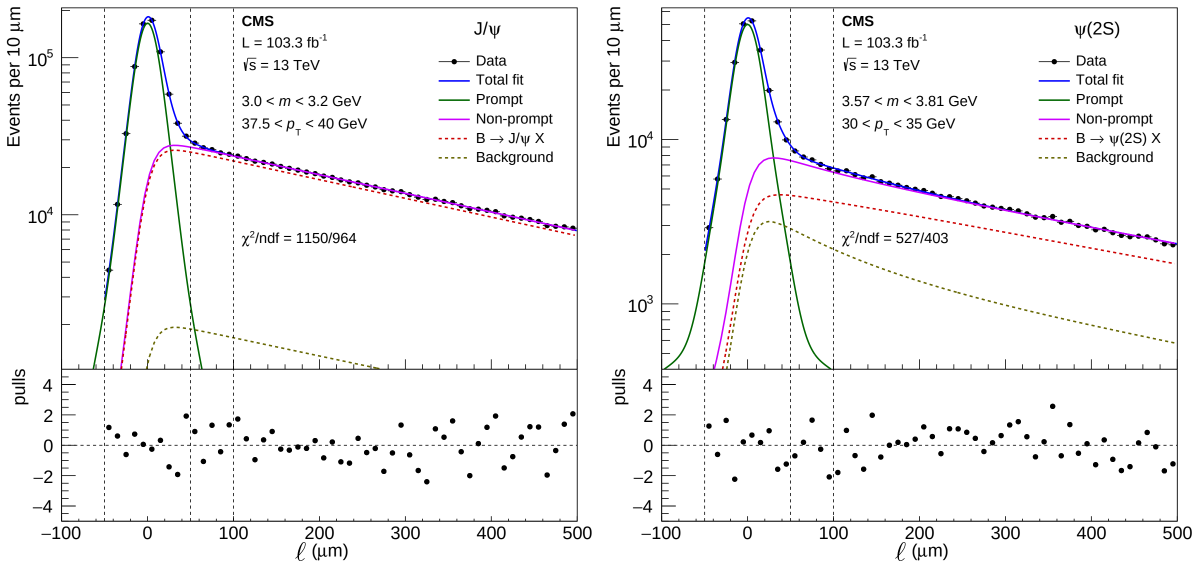

Figure 5.21: Dimuon lifetime distributions measured for the J/ψ (left) and $\psi(2\mathrm{S})$ (right) cases, in their mass signal windows, in the p_{T} bins mentioned in the legends. The vertical dashed lines mark the limits of the PR and NP ranges. The total fit function, as well as the several contributions, are also shown.

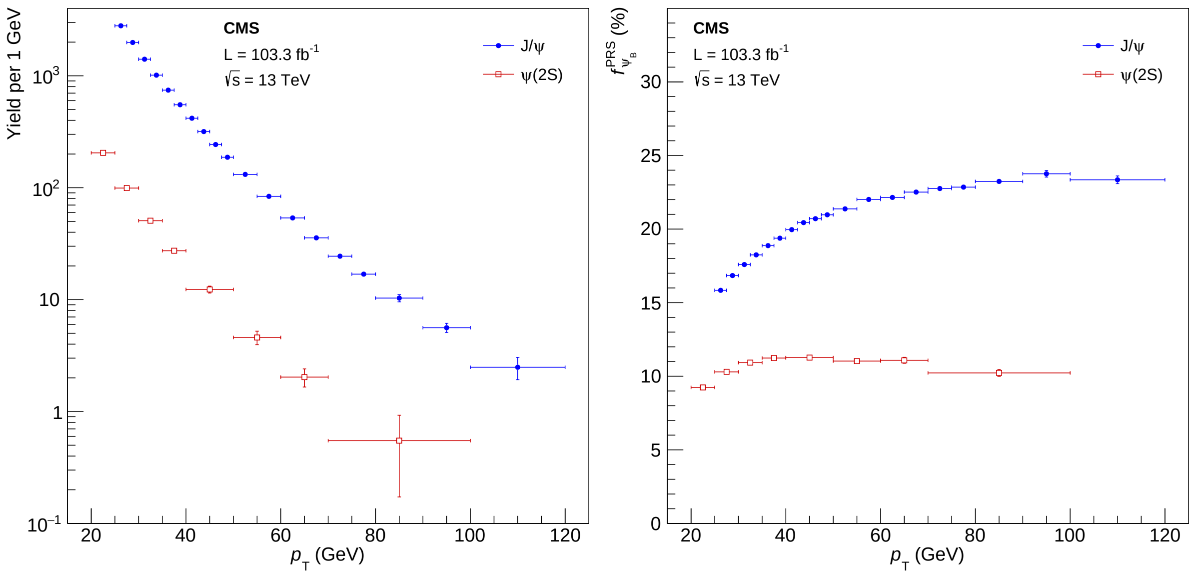

Figure 5.22: Variation with p_{T} of the integral of the fitted non-prompt ψ exponential function in the PRS region (left) and of the corresponding fraction of events (right).

The $f_{\psi_{\mathrm{B}}}^{\mathrm{PRS}}$ fractions are evaluated (in each p_{T} bin) by integrating the fitted ψ_{B} term in the prompt window and dividing the result by the total number of events counted in that region. The integrated values and corresponding fractions are shown in Fig. 5.22, for the J/ψ and $\psi(2\mathrm{S})$ cases. As expected from previous analyses, the J/ψ "non-prompt fraction" increases with p_{T} and then saturates.

5.3 Polarization measurement

The previous section described the procedure to get the fractions of background events, both from the mass-continuum dimuons in the NPS and PRS regions, $f_{\mathrm{B_{NP}}}^{\mathrm{NPS}}$ and $f_{\mathrm{B_{PR}}}^{\mathrm{PRS}}$, and from the charmonia produced in B decays that populate the PRS region, $f_{\psi_{\mathrm{B}}}^{\mathrm{PRS}}$, for both states. The results, as a function of p_{T}, have been presented in the right panels of Figs. 5.10, 5.13, and 5.22.

As shown in Eqs. 5.4 and 5.5, in addition to these fractions, the measurement of the physically-relevant $\psi_{\mathrm{B}}(|\cos\vartheta|, p_{\mathrm{T}})$ and $\psi_{\mathrm{P}}(|\cos\vartheta|, p_{\mathrm{T}})$ 2D distributions also implies knowing the $(|\cos\vartheta|, p_{\mathrm{T}})$ 2D distributions of the mass-continuum background terms, $B_{\mathrm{NP}}(|\cos\vartheta|, p_{\mathrm{T}})$ and $B_{\mathrm{PR}}(|\cos\vartheta|, p_{\mathrm{T}})$.

These NP and PR mass-continuum background terms are obtained by interpolating into the signal mass region, for each p_{T} bin, the $|\cos\vartheta|$ distributions of the mass sidebands. The interpolation is done as a weighted average of the two mass sideband distributions,

$$f_L(p_{\mathrm{T}}) \cdot \text{LSB}\,(|\cos\vartheta|, p_{\mathrm{T}}) + (1 - f_L(p_{\mathrm{T}})) \cdot \text{RSB}\,(|\cos\vartheta|, p_{\mathrm{T}})\,, \tag{5.13}$$

where

$$f_L = \frac{M_\psi - \langle m_{\mathrm{LSB}} \rangle}{\langle m_{\mathrm{RSB}} \rangle - \langle m_{\mathrm{LSB}} \rangle}\,, \tag{5.14}$$

with M_ψ being the mid-point of the signal mass windows (3.0–3.2 and 3.57–3.81 GeV for the J/ψ or $\psi(2\mathrm{S})$ cases, respectively), and $\langle m_{\mathrm{LSB,RSB}} \rangle$ obtained from L_{Bg}, defined in Eq. 5.7, through

$$\langle m_{\mathrm{LSB,RSB}} \rangle = \frac{\int_{m_{\min}}^{m_{\max}} m \cdot L_{\mathrm{Bg}}(m)\,\mathrm{d}m}{\int_{m_{\min}}^{m_{\max}} L_{\mathrm{Bg}}(m)\,\mathrm{d}m}\,. \tag{5.15}$$

The weight f_L is found to be essentially independent of p_{T} and only slightly above 50%, for both states.

Figure 5.23 shows the LSB and RSB $|\cos\vartheta|$ distributions, as well as their weighted average, for the PR J/ψ (top panels) and NP $\psi(2\mathrm{S})$ (bottom panels) samples, in two p_{T} bins.

With these distributions, all required contributions have been determined, and it is possible to perform the background subtraction that gives, from the PRS and NPS samples, the ψ_{B} and ψ_{P} $(|\cos\vartheta|, p_{\mathrm{T}})$ distributions. From these, the prompt and non-prompt $\lambda_\vartheta(p_{\mathrm{T}})$ values can then be determined.

Figure 5.24 illustrates the background subtraction procedure. The top panels show, for both ψ states, the $|\cos\vartheta|$ distributions of the NPS events (in black, before background subtraction) and of the mass-continuum background events (in green, scaled by its fraction), as well as their difference, the $\mathrm{B} \to \psi$ distribution ("non-prompt J/ψ" and "non-prompt $\psi(2\mathrm{S})$", in red), for one illustrative p_{T} bin.

The bottom panels of Fig. 5.24 show the $|\cos\vartheta|$ distributions of the several prompt terms. These are almost identical to the non-prompt case aside from an additional background contribution to be subtracted: the events in the PRS window that are actually the result of B meson decays, even though they have small ℓ values. The events in the signal mass regions (PRS) are shown in violet and the two background sources, scaled by their corresponding fractions, are shown in green (mass-continuum dimuons) and in red ($\mathrm{B} \to \mathrm{J}/\psi$ and $\mathrm{B} \to \psi(2\mathrm{S})$ contributions). Subtracting the two backgrounds from the

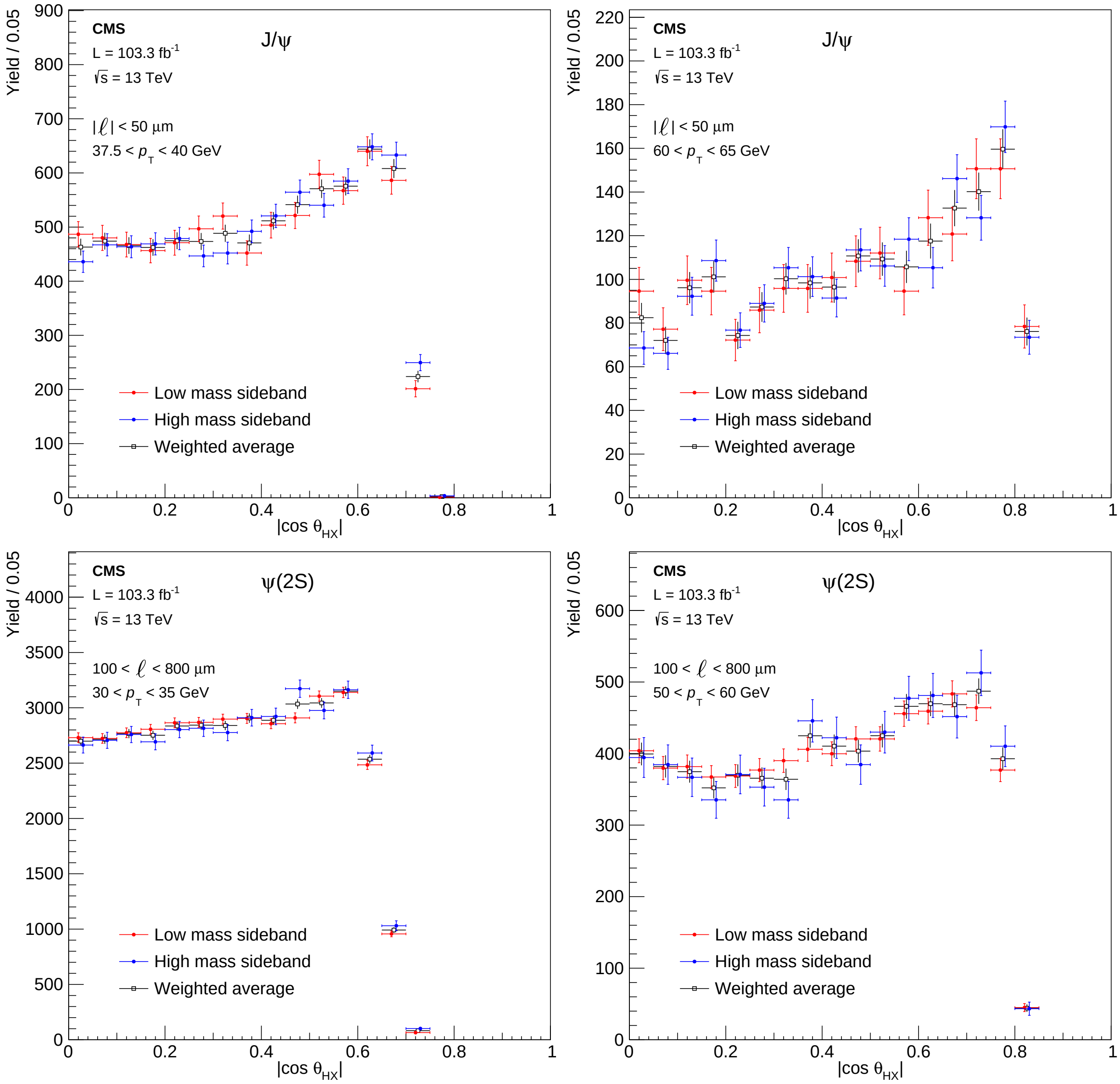

Figure 5.23: LSB (red), RSB (blue), and interpolated (black) $|\cos\vartheta|$ distributions, for two p_{T} bins (left and right) in the PR J/ψ (top) and NP $\psi(2\mathrm{S})$ (bottom) samples.

PRS points, the prompt J/ψ and $\psi(2\mathrm{S})$ signals are obtained, shown in blue.

Figure 5.25 shows the ratios between the measured and the simulated $|\cos\vartheta|$ distributions, for the prompt and non-prompt J/ψ (left) and $\psi(2\mathrm{S})$ (right), obtained after subtracting the backgrounds. Fitting these distributions with Eq. 5.3 gives the corresponding λ_ϑ values, for the given p_{T} bin. As was mentioned in Section 5.1, the fits do not include the largest $|\cos\vartheta|$ bins, which are closest to the edge of the covered range and thus correspond to the ratio of two steeply falling distributions. More precisely, we exclude from the fit the $|\cos\vartheta|$ bins whose uncertainties exceed more than twice those of the fitted $|\cos\vartheta|$ bins.

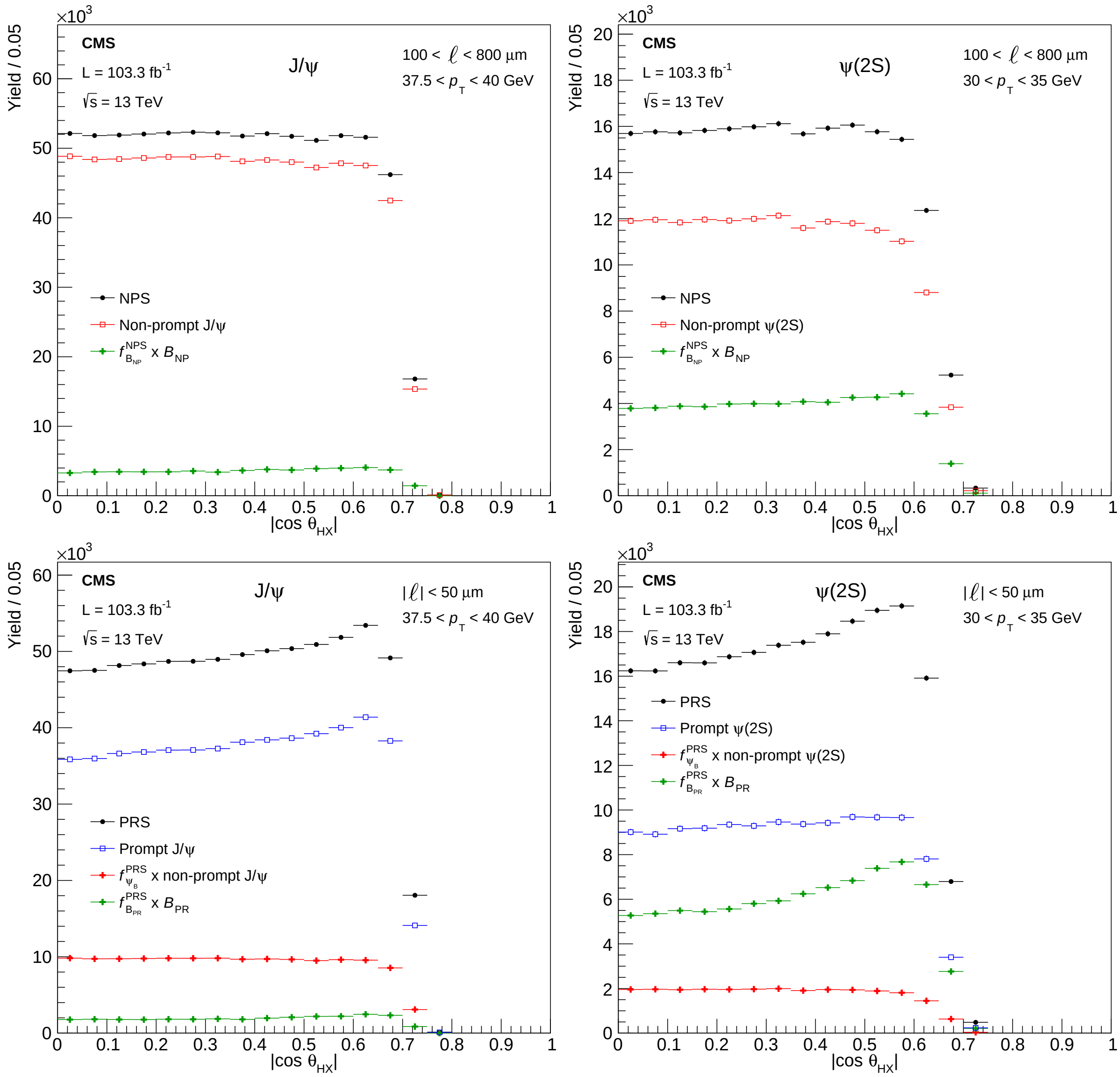

Figure 5.24: Top: $|\cos\vartheta|$ distributions of the J/ψ (left) and $\psi(2\mathrm{S})$ (right) NPS (black) and NP background (green) terms, as well as their difference, the non-prompt ψ signal (red). Bottom: $|\cos\vartheta|$ distributions of the J/ψ (left) and $\psi(2\mathrm{S})$ (right) PRS events (black), and of the two background sources (red and green), as well as their difference, the prompt ψ signal (blue).

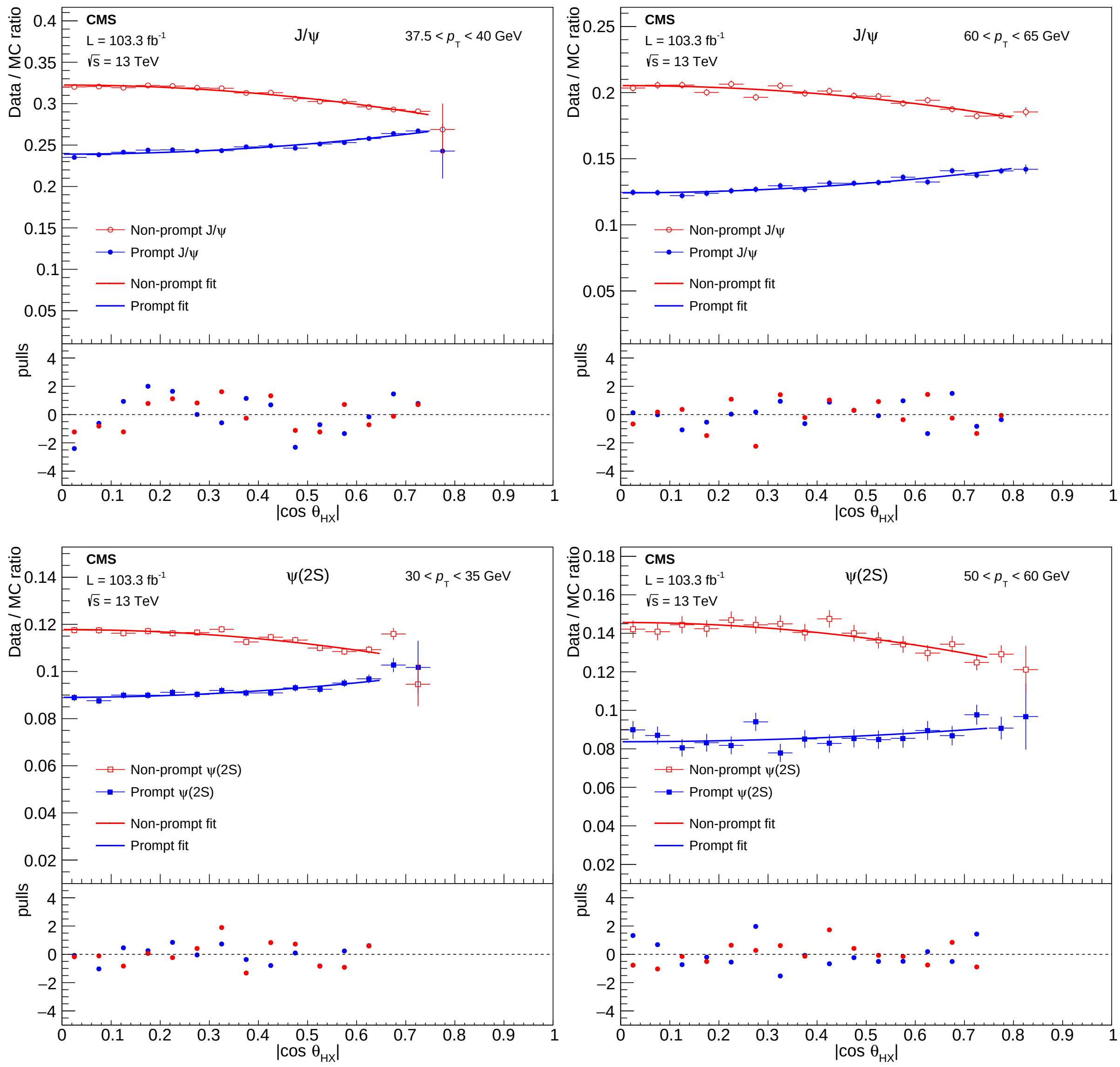

Figure 5.25: Ratios between the data and MC $|\cos\vartheta|$ distributions of the prompt and non-prompt J/ψ (top) and $\psi(2\mathrm{S})$ (bottom) for two p_{T} bins (left and right). The curves represent fits using Eq. 5.3, excluding the largest $|\cos\vartheta|$ bins. The lower panels show the corresponding pull distributions.

Repeating the same procedure for all p_{T} bins, the p_{T}-dependence of the λ_ϑ parameters is obtained, for the prompt and non-prompt J/ψ and $\psi(2\mathrm{S})$ states. The results are shown in Fig. 5.26.

The uncertainties shown in this figure are purely statistical. In order to have a full evaluation of the uncertainties associated with this measurement, it is necessary to perform systematic checks and determine the systematic uncertainties arising from the measurement procedure. This is done in the following chapter.

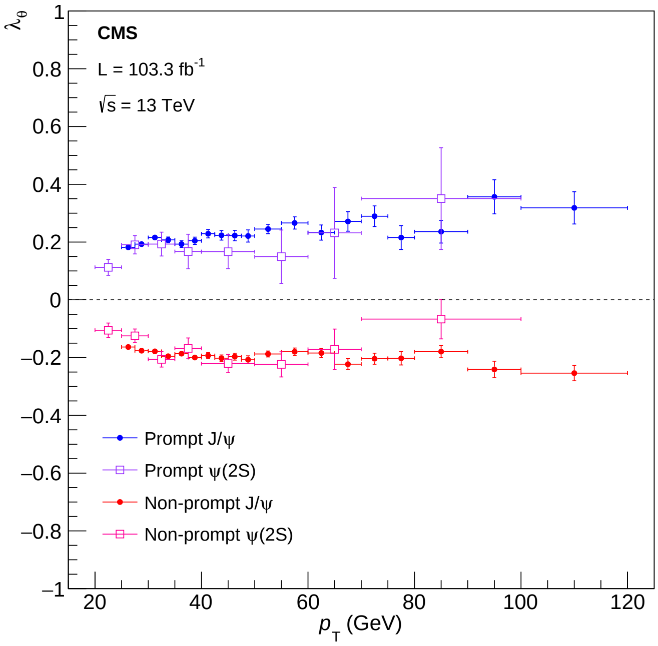

Figure 5.26: Polarization parameter λ_ϑ versus p_{T}, for the non-prompt (red or magenta) and prompt (blue or purple) J/ψ (filled circles) and $\psi(2\mathrm{S})$ (open squares) mesons.

Chapter 6

Systematic uncertainties

In this chapter, several potential sources of systematic uncertainties are studied, in order to evaluate the systematic uncertainties associated with the polarization measurements reported in the previous chapter.

The sources of systematic uncertainties considered, based on the dataset and steps of the analysis, and which will be discussed in detail in the next sections, are:

- Potential differences between the 2017 and 2018 samples;
- Single muon detection efficiencies;
- Dimuon detection efficiencies ("ρ factor");
- Fit model of the dimuon mass distributions;
- Fit model of the dimuon lifetime distributions;
- Potential residual azimuthal anisotropy in the helicity frame;
- Closure test of the polarization fit procedure.

At the end of the procedure, all contributing systematic uncertainties are summed in quadrature to determine the total systematic uncertainty associated with the measurement.

6.1 Potential differences between the 2017 and 2018 samples

To study the impact of possible differences between the 2017 and 2018 event samples, which are combined for the analysis, the polarization is measured independently in each sample. As can be seen in Fig. 6.1, for the prompt J/ψ and $\psi(2\mathrm{S})$ cases, the two measurements are compatible with each other, their difference being zero within the statistical uncertainties. Therefore, this is considered to be a "passed check" and no corresponding systematic uncertainty is attributed.

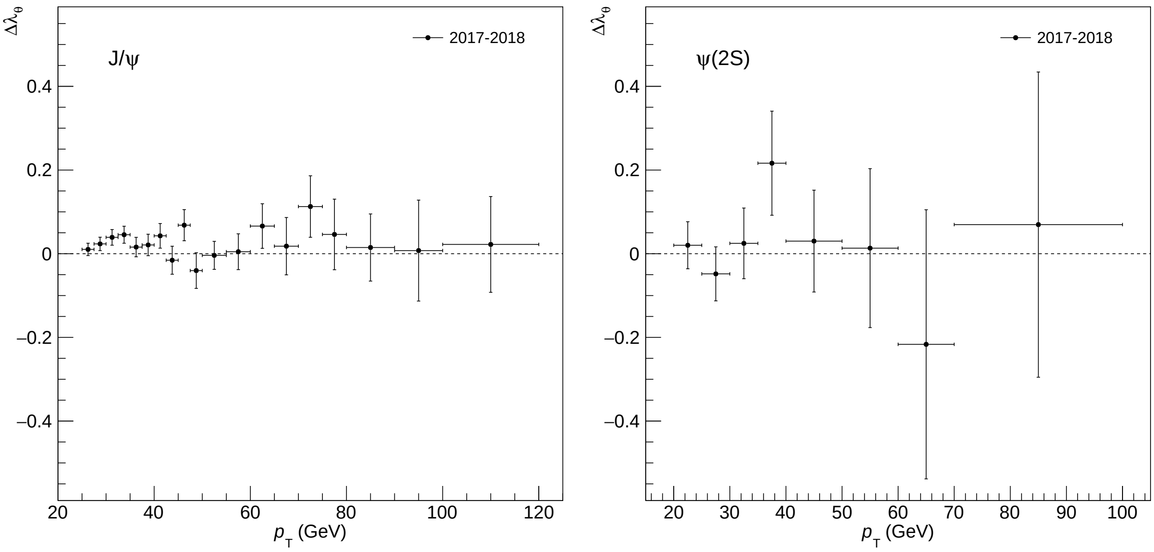

Figure 6.1: Difference between the λ_ϑ parameters measured with the 2017 data sample and those measured with the 2018 sample, for the prompt J/ψ (left) and $\psi(2\mathrm{S})$ (right) analyses.

6.2 Single muon detection efficiencies

As discussed in Section 4.2, the single muon p_T cut of 5.6 GeV ensures that all the selected events have muons of similar detection efficiencies, so that an inaccurate parametrization of the efficiency curve will have a negligible impact on the results. For the muons in the region $|\eta| < 0.2$, however, the "turn-on region" is not completely removed, as can be seen in Fig. 6.2.

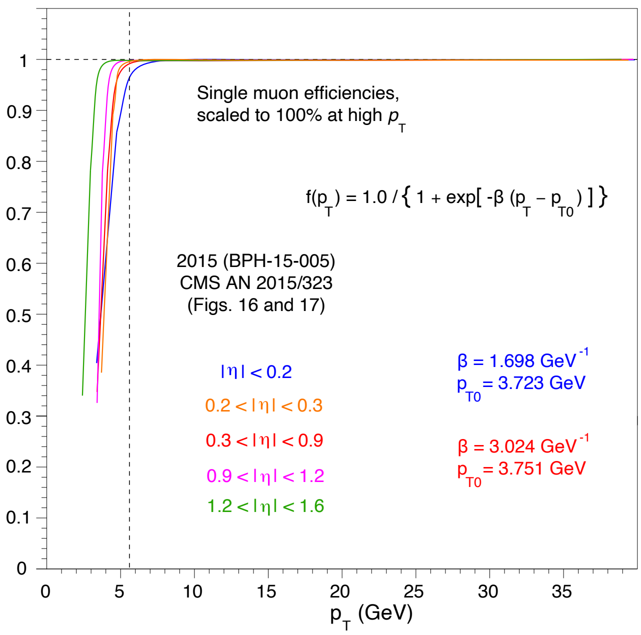

Figure 6.2: Single muon detection efficiencies for muons in several exclusive $|\eta|$ bins, as used in quarkonium production cross section measurements using the 2015 dataset [73].

Two checks are considered to evaluate if the results might be affected by a potentially wrong efficiency correction of the events in this η region.

- **Efficiency curve reweighing**:

  The single muon efficiency function for this η range is parametrised as [73],

$$f(p_{\mathrm{T}}) = \frac{1}{1+\exp\left[-\beta \cdot (p_{\mathrm{T}} - p_{\mathrm{T}0})\right]} \qquad (\beta = 1.698\,\text{GeV}^{-1},\;\; p_{\mathrm{T}0} = 3.723\,\text{GeV})$$

  where $f(p_{\mathrm{T}0}) = 0.5$, and two extreme cases are considered:

  1) There is no inefficiency at all: the MC events are thus weighed by $1/f(p_{\mathrm{T}})$ to "remove" the efficiency correction applied;

  2) The real efficiency differs from the MC efficiency by an amount equal to the efficiency itself: the MC events are weighed by $f(p_{\mathrm{T}})$, "squaring" the efficiency correction applied.

- p_{T} **cut**:

  The p_{T} cut is increased from 5.6 to 6.7 GeV for the muons with $|\eta| < 0.2$, removing their turn-on region. This more extreme check naturally leads to larger statistical uncertainties at low dimuon p_{T}.

The differences between the λ_ϑ values obtained in each of these three alternative analyses and those of the baseline analysis are shown in Fig. 6.3, for the prompt J/ψ (left) and $\psi(2\mathrm{S})$ (right) analyses, together with a grey band centred at zero that represents the statistical uncertainty of the baseline results. This band allows for a visual estimation of the impact of the different systematic sources.

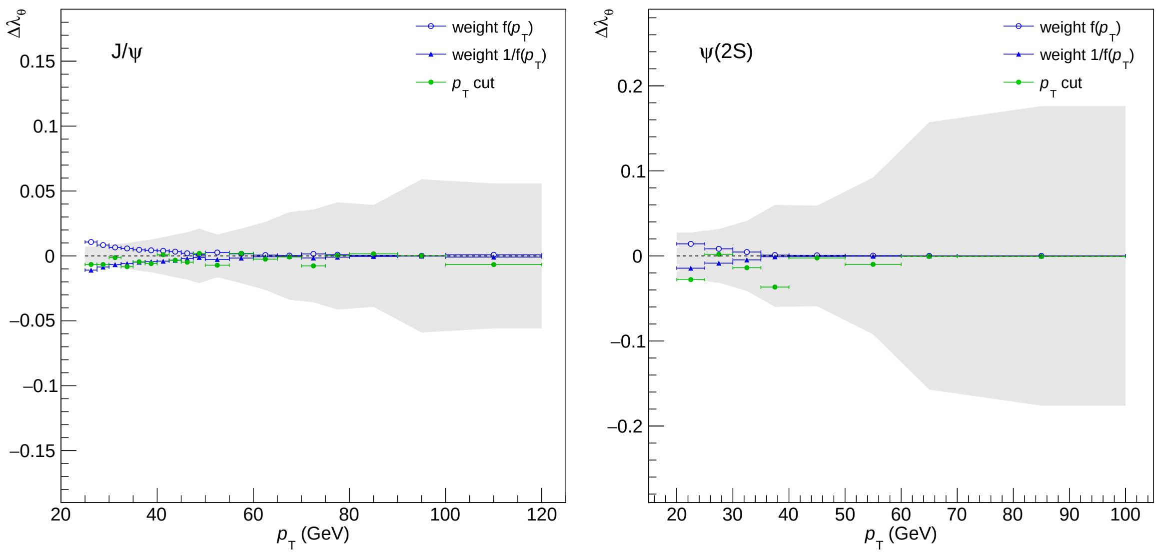

Figure 6.3: Differences between the λ_ϑ values obtained in each of the three alternative analysis scenarios and the baseline procedure, compared to the statistical uncertainties of the baseline measurement (grey band), for the prompt J/ψ (left) and $\psi(2\mathrm{S})$ (right) analyses.

A systematic uncertainty is assigned from this source, up to 50 GeV for the J/ψ and up to 40 GeV for the $\psi(2\mathrm{S})$, computed (conservatively) as the average of the absolute differences between each of the two reweighing options and the baseline values. These uncertainties are determined independently for the prompt and non-prompt cases.

Still on the topic of single muon efficiencies, the muons produced with pseudorapidity in the region $0.2 < |\eta| < 0.3$ have a lower detection efficiency because of the gap between the central muon detector wheel and its neighbours. To evaluate the possible impact of a miscorrection of this efficiency, λ_ϑ is measured after rejecting all events with a muon (or both) in this η region. As shown in Fig. 6.4 for the prompt J/ψ and $\psi(2\mathrm{S})$ analyses, the difference between the varied and baseline λ_ϑ values, vs. p_T, is randomly distributed around zero; the deviations seem to be purely statistical. Therefore, no systematic uncertainty is assigned to this source.

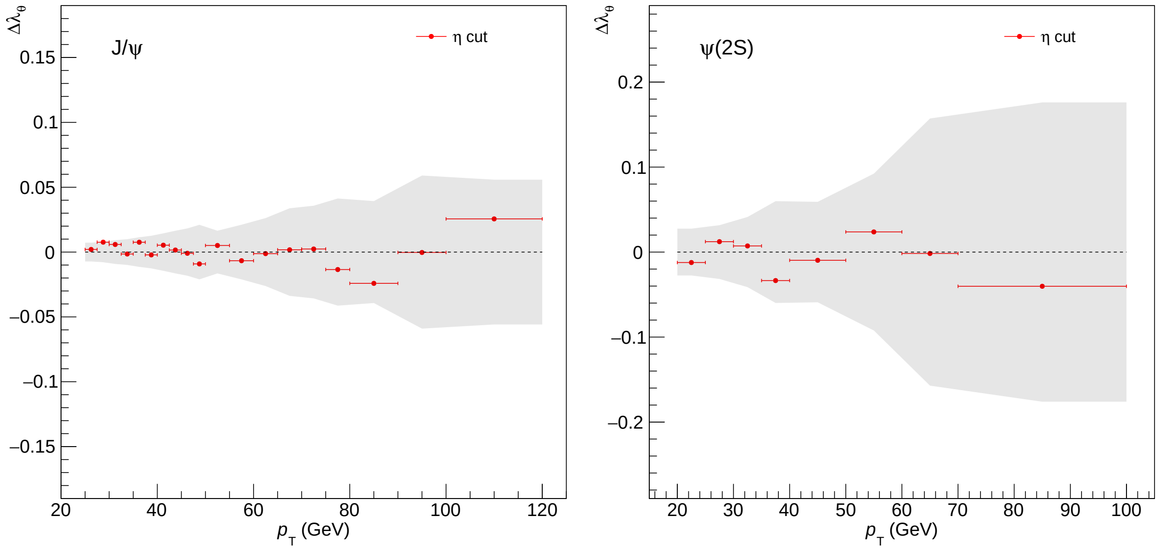

Figure 6.4: Differences between the λ_ϑ values obtained when rejecting events with at least one muon in the $0.2 < |\eta| < 0.3$ region and the baseline procedure, compared to the statistical uncertainties of the baseline measurement (grey band), for the prompt J/ψ (left) and $\psi(2\mathrm{S})$ (right) analyses.

6.3 Dimuon detection efficiencies ("ρ factor")

At high enough p_T, the two decay muons might be emitted with almost parallel trajectories and, in these conditions, they may be detected, at the trigger level, as a single muon, so that the event is not selected [71, 72]. Because of this, the dimuon efficiency $\epsilon_{\mu\mu}$ is actually smaller than the product of the two single muon efficiencies $\epsilon_{\mu,i}$, with the difference quantified by the "ρ factor", most significant at high p_T:

$$\epsilon_{\mu\mu} = \epsilon_{\mu,1} \cdot \epsilon_{\mu,2} \cdot \rho \,. \tag{6.1}$$

In principle, this effect should be faithfully reproduced by the detailed trigger emulation, included in the MC simulation, but it is important to evaluate if the obtained results could be affected by some residual differences. This is studied following the procedure used in the 7 TeV prompt charmonium polarization measurement by CMS [37].

The dimuon trigger efficiency is studied by comparing the J/ψ MC event distributions obtained after applying the trigger ("trig") to those obtained before ("reco"). The study is restricted to $p_\mathrm{T} > 50$ GeV events, where the effects are more visible. As can be seen in Fig. 6.5, the trig/reco ratio of the $\Delta\phi$ vs.

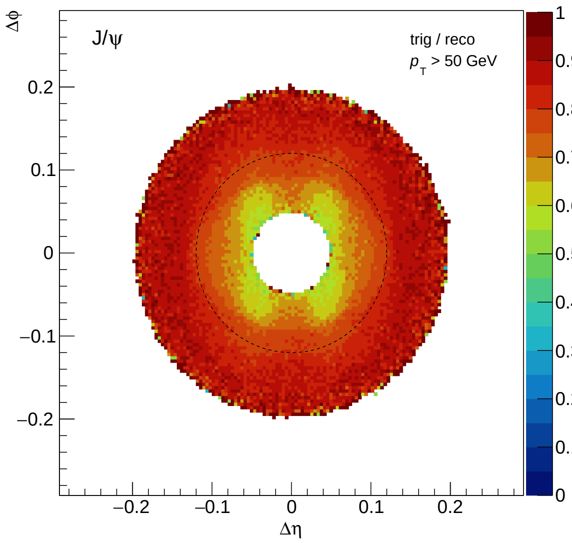

Figure 6.5: Ratio between "trig" (after applying the trigger) and "reco" (before applying the trigger) simulated 2D event distributions, for J/ψ dimuons of $p_{\mathrm{T}} > 50$ GeV, in the $\Delta\phi$ vs. $\Delta\eta$ plane. The dashed black curve represents a circumference of $\Delta R = 0.12$.

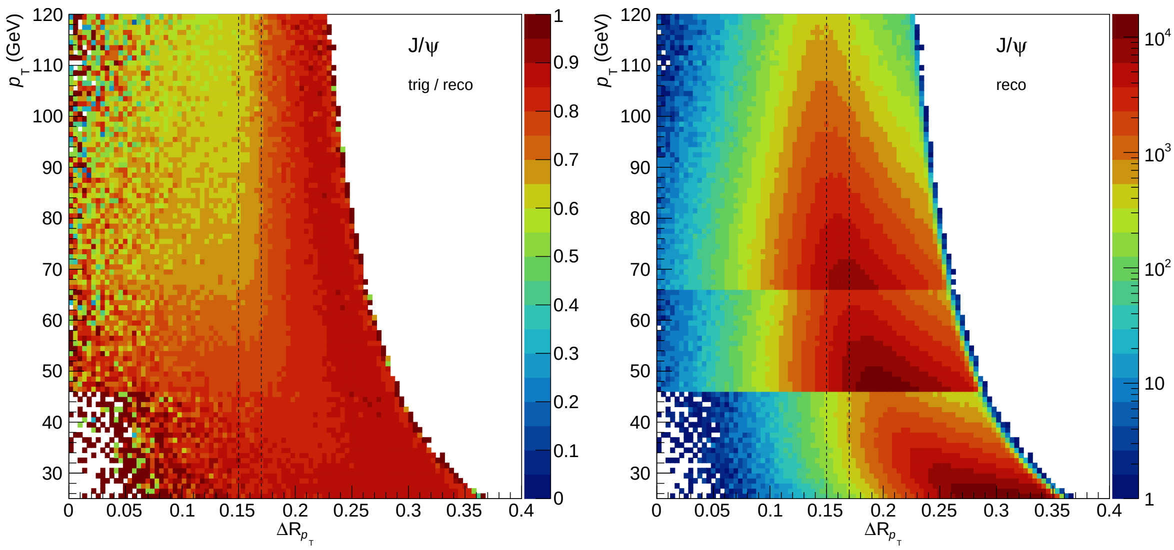

Figure 6.6: Left: Ratio between "trig" and "reco" simulated 2D event distributions, for J/ψ dimuons of $p_{\mathrm{T}} > 50$ GeV, in the p_{T} vs. $\Delta R_{p_{\mathrm{T}}}$ plane. Right: Corresponding "reco" event distribution. The dashed black lines represent the $\Delta R_{p_{\mathrm{T}}} = 0.15$ and $\Delta R_{p_{\mathrm{T}}} = 0.17$ cuts.

$\Delta\eta$ 2D distribution shows that the trigger efficiency is very low when the two muons are "too close to each other" in the variable $\Delta R = \sqrt{\Delta\phi^2 + \Delta\eta^2}$.

The dimuon trigger efficiency depends also on the difference between the p_{T} of the two muons, Δp_{T}, and it is better to isolate and reject regions of low dimuon efficiency applying cuts on the variable $\Delta R_{p_{\mathrm{T}}}$, defined as

$$\Delta R_{p_{\mathrm{T}}} = \sqrt{\Delta\phi^2 + \Delta\eta^2} + \frac{\log|\Delta p_{\mathrm{T}}|}{b} \qquad (b = 45)\,. \tag{6.2}$$

Figure 6.6-left shows that rejecting events of $\Delta R_{p_{\mathrm{T}}} < 0.17$ leads to a J/ψ event sample where all the dimuons have trigger efficiency above 70%, so that the sample is much less sensitive to the accuracy

of the MC efficiency correction. Figure 6.6-right shows the p_{T} vs. $\Delta R_{p_{\mathrm{T}}}$ 2D event distribution before applying the trigger emulation (the "reco" sample). It is evident that a $\Delta R_{p_{\mathrm{T}}} = 0.17$ cut rejects a very large fraction of the high-p_{T} events. Therefore, for $p_{\mathrm{T}} > 70$ GeV, a looser cut of $\Delta R_{p_{\mathrm{T}}} = 0.15$ is used (corresponding to an efficiency threshold of 60%), to avoid losing too many events, as otherwise the λ_ϑ measurement becomes too uncertain to provide meaningful results. For the $\psi(2\mathrm{S})$ sample, a similar evaluation leads to a $p_{\mathrm{T}} = 50$ GeV cutoff for the looser $\Delta R_{p_{\mathrm{T}}}$ cut.

Since the $\Delta R_{p_{\mathrm{T}}}$ cuts reduce the $|\cos\vartheta|$ coverage, the baseline λ_ϑ values are also recomputed, fitting the $|\cos\vartheta|$ distribution in the same range, to ensure that potential variations are exclusively caused by the ρ factor.

Figure 6.7 shows the differences between the λ_ϑ values measured with the event sample selected by the $\Delta R_{p_{\mathrm{T}}}$ cuts, where the dimuon detection efficiency is always quite high and the sample is not very sensitive to the accuracy of the trigger emulation in the simulated events, and the values measured without applying such a cut, for prompt J/ψ (left) and $\psi(2\mathrm{S})$ (right). No significant variation of $\Delta\lambda_\vartheta$ with p_{T} is seen; the fluctuations around zero are caused by the reduction in the size of the event sample (they are not seen when a coarser p_{T} binning is used, as shown by the red points on the J/ψ panel). Therefore, this is considered a passed check and no systematic uncertainty is assigned to the measurement from this source.

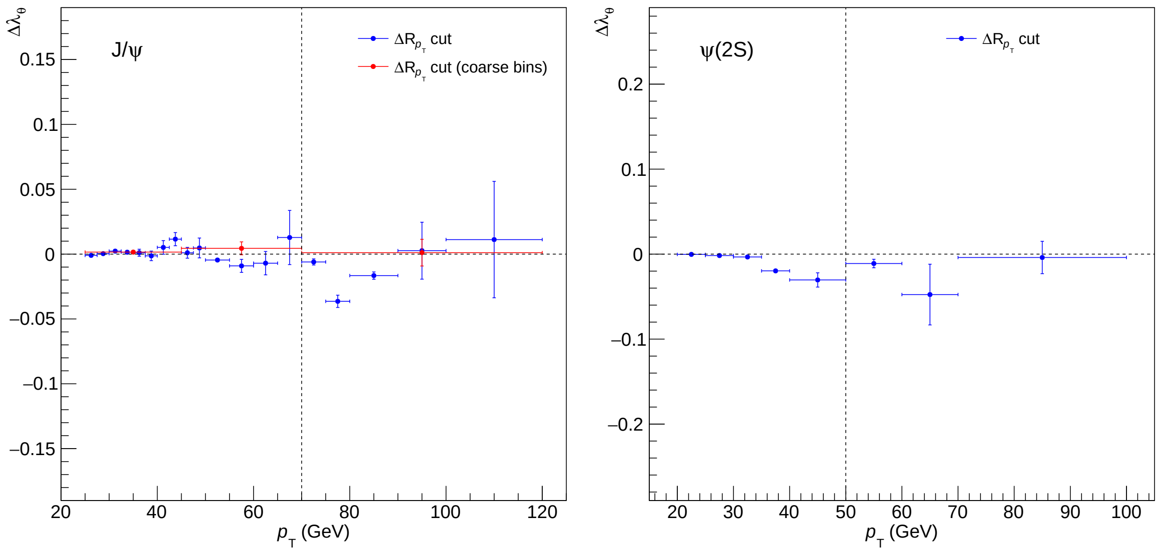

Figure 6.7: Difference between the λ_ϑ values measured with and without applying the $\Delta R_{p_{\mathrm{T}}}$ cuts, vs. p_{T}, for the J/ψ (left), and the $\psi(2\mathrm{S})$ (right) analysis, in the standard p_{T} bins (blue points) and in a coarser p_{T} binning (red points, for the J/ψ). The dashed vertical lines mark the p_{T} value above which we use a looser $\Delta R_{p_{\mathrm{T}}}$ cut.

6.4 Fit model of the dimuon mass distributions

The J/ψ and $\psi(2\mathrm{S})$ line shapes do not enter directly in the determination of the fractions of mass-continuum muon pairs in the signal mass windows because, as was described in Sections 5.2.1 and 5.2.2 for the NPS and PRS cases, respectively, the denominator is the number of counted events. The description of the peak line shape is only required to be accurate enough not to bias the fit of the mass-continuum background contribution. To this end, the signal fit model function is chosen such that it describes the simulated and measured peak shapes, with a sum of two Crystal-Ball functions for the $\psi(2\mathrm{S})$ and an added Gaussian function in the case of the J/ψ. It is considered that this description is sufficient for the purposes of the analysis, but it is necessary to evaluate whether it could be introducing a bias in the determination of the background term.

In the case of the $\psi(2\mathrm{S})$ analysis, the mass-continuum dimuon background has a relatively high contribution, with respect to the $\psi(2\mathrm{S})$ peak, so that it is important, for the polarization measurement, to precisely evaluate the fraction of events in the signal mass window coming from that background. It is in this case that an incorrect fit of the dimuon mass distributions would have the largest impact on the final λ_ϑ results.

The rather broad sideband ranges, both on the left and right sides of the $\psi(2\mathrm{S})$ peak, allow for an alternative procedure to evaluate the background fraction, completely avoiding the necessity to describe the $\psi(2\mathrm{S})$ peak. It is possible to simply count the number of events in each of the two sideband mass windows and then compute the interpolated event yield in the signal mass window, assuming that the mass distribution follows a decreasing exponential function. In other words, this procedure only considers the mass ranges where the signal peak has no contribution at all, so that the background level can be computed without the need to describe the peak line shape.

Figure 6.8 compares the mass-continuum dimuon background fractions in the $\psi(2\mathrm{S})$ mass window, for the NP and PR cases, when computed with the alternative "event counting" method and with the baseline fit procedure. The two procedures lead to essentially identical results, confirming that the functional form used to describe the peak line shape does not bias the extraction of the background levels.

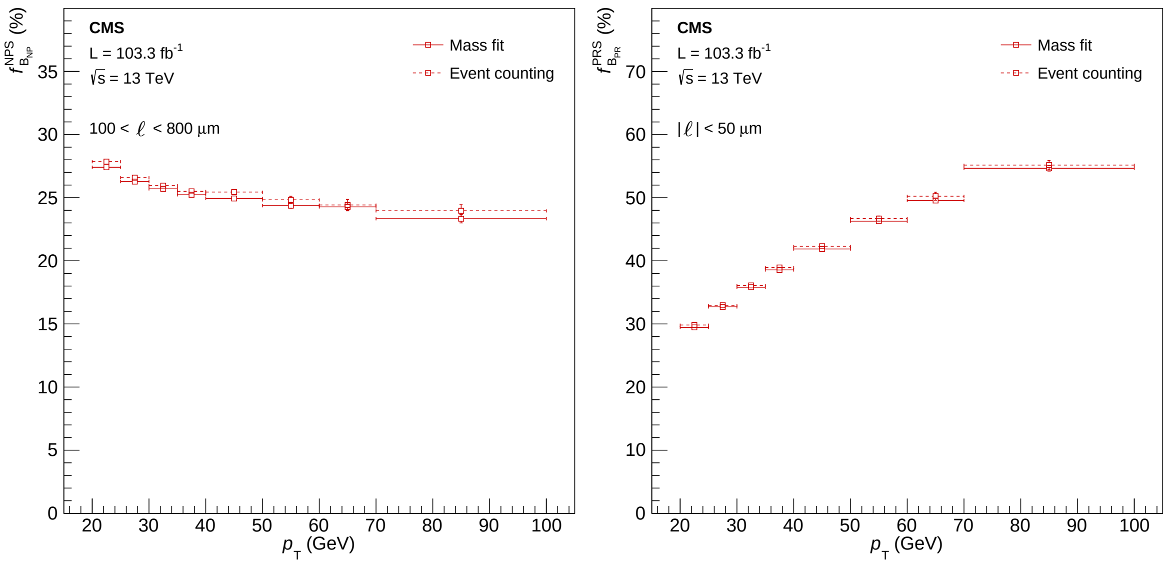

Figure 6.8: Variation with p_T of the fraction of events in the NPS (left) and PRS (right) regions due to mass-continuum muon pairs, computed with the baseline fit procedure (solid lines) and with the event counting alternative (dashed lines).

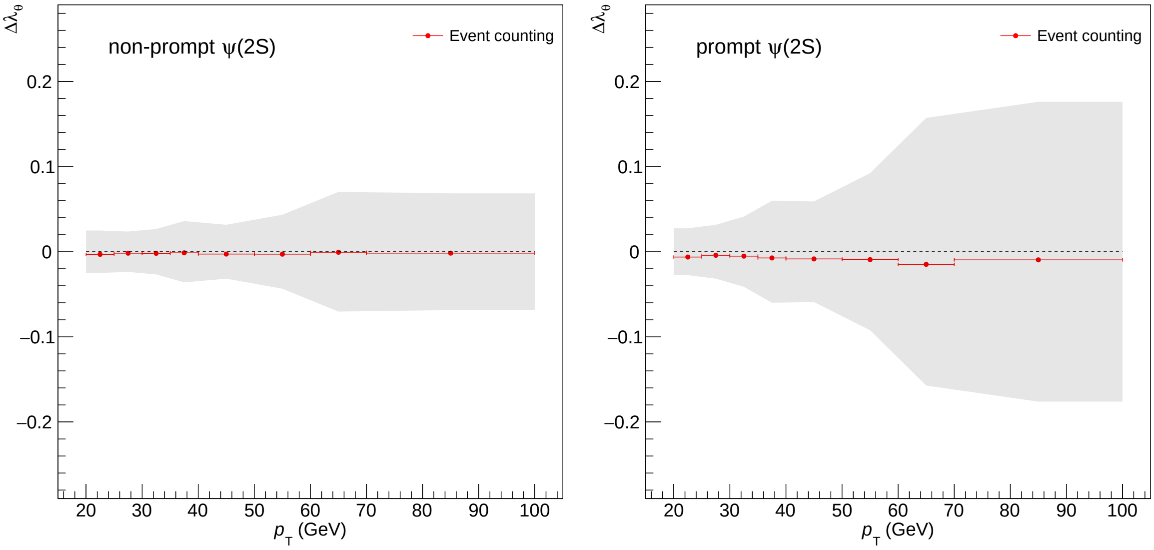

Figure 6.9: Differences between the λ_ϑ values obtained with the background event counting procedure and the baseline procedure, compared to the statistical uncertainties of the baseline measurement (grey band), for the NP (left) and PR (right) $\psi(2S)$ analyses.

Propagating the alternative background fractions to the λ_ϑ measurement, it is possible to compute the differences with respect to the baseline results, which are shown in Fig. 6.9. The obtained variations are negligible with respect to the statistical uncertainties, so that this is considered to be a passed check and no systematic uncertainty is assigned to the $\psi(2S)$ dimuon mass fit model.

In the case of the J/ψ analysis, the mass-continuum dimuon background is very small and, furthermore, the left sideband is quite narrow. This means that the analysis does not have access to a signal-free LSB window, because a small level of signal events could contaminate the available sideband window. Therefore, the counting method used in the $\psi(2S)$ case is not applicable in the J/ψ case. Instead, to test the method, the fits of the dimuon mass distributions are redone with variations in the shape of the J/ψ tail, to evaluate if it could significantly contribute to the LSB window, thereby biasing the evaluation of the level of the continuum background. More specifically, the α CB tail parameter is fixed to values equal to the baseline value plus or minus the value of its uncertainty, σ_α, as determined in the baseline fit.

As for the other sources of potential systematic uncertainties, the λ_ϑ measurement is redone with the varied α values and the differences with respect to the baseline measurement are computed. The results are shown in Fig. 6.10. The $\Delta\lambda_\vartheta$ vs. p_T values are very close to zero for the J/ψ as well, and also in this case this is considered a passed check and no systematic uncertainty is assigned.

6.5 Fit model of the dimuon lifetime distributions

As described in Section 5.2.2, the fits of the lifetime distributions include a term, corresponding to the mass-continuum dimuon background, that is fixed, in shape and normalization. While the shape is well parametrized by the selected functional form (one exponential for the J/ψ and two for the $\psi(2S)$),

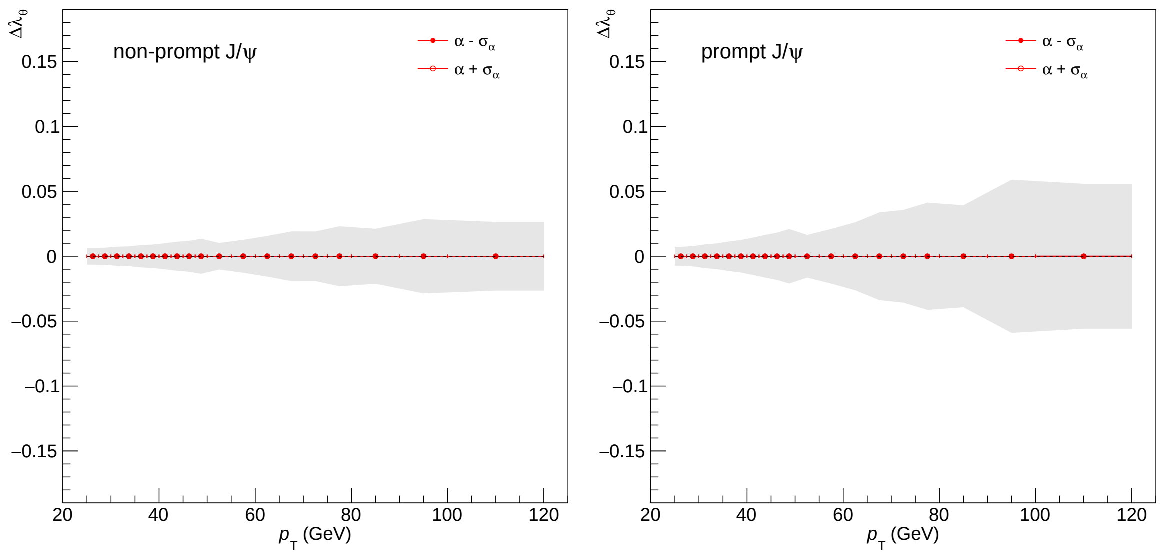

Figure 6.10: Differences between the λ_ϑ values obtained with the varied CB tail parameter α and the baseline procedure, compared to the statistical uncertainties of the baseline measurement (grey band), for the NP (left) and PR (right) J/ψ analyses.

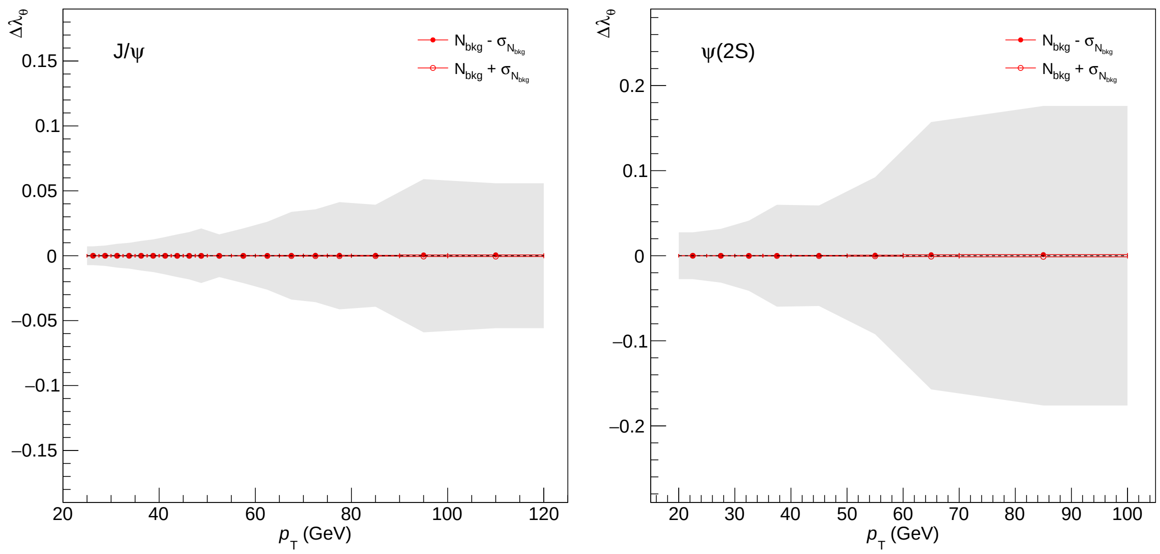

Figure 6.11: Differences between the λ_ϑ values obtained with the varied normalization of the lifetime term reflecting the mass-continuum background and the baseline procedure, compared to the statistical uncertainties of the baseline measurement (grey band), for the prompt J/ψ (left) and $\psi(2\mathrm{S})$ (right) analyses.

the normalization is obtained with a certain (statistical) uncertainty. The effect that this uncertainty has on the final results can be evaluated by redoing the analysis varying the normalization, adding or subtracting its uncertainty. Of course, this effect is only relevant for the prompt polarizations, given that the non-prompt analysis is completely insensitive to the lifetime dimension. The results are shown in Fig. 6.11, for the J/ψ (left) and $\psi(2\mathrm{S})$ (right) cases.

The $\Delta\lambda_\vartheta$ vs. p_T patterns seen in Fig. 6.11 are perfectly compatible with zero and independent of p_T. Therefore, this is considered a passed check and no systematic uncertainty is assigned to the measurement from this source.

6.6 Potential residual azimuthal anisotropy in the helicity frame

As mentioned in Section 5.1, the phase space window of the analysis motivates a one-dimensional study of the more significant $|\cos\vartheta|$ decay angle in the HX frame, integrating over φ, rather than a two-dimensional analysis using Eq. 2.2 to fit both angles simultaneously. This is done under the assumption, expected to be valid in the conditions of the analysis, that there are no correlations between $|\cos\vartheta|$ and φ in the two-dimensional acceptance maps.

In order to search for any residual azimuthal dependence on φ, and evaluate its potential impact on the final λ_ϑ, it is possible to redo the analysis, in exactly the same way, replacing the $|\cos\vartheta|$ polar angle by the φ azimuthal angle. All other elements of the analysis, from the p_{T} bins to the fractions of background contamination, are unchanged.

The φ distributions, obtained after background subtraction and corrected for acceptance as explained in previous chapters, are then fitted with the function

$$W(\varphi|\vec{\lambda}) \propto 1 + \beta\cos 2\varphi\,, \tag{6.3}$$

where $\beta = (2\,\lambda_\varphi)\,/\,(3+\lambda_\theta)$.

The fitted values of β, for both the prompt and non-prompt J/ψ and $\psi(2\mathrm{S})$ mesons, are very close to zero, as can be seen in Fig. 6.12. This confirms that the analysis can be done in $|\cos\vartheta|$, integrating over the φ angle, neglecting residual correlations between the two angles.

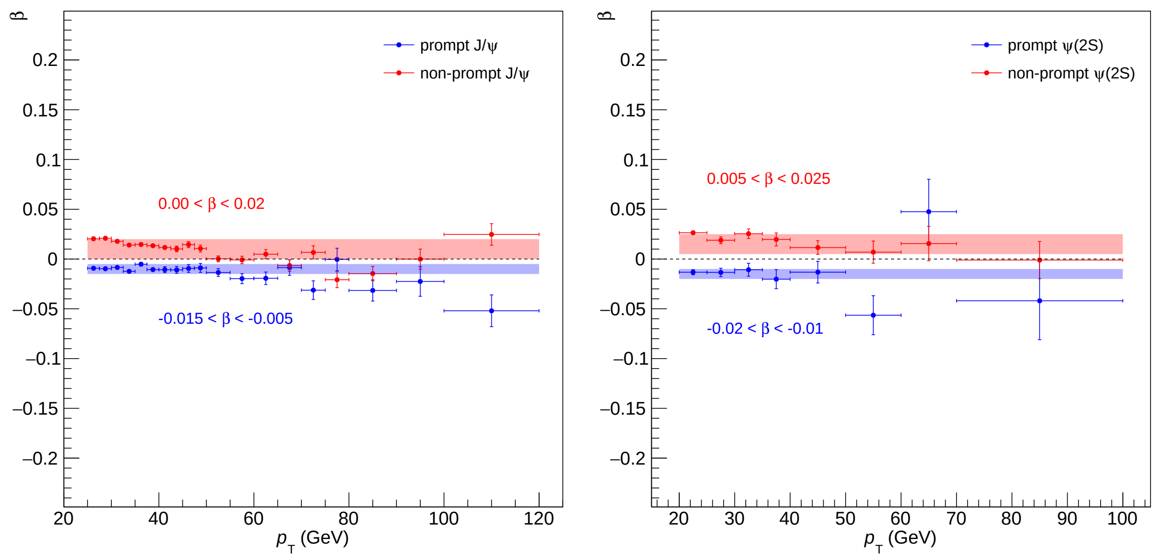

Figure 6.12: Fitted β values, versus p_{T}, for the prompt (blue) and non-prompt (red) J/ψ (left) and $\psi(2\mathrm{S})$ (right) analyses. The bands represent the chosen estimates for the β ranges.

It is worth noting that small non-zero β values are not necessarily evidence that there are residual differences between the acceptance maps evaluated through the MC simulations and the real acceptance maps of the actual detector. In other words, even a perfect MC simulation can lead to acceptance-corrected distributions that exhibit small azimuthal anisotropies in the HX frame. The reason for this is that the analysis uses the proton-proton HX frame and not the parton-parton HX frame, which would be

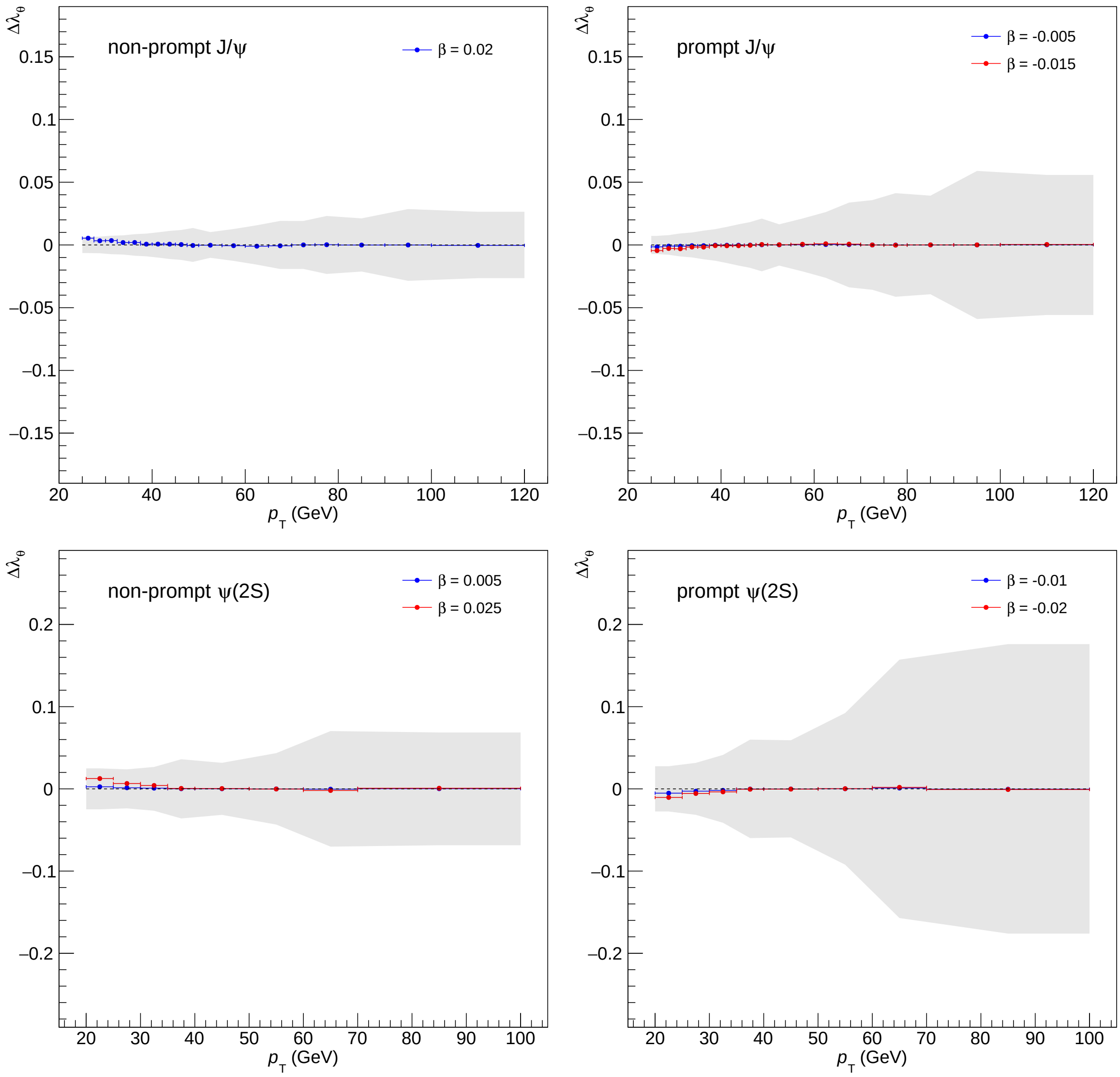

Figure 6.13: Difference $\Delta\lambda_\vartheta$ between the λ_ϑ values measured with the reweighed acceptance maps (using the β values mentioned in the legends) and the baseline values, vs. p_T, for the non-prompt (left) and prompt (right) J/ψ (top) and $\psi(2\mathrm{S})$ (bottom) analyses.

more suitable to measure the prompt J/ψ and $\psi(2\mathrm{S})$ polarization, but which it is not possible to access. Similarly, the B meson frame would be more suitable to measure the polarization of non-prompt J/ψ and $\psi(2\mathrm{S})$ mesons, but is also not available in this analysis. Since it is not possible to access those "natural" frames, the measurements must thus be reported in the proton-proton HX frame, where small azimuthal anisotropies can be expected, even if they are absent in the ideal frames.

Nevertheless, to be conservative, the extreme hypothesis that the residual non-flatness of the φ distributions is entirely caused by a mismatch between MC and data is considered. Hence, estimates for the β ranges are established, shown as red and blue bands in Fig. 6.12, and new $|\cos\vartheta|$ vs. p_T acceptance maps are computed, reweighing each MC event by the weight $1+\beta\cdot\cos(2\varphi)$, which depends on the φ of the event.

The differences between the λ_ϑ values obtained with the alternative maps (in the upper and lower limits of each β range) and those of the baseline analysis are shown in Fig. 6.13, for the non-prompt (left) and prompt (right) J/ψ (top) and $\psi(2S)$ (bottom) analyses. They are negligible with respect to the grey bands, which represent the statistical uncertainty of the baseline results, so that this could be considered to be a passed check. Conservatively, a systematic uncertainty from this source is assigned, up to 37.5 GeV for the J/ψ case and 35 GeV for the $\psi(2S)$, computed from the difference between the λ_ϑ values obtained with the most extreme β scenario and the baseline values. This uncertainty is asymmetric but it is quite small so that symmetric total systematic uncertainties are retained, for simplicity.

6.7 Closure test of the polarization fit procedure

As a check of the polarization fitting procedure, a Monte Carlo closure test is performed to verify that it provides results consistent with the generated values. J/ψ MC samples are generated with λ_ϑ values between -1 and +1, in steps of 0.1. The analysis is then run on these samples and the corresponding λ_ϑ values are obtained versus p_T, as well as the differences between the output and input values.

The results show no indications of a bias in the procedure, as can be seen in Fig. 6.14, where the left panel shows the λ_ϑ values obtained from each of the MC samples and the right panel shows the $\Delta\lambda_\vartheta$ between generated and returned values for the three most relevant λ_ϑ, given the range of values shown in Fig. 5.26. Therefore, no systematic uncertainty is assigned to this potential effect.

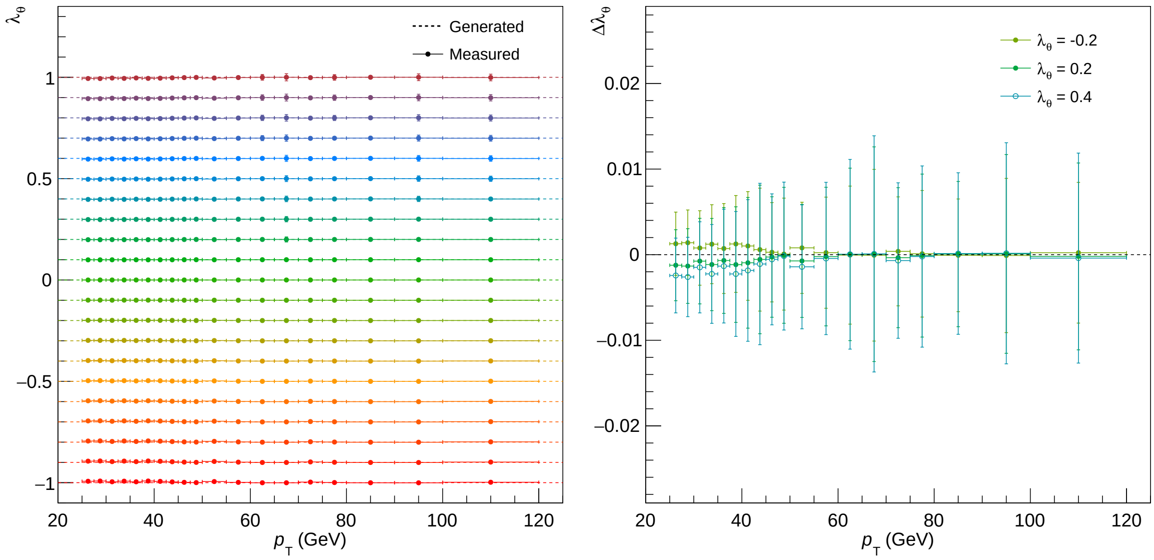

Figure 6.14: Left: λ_ϑ values obtained from the J/ψ MC samples (markers) compared to the generated values (dashed lines). Right: Difference $\Delta\lambda_\vartheta$ between the returned values and the generated values, only for the three most relevant λ_ϑ values, for visibility purposes.

6.8 Summary of the systematic uncertainties

All the uncertainties described in the previous sections of this chapter are summed in quadrature to give the total systematic uncertainty of the measurements. The numerical values are collected in Tables 6.1 and 6.2 for the J/ψ and $\psi(2\mathrm{S})$, respectively.

p_T (GeV)	Prompt J/ψ			Non-prompt J/ψ		
	μ eff.	β	total	μ eff.	β	total
25–27.5	±0.011	-0.004	±0.012	±0.010	+0.005	±0.011
27.5–30	±0.008	-0.003	±0.009	±0.007	+0.003	±0.008
30–32.5	±0.007	-0.003	±0.007	±0.006	+0.003	±0.007
32.5–35	±0.006	-0.002	±0.006	±0.005	+0.002	±0.005
35–37.5	±0.005	-0.002	±0.005	±0.004	+0.002	±0.005
37.5–40	±0.004	–	±0.004	±0.004	–	±0.004
40–42.5	±0.004	–	±0.004	±0.003	–	±0.003
42.5–45	±0.003	–	±0.003	±0.003	–	±0.003
45–47.5	±0.002	–	±0.002	±0.002	–	±0.002
47.5–50	±0.001	–	±0.001	±0.001	–	±0.001
50–55	–	–	–	–	–	–
55–60	–	–	–	–	–	–
60–65	–	–	–	–	–	–
65–70	–	–	–	–	–	–
70–75	–	–	–	–	–	–
75–80	–	–	–	–	–	–
80–90	–	–	–	–	–	–
90–100	–	–	–	–	–	–
100–120	–	–	–	–	–	–

Table 6.1: Systematic uncertainties affecting the J/ψ polarization measurement.

p_T (GeV)	Prompt $\psi(2\mathrm{S})$			Non-prompt $\psi(2\mathrm{S})$		
	μ eff.	β	total	μ eff.	β	total
20–25	±0.014	-0.010	±0.018	±0.014	+0.013	±0.018
25–30	±0.008	-0.006	±0.010	±0.008	+0.007	±0.010
30–35	±0.005	-0.004	±0.006	±0.004	+0.004	±0.006
35–40	±0.001	–	±0.001	±0.001	–	±0.001
40–50	–	–	–	–	–	–
50–60	–	–	–	–	–	–
60–70	–	–	–	–	–	–
70–100	–	–	–	–	–	–

Table 6.2: Systematic uncertainties affecting the $\psi(2\mathrm{S})$ polarization measurement.

Chapter 7

Results and summary

7.1 Summary of the experimental results

The final results of this analysis are displayed in Fig. 7.1, which shows the λ_ϑ parameters, measured in the helicity frame, for the prompt and non-prompt J/ψ and $\psi(2\mathrm{S})$ mesons, with the vertical bars representing the statistical and systematic uncertainties summed in quadrature.

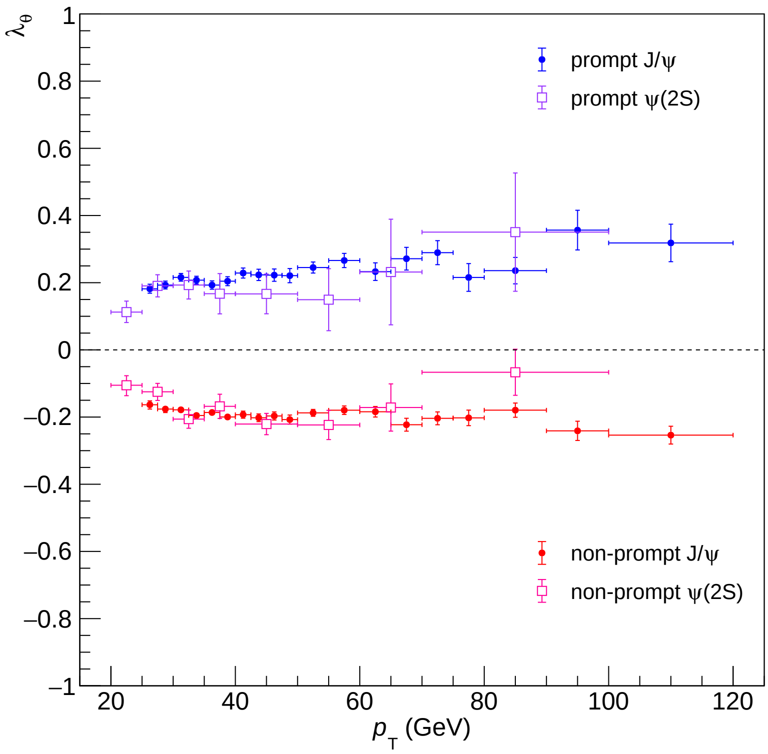

Figure 7.1: λ_ϑ parameter measured in the helicity frame, as a function of p_T, for the prompt and non-prompt J/ψ and $\psi(2\mathrm{S})$ mesons. The vertical bars represent the statistical and systematic uncertainties summed in quadrature.

7.2 Non-prompt polarizations: data versus theory

Figure 7.2 shows the λ_ϑ parameter measured for the non-prompt J/ψ and $\psi(2\mathrm{S})$ mesons, as a function of p_T. For $p_\mathrm{T} > 30$ GeV, the measured values show a flat p_T dependence, at around $\lambda_\vartheta \approx -0.2$. No significant differences are seen between the J/ψ and $\psi(2\mathrm{S})$ trends.

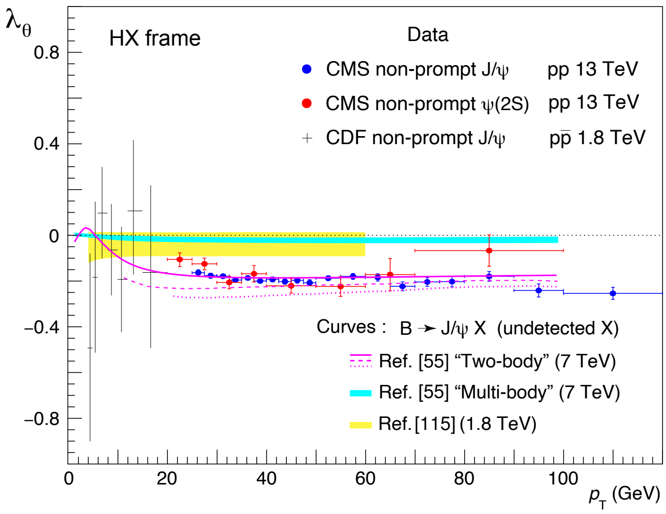

Figure 7.2: The λ_ϑ parameter measured, as a function of p_T, for non-prompt J/ψ and $\psi(2\mathrm{S})$ mesons. The vertical bars represent the total uncertainties. Predicted polarizations of J/ψ mesons produced in $\mathrm{B} \to \mathrm{J}/\psi\, X$ decays are shown for three calculations [55, 115], discussed in the text. The low-p_T CDF measurement [21] is also shown.

The pink and light blue bands represent the corresponding polarizations of J/ψ mesons produced in $\mathrm{B} \to \mathrm{J}/\psi\, X$ decays, computed in Ref. [55] and described in Section 2.3.3. As discussed there, these predictions correspond to two hypothetical cases denoted as “two-body” and “multi-body”. For the “two-body” case, the dashed and dotted curves reflect a minimum p_T requirement for the two J/ψ decay muons of 5 and 10 GeV, respectively, while the solid curve represents the calculation without any p_T requirement. Comparing the data points and the computed curves indicates that non-prompt J/ψ production, at least in the dimuon p_T range covered by this measurement ($p_\mathrm{T} > 25$ GeV), is dominated by the “two-body” topology, where, interestingly, the J/ψ is expected to be predominantly produced through colour-singlet processes [57, 58].

The non-prompt J/ψ polarization measured by CDF [21] in $p\overline{p}$ collisions at $\sqrt{s} = 1.8$ TeV, in the $|y| < 0.6$ range, is also shown, together with a computation made for the CDF conditions (yellow band), where NRQCD colour-octet contributions are found to dominate [114, 115]. This prediction, leading to an almost vanishing non-prompt polarization, is in disagreement with the measurement performed in this analysis.

7.3 Prompt polarizations: data versus theory

Figure 7.3 shows the λ_ϑ measurements obtained in this analysis for the prompt J/ψ (left) and $\psi(2\mathrm{S})$ (right) mesons. The results previously reported by CMS and LHCb for pp collisions at $\sqrt{s} = 7$ TeV [37, 39, 96] are also shown, extending the p_T coverage down to much lower p_T. In the p_T ranges where there are measurements from both the new and the previous CMS analyses, the two sets of points are in agreement, within the relatively large uncertainties of the 2011 data.

Considering all measurements together (neglecting possible differences with collision energy and rapidity interval), the λ_ϑ patterns show a significant trend from negative to positive, with the sign change occurring at $p_\mathrm{T} \sim 15$ GeV. At high p_T, the polarization tends to an asymptotic value, $\lambda_\vartheta \approx +0.3$. There is no evidence of the strong transverse polarizations (λ_ϑ approaching +1) expected in case the ${}^3S_1^{[8]}$ and ${}^3P_J^{[8]}$ octet terms would dominate.

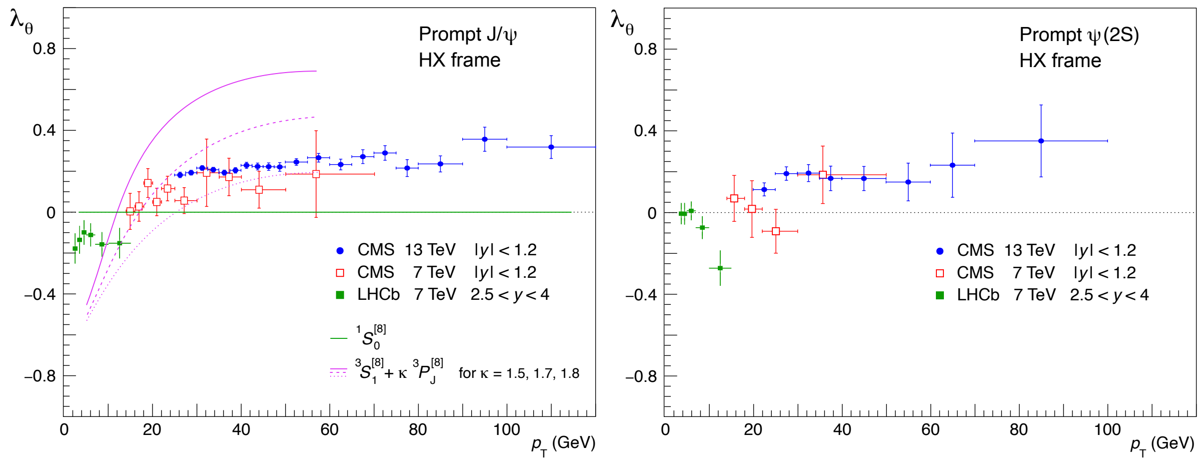

Figure 7.3: The λ_ϑ parameter measured, as a function of p_T, for prompt J/ψ (left) and $\psi(2\mathrm{S})$ (right) mesons, in pp collisions at $\sqrt{s} = 13$ TeV, compared to measurements made at 7 TeV by CMS [37] and LHCb [39, 96]. The vertical bars represent the total uncertainties. The curves on the left panel are described in the text.

It is interesting to compare the measured p_T dependence with the pattern obtainable as a superposition of the three dominant NRQCD colour octet terms, ${}^1S_0^{[8]}$, ${}^3S_1^{[8]}$, and ${}^3P_J^{[8]}$, recalling the discussion in Chapter 2. The first term yields zero (p_T independent) polarization, while the remaining two, considered in a mutual combination of the kind ${}^3S_1^{[8]} + \kappa {}^3P_J^{[8]}$ as introduced in Section 2.5.2, are characterized by a λ_ϑ trend qualitatively similar to the measured one, going from longitudinal to transverse at a p_T transition point that depends on their relative proportions, symbolically represented by the κ coefficient. This behaviour is illustrated by the family of curves displayed in Fig. 2.17, based on NLO calculations made for $\sqrt{s} = 7$ TeV and mid-rapidity as discussed in Ref. [118].

Three examples of such polarized colour-octet combinations are shown in Fig. 7.3 (left), in pink, together with the unpolarized term, represented by the green horizontal line at zero. The comparison between the J/ψ data points (with much smaller uncertainties than the $\psi(2\mathrm{S})$ points) and the curves shows that precise polarization measurements significantly constrain the overall NRQCD colour-octet contributions: the value of p_T where λ_ϑ changes sign determines κ, while the high-p_T asymptotic λ_ϑ

value constrains the relative weight of the polarized ($^3S_1^{[8]} + \kappa^3P_J^{[8]}$) and unpolarized ($^1S_0^{[8]}$) colour-octet terms.

7.4 Tables of results

The numerical values of the measurements described in this thesis are collected in Tables 7.1 and 7.2, for the prompt and non-prompt J/ψ and $\psi(2\mathrm{S})$ polarizations, respectively.

p_{T} (GeV)	Prompt J/ψ				Non-prompt J/ψ			
	λ_ϑ	σ_{stat}	σ_{sys}	σ_{tot}	λ_ϑ	σ_{stat}	σ_{sys}	σ_{tot}
25–27.5	0.182	0.007	0.012	0.014	-0.163	0.006	0.011	0.013
27.5–30	0.193	0.008	0.009	0.012	-0.176	0.007	0.008	0.010
30–32.5	0.216	0.009	0.007	0.012	-0.178	0.007	0.007	0.010
32.5–35	0.208	0.010	0.006	0.012	-0.195	0.008	0.005	0.009
35–37.5	0.193	0.011	0.005	0.012	-0.186	0.009	0.005	0.010
37.5–40	0.204	0.013	0.004	0.013	-0.200	0.009	0.004	0.010
40–42.5	0.229	0.014	0.004	0.015	-0.193	0.010	0.003	0.011
42.5–45	0.223	0.016	0.003	0.017	-0.202	0.011	0.003	0.012
45–47.5	0.223	0.018	0.002	0.018	-0.197	0.012	0.002	0.012
47.5–50	0.221	0.021	0.001	0.021	-0.207	0.014	0.001	0.014
50–55	0.245	0.016	–	0.016	-0.188	0.010	–	0.010
55–60	0.266	0.021	–	0.021	-0.180	0.013	–	0.013
60–65	0.233	0.026	–	0.026	-0.184	0.016	–	0.016
65–70	0.271	0.034	–	0.034	-0.223	0.019	–	0.019
70–75	0.289	0.036	–	0.036	-0.204	0.019	–	0.019
75–80	0.216	0.041	–	0.041	-0.202	0.023	–	0.023
80–90	0.236	0.039	–	0.039	-0.179	0.021	–	0.021
90–100	0.357	0.059	–	0.059	-0.241	0.029	–	0.029
100–120	0.318	0.056	–	0.056	-0.254	0.026	–	0.026

Table 7.1: λ_ϑ parameter, in the HX frame, as a function of p_{T}, for the prompt and non-prompt J/ψ mesons, with the statistical (σ_{stat}), systematic (σ_{sys}) and total (σ_{tot}) uncertainties. All uncertainties are symmetrical.

p_{T} (GeV)	Prompt $\psi(2\mathrm{S})$				Non-prompt $\psi(2\mathrm{S})$			
	λ_ϑ	σ_{stat}	σ_{sys}	σ_{tot}	λ_ϑ	σ_{stat}	σ_{sys}	σ_{tot}
20–25	0.112	0.028	0.018	0.033	-0.105	0.025	0.018	0.031
25–30	0.191	0.032	0.010	0.033	-0.125	0.024	0.010	0.026
30–35	0.193	0.041	0.006	0.042	-0.206	0.027	0.006	0.027
35–40	0.167	0.060	0.001	0.060	-0.168	0.036	0.001	0.036
40–50	0.167	0.059	–	0.059	-0.221	0.032	–	0.032
50–60	0.149	0.092	–	0.092	-0.223	0.043	–	0.043
60–70	0.232	0.157	–	0.157	-0.172	0.070	–	0.070
70–100	0.351	0.176	–	0.176	-0.067	0.069	–	0.069

Table 7.2: λ_ϑ parameter, in the HX frame, as a function of p_{T}, for the prompt and non-prompt $\psi(2\mathrm{S})$ mesons, with the statistical (σ_{stat}), systematic (σ_{sys}) and total (σ_{tot}) uncertainties. All uncertainties are symmetrical.

7.5 Summary

The prompt and non-prompt J/ψ and $\psi(2\mathrm{S})$ λ_ϑ polarization parameters have been measured, in the helicity frame and for $|y| < 1.2$, using a sample of pp collisions at $\sqrt{s} = 13\,$TeV collected in 2017 and 2018, corresponding to an integrated luminosity of 103.3 fb^{-1}. The results cover a very broad p_T range, up to p_T values of 100 and 120 GeV for the $\psi(2\mathrm{S})$ and J/ψ, respectively, significantly extending the p_T coverage of previous measurements.

Thanks to their good precision and broad p_T coverage, the measurements exclude the hypothesis that the quarkonium polarizations under study are p_T-independent.

The non-prompt J/ψ and $\psi(2\mathrm{S})$ polarization measurements are compatible with each other, in terms of p_T dependence and overall magnitude, and show a flat p_T dependence for $p_\mathrm{T} > 30$ GeV, with $\lambda_\vartheta \approx -0.2$ in that region. The measured trends agree with predictions based on the hypothesis of dominant production by two-body B meson decays, where colour-singlet processes dominate production.

Regarding the prompt results, there appears to be no evidence of strong transverse polarizations (λ_ϑ approaching +1), up to p_T values exceeding 30 times the J/ψ mass. Using NRQCD terminology, this means that there is no evidence that, at very high p_T, the transversely polarized ${}^3S_1^{[8]}$ and ${}^3P_J^{[8]}$ terms become dominant with respect to the unpolarized ${}^1S_0^{[8]}$ octet. Taken together with previous CMS and LHCb measurements, which cover a lower p_T domain, a significant variation of the prompt polarizations with p_T is observed at low p_T.

These results provide important constraints to be included in future phenomenological analyses of quarkonium production, so far mostly focused on p_T-differential cross sections. The J/ψ and $\psi(2\mathrm{S})$ polarization measurements can be combined with other experimental constraints, including the χ_{c1}, χ_{c2}, and $\psi(2\mathrm{S})$ feed-down fractions into the J/ψ and the polarizations of the χ_{c1} and χ_{c2} states, among others. For example, the strong similarity between the J/ψ and $\psi(2\mathrm{S})$ polarizations, now established with a much higher precision than in previous measurements, represents a significant and model-independent constraint on the χ_{c1} and χ_{c2} polarizations, independent from and complementary to direct measurements [111], as shown in Ref. [117].

Bibliography

[1] S. L. Glashow, Partial-symmetries of weak interactions, *Nucl. Phys.* **22**, 579 (1961).

[2] M. Gell-Mann, A Schematic Model of Baryons and Mesons, *Phys. Lett.* **8**, 214 (1964).

[3] S. Weinberg, A Model of Leptons, *Phys. Rev. Lett.* **19**, 1264 (1967).

[4] A. Salam, *8th Nobel Symposium* (1968), p. 367.

[5] F. Englert, R. Brout, Broken Symmetry and the Mass of Gauge Vector Mesons, *Phys. Rev. Lett.* **13**, 321 (1964).

[6] P. W. Higgs, Broken Symmetries and the Masses of Gauge Bosons, *Phys. Rev. Lett.* **13**, 508 (1964).

[7] G. S. Guralnik, C. R. Hagen, T. W. B. Kibble, Global Conservation Laws and Massless Particles, *Phys. Rev. Lett.* **13**, 585 (1964).

[8] CMS Collaboration, Observation of a new boson at a mass of 125 GeV with the CMS experiment at the LHC, *Phys. Lett. B* **716**, 30 (2012).

[9] ATLAS Collaboration, Observation of a new particle in the search for the Standard Model Higgs boson with the ATLAS detector at the LHC, *Phys. Lett. B* **716**, 1 (2012).

[10] H. Fritzsch, M. Gell-Mann, H. Leutwyler, Advantages of the color octet gluon picture, *Phys. Lett. B* **47**, 365 (1973).

[11] H. D. Politzer, Reliable Perturbative Results for Strong Interactions?, *Phys. Rev. Lett.* **30**, 1346 (1973).

[12] D. J. Gross, F. Wilczek, Ultraviolet Behavior of Non-Abelian Gauge Theories, *Phys. Rev. Lett.* **30**, 1343 (1973).

[13] N. Brambilla, *et al.*, Heavy quarkonium: Progress, puzzles, and opportunities, *Eur. Phys. J. C* **71**, 1534 (2011).

[14] N. Brambilla, *et al.*, QCD and strongly coupled gauge theories: challenges and perspectives, *Eur. Phys. J. C* **74**, 2981 (2014).

[15] G. Bodwin, E. Braaten, P. Lepage, Rigorous QCD analysis of inclusive annihilation and production of heavy quarkonium, *Phys. Rev. D* **51**, 1125 (1995). [Erratum: Phys. Rev. D 55, 5853 (1997)].

[16] CDF Collaboration, Υ Production in $p\overline{p}$ Collisions at $\sqrt{s} = 1.8$ TeV, *Phys. Rev. Lett.* **75**, 4358 (1995).

[17] CDF Collaboration, J/ψ and $\psi(2\mathrm{S})$ Production in $p\overline{p}$ Collisions at $\sqrt{s} = 1.8$ TeV, *Phys. Rev. Lett.* **79**, 572 (1997).

[18] CDF Collaboration, Production of J/ψ Mesons from χ_c Meson Decays in $p\overline{p}$ Collisions at $\sqrt{s} = 1.8$ TeV, *Phys. Rev. Lett.* **79**, 578 (1997).

[19] D0 Collaboration, J/ψ production in $p\overline{p}$ collisions at $\sqrt{s} = 1.8$ TeV, *Phys. Lett. B* **370**, 239 (1996).

[20] M. Krämer, Quarkonium production at high-energy colliders, *Prog. Part. and Nucl. Phys.* **47**, 141 (2001).

[21] CDF Collaboration, Measurement of J/ψ and $\psi(2\mathrm{S})$ Polarization in $p\overline{p}$ Collisions at $\sqrt{s} = 1.8$ TeV, *Phys. Rev. Lett.* **85**, 2886 (2000).

[22] CDF Collaboration, Polarizations of J/ψ and $\psi(2\mathrm{S})$ Mesons Produced in $p\overline{p}$ Collisions at $\sqrt{s} = 1.96$ TeV, *Phys. Rev. Lett.* **99**, 132001 (2007).

[23] D0 Collaboration, Measurement of the Polarization of the $\Upsilon(1S)$ and $\Upsilon(2S)$ States in $p\overline{p}$ Collisions at $\sqrt{s} = 1.96$ TeV, *Phys. Rev. Lett.* **101**, 182004 (2008).

[24] E. Braaten, B. A. Kniehl, J. Lee, Polarization of prompt J/ψ at the Fermilab Tevatron, *Phys. Rev. D* **62**, 094005 (2000).

[25] P. Faccioli, C. Lourenço, J. Seixas, H. K. Wöhri, J/ψ Polarization from Fixed-Target to Collider Energies, *Phys. Rev. Lett.* **102**, 151802 (2009).

[26] P. Faccioli, C. Lourenço, J. Seixas, Rotation-Invariant Relations in Vector Meson Decays into Fermion Pairs, *Phys. Rev. Lett.* **105**, 061601 (2010).

[27] P. Faccioli, C. Lourenço, J. Seixas, New approach to quarkonium polarization studies, *Phys. Rev. D* **81**, 111502(R) (2010).

[28] P. Faccioli, C. Lourenço, J. Seixas, H. K. Wöhri, Model-independent constraints on the shape parameters of dilepton angular distributions, *Phys. Rev. D* **83**, 056008 (2011).

[29] P. Faccioli, C. Lourenço, J. Seixas, H. K. Wöhri, Towards the experimental clarification of quarkonium polarization, *Eur. Phys. J. C* **69**, 657 (2010).

[30] P. Faccioli, C. Lourenço, J. Seixas, H. K. Wöhri, Determination of χ_c and χ_b polarizations from dilepton angular distributions in radiative decays, *Phys. Rev. D* **83**, 096001 (2011).

[31] P. Faccioli, V. Knünz, C. Lourenço, J. Seixas, H. K. Wöhri, Quarkonium production in the LHC era: A polarized perspective, *Phys. Lett. B* **736**, 98 (2014).

[32] P. Faccioli, *et al.*, Quarkonium production at the LHC: A data-driven analysis of remarkably simple experimental patterns, *Phys. Lett. B* **773**, 476 (2017).

[33] P. Faccioli, *et al.*, From identical s- and p-wave p_{T} spectra to maximally distinct polarizations: probing NRQCD with χ states, *Eur. Phys. J. C* **78**, 268 (2018).

[34] P. Faccioli, C. Lourenço, M. Araújo, J. Seixas, Universal kinematic scaling as a probe of factorized long-distance effects in high-energy quarkonium production, *Eur. Phys. J. C* **78**, 118 (2018).

[35] CDF Collaboration, Measurements of the Angular Distributions of Muons from Υ Decays in $p\overline{p}$ Collisions at $\sqrt{s} = 1.96$ TeV, *Phys. Rev. Lett.* **108**, 151802 (2012).

[36] ALICE Collaboration, J/ψ Polarization in pp Collisions at $\sqrt{s} = 7$ TeV, *Phys. Rev. Lett.* **108**, 082001 (2012).

[37] CMS Collaboration, Measurement of the prompt J/ψ and $\psi(2\mathrm{S})$ polarizations in pp collisions at $\sqrt{s} = 7$ TeV, *Phys. Lett. B* **727**, 381 (2013).

[38] CMS Collaboration, Measurement of the Υ(1S), Υ(2S), and Υ(3S) Polarizations in pp Collisions at $\sqrt{s} = 7$ TeV, *Phys. Rev. Lett.* **110**, 081802 (2013).

[39] LHCb Collaboration, Measurement of J/ψ polarization in pp collisions at $\sqrt{s} = 7$ TeV, *Eur. Phys. J. C* **73**, 2631 (2013).

[40] CMS Collaboration, Measurement of the polarizations of prompt and non-prompt J/ψ and $\psi(2\mathrm{S})$ mesons produced in pp collisions at $\sqrt{s} = 13$ TeV, *Phys. Lett. B* **858**, 139044 (2024).

[41] J. E. Augustin, *et al.*, Discovery of a Narrow Resonance in e^+e^- Annihilation, *Phys. Rev. Lett.* **33**, 1406 (1974).

[42] J. J. Aubert, *et al.*, Experimental Observation of a Heavy Particle J, *Phys. Rev. Lett.* **33**, 1404 (1974).

[43] S. W. Herb, *et al.*, Observation of a Dimuon Resonance at 9.5 GeV in 400-GeV Proton-Nucleus Collisions, *Phys. Rev. Lett.* **39**, 252 (1977).

[44] R. L. Workman, *et al.* (Particle Data Group), Review of Particle Physics, *Prog. Theor. Exp. Phys.* **2022**, 083C01 (2022).

[45] R. Baier, R. Rückl, Hadronic production of J/ψ and Υ: Transverse momentum distributions, *Phys. Lett. B* **102**, 364 (1981).

[46] J. P. Lansberg, On the mechanisms of heavy-quarkonium hadroproduction, *Eur. Phys. J. C* **61**, 693 (2008).

[47] V. Barger, W. Y. Keung, R. J. N. Phillips, On ψ and Υ production via gluons, *Phys. Lett. B* **91**, 253 (1980).

[48] V. Barger, W. Y. Keung, R. J. N. Phillips, Hadroproduction of ψ and Υ, *Z. Phys. C* **6**, 169 (1980).

[49] A. Andronic, *et al.*, Heavy-flavour and quarkonium production in the LHC era: from proton–proton to heavy-ion collisions, *Eur. Phys. J. C* **76**, 107 (2016).

[50] Private Communication from P. Faccioli.

[51] G. C. Nayak, J.-W. Qiu, G. Sterman, Fragmentation, factorization and infrared poles in heavy quarkonium production, *Phys. Lett. B* **613**, 45 (2005).

[52] G. C. Nayak, J.-W. Qiu, G. Sterman, Fragmentation, nonrelativistic QCD, and NNLO factorization analysis in heavy quarkonium production, *Phys. Rev. D* **72**, 114012 (2005).

[53] G. A. Schuler, Quarkonium Production: Velocity-Scaling Rules and Long-Distance Matrix Elements, *Int. J. Mod. Phys. A* **12**, 3951 (1997).

[54] J. C. Collins, D. E. Soper, Angular Distribution of Dileptons in High-Energy Hadron Collisions, *Phys. Rev. D* **16**, 2219 (1977).

[55] P. Faccioli, C. Lourenço, On the polarization of the non-prompt contribution to inclusive J/ψ production in pp collisions, *JHEP* **10**, 005 (2022).

[56] BaBar Collaboration, Study of inclusive production of charmonium mesons in B decays, *Phys. Rev. D* **67**, 032002 (2003).

[57] M. Beneke, F. Maltoni, I. Z. Rothstein, QCD analysis of inclusive B decay into charmonium, *Phys. Rev. D* **59**, 054003 (1999).

[58] M. Beneke, G. A. Schuler, S. Wolf, Quarkonium momentum distributions in photoproduction and B decay, *Phys. Rev. D* **62**, 034004 (2000).

[59] G. A. Schuler, Quarkonium production and decays, Habilitation thesis, Hamburg U. (1994). Presented on Feb 1994.

[60] E789 Collaboration, Measurement of J/ψ and ψ' production in 800 GeV/c proton-gold collisions, *Phys. Rev. D* **52**, 1307 (1995). [Erratum: Phys. Rev. D 53, 570 (1996)].

[61] P. L. McGaughey, Recent measurements of quarkonia and Drell-Yan production in proton nucleus collisions, *Nucl. Phys. A* **610**, 394 (1996). Quark Matter '96.

[62] M. Butenschoen, B. A. Kniehl, J/ψ Polarization at the Tevatron and the LHC: Nonrelativistic-QCD Factorization at the Crossroads, *Phys. Rev. Lett.* **108**, 172002 (2012).

[63] K.-T. Chao, Y.-Q. Ma, H.-S. Shao, K. Wang, Y.-J. Zhang, J/ψ Polarization at Hadron Colliders in Nonrelativistic QCD, *Phys. Rev. Lett.* **108**, 242004 (2012).

[64] H.-S. Shao, HELAC-Onia 2.0: An upgraded matrix-element and event generator for heavy quarkonium physics, *Comp. Phys. Commun.* **198**, 238 (2016).

[65] B. Gong, L.-P. Wan, J.-X. Wang, H.-F. Zhang, Polarization for Prompt J/ψ and $\psi(2\mathrm{S})$ Production at the Tevatron and LHC, *Phys. Rev. Lett.* **110**, 042002 (2013).

[66] P. Artoisenet, J. Campbell, J. P. Lansberg, F. Maltoni, F. Tramontano, Υ Production at Fermilab Tevatron and LHC Energies, *Phys. Rev. Lett.* **101**, 152001 (2008).

[67] J. Lansberg, Real next-to-next-to-leading-order QCD corrections to J/ψ and Υ hadroproduction in association with a photon, *Phys. Lett. B* **679**, 340 (2009).

[68] J. P. Lansberg, J/ψ production at $\sqrt{s} = 1.96$ and 7 TeV: colour-singlet model, NNLO* and polarization, *J. Phys. G: Nucl. Part. Phys.* **38**, 124110 (2011).

[69] CDF Collaboration, CDF Public Note 9966.

[70] CMS Collaboration, Prompt and non-prompt J/ψ production in pp collisions at $\sqrt{s} = 7$ TeV, *Eur. Phys. J. C* **71**, 1575 (2011).

[71] CMS Collaboration, J/ψ and $\psi(2\mathrm{S})$ production in pp collisions at $\sqrt{s} = 7$ TeV, *JHEP* **02**, 11 (2012).

[72] CMS Collaboration, Measurement of J/ψ and $\psi(2\mathrm{S})$ Prompt Double-Differential Cross Sections in pp Collisions at $\sqrt{s} = 7$ TeV, *Phys. Rev. Lett.* **114**, 191802 (2015).

[73] CMS Collaboration, Measurement of quarkonium production cross sections in pp collisions at $\sqrt{s} = 13$ TeV, *Phys. Lett. B* **780**, 251 (2018).

[74] ATLAS Collaboration, Measurement of the differential cross-sections of inclusive, prompt and non-prompt J/ψ production in proton–proton collisions at $\sqrt{s} = 7$ TeV, *Nucl. Phys. B* **850**, 387 (2011).

[75] ATLAS Collaboration, Measurement of the production cross-section of $\psi(2\mathrm{S}) \rightarrow \mathrm{J}/\psi(\rightarrow \mu^+\mu^-)\pi^+\pi^-$ in pp collisions at $\sqrt{s} = 7$ TeV at ATLAS, *JHEP* **09**, 79 (2014).

[76] ATLAS Collaboration, Measurement of the differential cross-sections of prompt and non-prompt production of J/ψ and $\psi(2\mathrm{S})$ in pp collisions at $\sqrt{s} = 7$ and 8 TeV with the ATLAS detector, *Eur. Phys J. C* **76**, 283 (2016).

[77] LHCb Collaboration, Measurement of J/ψ production in pp collisions at $\sqrt{s} = 7$ TeV, *Eur. Phys. J. C* **71**, 1645 (2011).

[78] LHCb Collaboration, Measurement of $\psi(2\mathrm{S})$ meson production in pp collisions at $\sqrt{s} = 7$ TeV, *Eur. Phys. J. C* **72**, 2100 (2012).

[79] LHCb Collaboration, Measurement of J/ψ production in pp collisions at $\sqrt{s} = 2.76$ TeV, *JHEP* **02**, 41 (2013).

[80] LHCb Collaboration, Production of J/ψ and Υ mesons in pp collisions at $\sqrt{s} = 8$ TeV, *JHEP* **06**, 64 (2013).

[81] LHCb Collaboration, Measurement of forward J/ψ production cross-sections in pp collisions at $\sqrt{s} = 13$ TeV, *JHEP* **10**, 172 (2015). [Erratum: JHEP 05, 063 (2017)].

[82] LHCb Collaboration, Measurement of $\psi(2\mathrm{S})$ production cross-sections in proton-proton collisions at $\sqrt{s} = 7$ and 13 TeV, *Eur. Phys. J. C* **80**, 185 (2020).

[83] ALICE Collaboration, Rapidity and transverse momentum dependence of inclusive J/ψ production in pp collisions at $\sqrt{s} = 7$ TeV, *Phys. Lett. B* **704**, 442 (2011). [Erratum: Phys. Lett. B 718, 692 (2012)].

[84] ALICE Collaboration, Measurement of prompt J/ψ and beauty hadron production cross sections at mid-rapidity in pp collisions at $\sqrt{s} = 7$ TeV, *JHEP* **11**, 65 (2012).

[85] ALICE Collaboration, J/ψ production as a function of charged particle multiplicity in pp collisions at $\sqrt{s} = 7$ TeV, *Phys. Lett. B* **712**, 165 (2012).

[86] ALICE Collaboration, Measurement of quarkonium production at forward rapidity in pp collisions at $\sqrt{s} = 7$ TeV, *Eur. Phys. J. C* **74**, 2974 (2014).

[87] ALICE Collaboration, Inclusive quarkonium production at forward rapidity in pp collisions at $\sqrt{s} = 8$ TeV, *Eur. Phys. J. C* **76**, 184 (2016).

[88] ALICE Collaboration, Energy dependence of forward-rapidity J/ψ and $\psi(2\mathrm{S})$ production in pp collisions at the LHC, *Eur. Phys. J. C* **77**, 392 (2017).

[89] ALICE Collaboration, Prompt and non-prompt J/ψ production cross sections at midrapidity in proton-proton collisions at $\sqrt{s} = 5.02$ and 13 TeV, *JHEP* **03**, 190 (2022).

[90] CMS Collaboration, Measurements of the $\Upsilon(1S)$, $\Upsilon(2S)$, and $\Upsilon(3S)$ differential cross sections in pp collisions at $\sqrt{s} = 7$ TeV, *Phys. Lett. B* **749**, 14 (2015).

[91] ATLAS Collaboration, Measurement of upsilon production in 7 TeV pp collisions at ATLAS, *Phys. Rev. D* **87**, 052004 (2013).

[92] LHCb Collaboration, Measurement of Υ production in pp collisions at $\sqrt{s} = 7$ TeV, *Eur. Phys. J. C* **72**, 2025 (2012).

[93] LHCb Collaboration, Measurement of Υ production in pp collisions at $\sqrt{s} = 2.76$ TeV, *Eur. Phys. J. C* **74**, 2835 (2014).

[94] LHCb Collaboration, Forward production of Υ mesons in pp collisions at $\sqrt{s} = 7$ and 8 TeV, *JHEP* **11**, 103 (2015).

[95] LHCb Collaboration, Measurement of Υ production in pp collisions at $\sqrt{s} = 13$ TeV, *JHEP* **07**, 134 (2018). [Erratum: JHEP 05, 076 (2019)].

[96] LHCb Collaboration, Measurement of $\psi(2\mathrm{S})$ polarisation in pp collisions at $\sqrt{s} = 7$ TeV, *Eur. Phys. J. C* **74**, 2872 (2014).

[97] LHCb Collaboration, Measurement of the $\Upsilon(nS)$ polarizations in pp collisions at $\sqrt{s} = 7$ and 8 TeV, *JHEP* **12**, 110 (2017).

[98] ALICE Collaboration, Measurement of the inclusive J/ψ polarization at forward rapidity in pp collisions at $\sqrt{s} = 8$ TeV, *Eur. Phys. J. C* **78**, 562 (2018).

[99] CDF Collaboration, Cross section for forward J/ψ production in $p\overline{p}$ collisions at $\sqrt{s} = 1.8$ TeV, *Phys. Rev. D* **66**, 092001 (2002).

[100] CDF Collaboration, Measurement of the J/ψ meson and b-hadron production cross sections in $p\overline{p}$ collisions at $\sqrt{s} = 1960$ GeV, *Phys. Rev. D* **71**, 032001 (2005).

[101] CDF Collaboration, Production of $\psi(2\mathrm{S})$ mesons in $p\overline{p}$ collisions at 1.96 TeV, *Phys. Rev. D* **80**, 031103 (2009).

[102] CDF Collaboration, Production of $\Upsilon(1S)$ Mesons from χ_b Decays in $p\overline{p}$ Collisions at $\sqrt{s} = 1.8$ TeV, *Phys. Rev. Lett.* **84**, 2094 (2000).

[103] CDF Collaboration, Υ Production and Polarization in $p\overline{p}$ Collisions at $\sqrt{s} = 1.8$ TeV, *Phys. Rev. Lett.* **88**, 161802 (2002).

[104] D0 Collaboration, Small Angle J/ψ Production in $p\overline{p}$ Collisions at $\sqrt{s} = 1.8$ TeV, *Phys. Rev. Lett.* **82**, 35 (1999).

[105] D0 Collaboration, Measurement of Inclusive Differential Cross Sections for $\Upsilon(1S)$ Production in $p\overline{p}$ Collisions at $\sqrt{s} = 1.96$ TeV, *Phys. Rev. Lett.* **94**, 232001 (2005). [Erratum: PRL 100, 049902 (2008)].

[106] CMS Collaboration, Measurement of the relative prompt production rate of χ_{c2} and χ_{c1} in pp collisions at $\sqrt{s} = 7$ TeV, *Eur. Phys. J. C* **72**, 2251 (2012).

[107] LHCb Collaboration, Measurement of the cross-section ratio $\sigma(\chi_{c1})/\sigma(\chi_{c2})$ for prompt χ_c production at $\sqrt{s} = 7$ TeV, *Phys. Lett. B* **714**, 215 (2012).

[108] LHCb Collaboration, Measurement of the relative rate of prompt χ_{c0}, χ_{c1} and χ_{c2} production at $\sqrt{s} = 7$ TeV, *JHEP* **10**, 115 (2013).

[109] CMS Collaboration, Measurement of the production cross section ratio $\sigma(\chi_{b2}(1P))/\sigma(\chi_{b1}(1P))$ in pp collisions at $\sqrt{s} = 8$ TeV, *Phys. Lett. B* **743**, 383 (2015).

[110] ATLAS Collaboration, Measurement of χ_{c1} and χ_{c2} production with $\sqrt{s} = 7$ TeV pp collisions at ATLAS, *JHEP* **07**, 154 (2014).

[111] CMS Collaboration, Constraints on the χ_{c1} versus χ_{c2} Polarizations in Proton-Proton Collisions at $\sqrt{s} = 8$ TeV, *Phys. Rev. Lett.* **124**, 162002 (2020).

[112] M. BUTENSCHOEN, B. A. KNIEHL, Next-to-leading order tests of non-relativistic-QCD factorization with J/ψ yield and polarization, *Mo. Phys. Lett. A* **28**, 1350027 (2013).

[113] I. Kratschmer, Measurements of prompt J/ψ and ψ(2S) production and polarization at CMS, Ph.D. thesis, Vienna, Tech. U., Atominst. (2015).

[114] S. Fleming, O. F. Hernández, I. Maksymyk, H. Nadeau, NRQCD matrix elements in polarization of J/ψ produced from b decay, *Phys. Rev. D* **55**, 4098 (1997).

[115] V. Krey, K. R. S. Balaji, Polarized J/ψ production from B mesons at the Fermilab Tevatron, *Phys. Rev. D* **67**, 054011 (2003).

[116] M. Butenschoen, B. A. Kniehl, J/ψ production in NRQCD: A global analysis of yield and polarization, *Nucl. Phys. B, Proc. Suppl.* **222-224**, 151 (2012). Proceedings of the Ringberg Workshop New Trends in HERA Physics 2011.

[117] P. Faccioli, C. Lourenço, T. Madlener, From prompt to direct J/ψ production: new insights on the χ_{c1} and χ_{c2} polarizations and feed-down contributions from a global-fit analysis of mid-rapidity LHC data, *Eur. Phys. J. C* **80**, 623 (2020).

[118] P. Faccioli, C. Lourenço, NRQCD colour-octet expansion vs. LHC quarkonium production: signs of a hierarchy puzzle?, *Eur. Phys. J. C* **79**, 457 (2019).

[119] L. Evans, P. Bryant, LHC Machine, *JINST* **3**, S08001 (2008).

[120] CMS Collaboration, *CMS Physics: Technical Design Report Volume I: Detector Performance and Software*, Technical design report. CMS (CERN, Geneva, 2006).

[121] CMS Collaboration, CMS Physics Technical Design Report, Volume II: Physics Performance, *J. Phys. G: Nucl. Part. Phys.* **34**, 995 (2007).

[122] CMS Collaboration, The CMS experiment at the CERN LHC, *JINST* **3**, S08004 (2008).

[123] Esma Mobs, The CERN accelerator complex - August 2018. Complexe des accélérateurs du CERN - Août 2018, http://cds.cern.ch/record/2636343 (2018).

[124] ALICE Collaboration, The ALICE experiment at the CERN LHC, *JINST* **3**, S08002 (2008).

[125] ATLAS Collaboration, The ATLAS Experiment at the CERN Large Hadron Collider, *JINST* **3**, S08003 (2008).

[126] LHCb Collaboration, The LHCb Detector at the LHC, *JINST* **3**, S08005 (2008).

[127] CMS Collaboration, CMS Public Luminosity Results, https://twiki.cern.ch/twiki/-bin/view/CMSPublic/LumiPublicResults (2024).

[128] T. Sakuma, Cutaway diagrams of CMS detector, http://cds.cern.ch/record/2665537 (2019).

[129] T. Sakuma, T. McCauley, Detector and Event Visualization with SketchUp at the CMS Experiment, *J. Phys.: Conf. Ser.* **513**, 022032 (2014).

[130] CMS Collaboration, Interactive Slice of the CMS detector, https://cms-docdb.cern.ch/cgi-bin/PublicDocDB//ShowDocument?docid=4172 (2011).

[131] The Tracker Group of the CMS collaboration, The CMS Phase-1 pixel detector upgrade, *JINST* **16**, P02027 (2021).

[132] CMS Collaboration, CMS trigger performance, *Eur. Phys. J. Conf.* **182**, 02037 (2018).

[133] CMS Collaboration, The CMS trigger system, *JINST* **12**, P01020 (2017).

[134] CMS Collaboration, CMS Technical Design Report for the Level-1 Trigger Upgrade, *Tech. rep.* (2013).

[135] CMS Collaboration, *CMS The TriDAS Project: Technical Design Report, Volume 2: Data Acquisition and High-Level Trigger. CMS trigger and data-acquisition project*, Technical design report. CMS (CERN, Geneva, 2002).

[136] C. Collaboration, CMS Run 2 High Level Trigger Performance, *Tech. rep.*, CERN, Geneva (2020).

[137] CMS Collaboration, Enriching the physics program of the CMS experiment via data scouting and data parking (2024).

[138] T. Madlener, Measurement of the prompt χ_{c1} and χ_{c2} polarizations at CMS, Ph.D. thesis, Technische Universität Wien (2020).

[139] CMS Collaboration, Heavy Flavour distributions from CMS with 2017 data at $\sqrt{s} = 13$ TeV, http://http://cds.cern.ch/record/2276459 (2017).

[140] CMS Collaboration, Description and performance of track and primary-vertex reconstruction with the CMS tracker, *JINST* **9**, P10009 (2014).

[141] R. Frühwirth, Application of Kalman filtering to track and vertex fitting, *Nucl. Instrum. Meth. A* **262**, 444 (1987).

[142] P. Faccioli, C. Lourenço, J. Seixas, H. K. Wöhri, Study of ψ' and χ_c decays as feed-down sources of J/ψ hadro-production, *JHEP* **10**, 004 (2008).

[143] F. Cavallari, C. Rovelli, Calibration and Performance of the CMS Electromagnetic Calorimeter in LHC Run2, *EPJ Web Conf.* **245**, 02027 (2020).

[144] T. Sjöstrand, S. Mrenna, P. Skands, A brief introduction to PYTHIA 8.1, *Comp. Phys. Commun.* **178**, 852 (2008).

[145] N. Davidson, T. Przedzinski, Z. Wąs, PHOTOS interface in C++: technical and physics documentation, *Comput. Phys. Commun.* **199**, 86 (2016).

[146] GEANT4 Collaboration, GEANT4—a simulation toolkit, *Nucl. Instrum. Meth. A* **506**, 250 (2003).

[147] M. J. Oreglia, A study of the reactions $\psi' \to \gamma\gamma\psi$, Ph.D. thesis, Stanford University (1980).